# Electrical Properties and Defect Structure of Praseodymium-Cerium Oxide Solid Solutions

by

Todd Stanley Stefanik

BS Ceramic Engineering

New York State College of Ceramics at Alfred University, 1995

SM Materials Science and Engineering

Massachusetts Institute of Technology, 1998

SUBMITTED TO THE DEPARTMENT OF
MATERIALS SCIENCE AND ENGINEERING
IN PARTIAL FULFILLMENT OF THE REQUIREMENTS
FOR THE DEGREE OF
DOCTOR OF PHILOSOPHY IN CERAMICS

FEBRUARY 2004

© 2003 Massachusetts Institute of Technology. All rights reserved.

Signature of Author_____
Todd Stanley Stefanik
January 23rd, 2004

Certified by_____
Harry L. Tuller
Professor of Ceramics and Electronic Materials
Thesis Supervisor

Accepted by_____
Harry L. Tuller
Professor of Ceramics and Electronic Materials
Chairperson, Departmental Committee on Graduate Students

Electrical Properties and Defect Structure of
Praseodymium-Cerium Oxide Solid Solutions

by

Todd Stanley Stefanik

Submitted to the Department of Materials Science and Engineering in Partial Fulfillment of the Requirements for the Degree of Doctor of Philosophy in Ceramics

## Abstract

A defect chemistry model consistent with observed trends in the $pO_2$ and temperature dependence of electrical conductivity in praseodymium cerium oxide (PCO) was developed. Four point DC conductivity measurements were made from 1 atm to $10^{-18}$ atm $pO_2$ over isotherms ranging from 600-1000°C in materials containing 0-20% Pr. A $pO_2$-dependent ionic conductivity was observed at high $pO_2$ values in compositions containing 0.5% and 1% Pr. This behavior was attributed to oxidation of $Pr^{3+}$ to $Pr^{4+}$ under oxidizing conditions, thereby decreasing the concentration of acceptor dopants in the PCO material. In compositions containing 10% and 20% Pr, an electron hopping conductivity was observed at high $pO_2$ values. This contribution was strongest at low temperatures and was attributed to the formation of a praseodymium impurity band within the $CeO_2$ band gap. Defect association significantly altered the predicted $pO_2$ dependence of the impurity band conductivity, especially at low temperatures.

The temperature dependences of the thermodynamic parameters governing defect formation and transport in PCO were determined. The reduction enthalpy of cerium was significantly decreased with additions of Pr from approximately 4.7 eV (the value in pure $CeO_2$) to 3.4 eV in 20% PCO. The energy between the Pr impurity band and the $CeO_2$ conduction band was approximately 0.95 eV for 10% and 20% PCO samples. The measured trap depth was significantly higher (approximately 1.6 eV) in 0.5% and 1% PCO. The migration enthalpy for impurity band hopping conductivity was approximately 0.55 eV, slightly higher than the hopping enthalpy for intrinsic carriers in $CeO_2$ (0.4 eV). The oxygen ion migration enthalpy measured for most samples was approximately 0.6-0.7 eV, in agreement with values determined for other rare-earth doped systems. At 20% Pr, the total migration energy increased to approximately 0.9 eV. This increase was attributed to an association energy at high doping levels.

Coulometric titration measurements were also performed in order to confirm the total nonstoichiometry in PCO. The ionization energy for $Pr^{3+} \rightarrow Pr^{4+}$ ($E_{Pr}$) in 20% PCO as calculated from coulometric titration measurements was approximately 1.1 eV, in relatively good agreement with the value determined from electrical conductivity data (approximately 0.95eV). Values of the praseodymium ionization constant ($K_{Pr}$) derived from coulometric titration data were lower than those derived from electrical conductivity measurements. This corresponds to a higher total nonstoichiometry measured via

coulometric titration and points to the possible existence of uncharged oxygen vacancies, particularly at low temperatures.

During the course of these experiments, it became evident that the mechanical stability of PCO needs to be addressed if the material is to be used in real applications. Oxygen uptake/evolution during reduction/oxidation cycles appears to result in development of significant stresses and cracking. While the material may be useful in powder form, this cracking issue must be addressed if it is to be used in bulk or thin film form.

Thesis Supervisor: Harry Tuller

Title: Professor of Ceramics and Electronic Materials

## Acknowledgements

There are a host of individuals who have made this thesis possible. Without their contributions, this degree would not have happened.

First I'd like to thank my advisor, professor Harry Tuller. He's been an excellent supervisor of this work on all fronts. His technical knowledge, experience, interest in the subject, flexibility, and genuine care for me, both as a student and a professional researcher have all been obvious, unfailing, and appreciated.

My thesis committee, consisting of professor Caroline Ross and professor Bernhardt Wuensch has been instructive, constructively critical, and accommodating, even when my timing has been difficult. They've demonstrated a genuine interest in improving my work and I thank them for their efforts.

I have had the privilege of working with a great research group over the last four years. Be it assistance with an experimental setup, help placing an order, discussions about the work, lunch breaks, hiking trips, skiing adventures, or a ride home at 11pm, the group has always been fun, helpful, and supportive.

There have been lots of folks outside the office who have been instrumental in this research as well. The Lutheran-Episcopal Ministry has been a great source of support, camaraderie, calming, challenge, and friendship. My involvement with ice hockey and softball have provided me with the physical exercise and stress relief I require. Both have kept me in contact with the world outside of science, not as trivial as it sounds when working on a PhD.

Thank you to Kathye, Jack, Bette, and Ron for giving me a home away from home to visit while I've been in Boston. It's been great to have a place to go when the drive to New York wasn't feasible.

Emily's love and support has made the doctoral process infinitely more enjoyable. Whether calming me when things just weren't working right, encouraging me when motivation was low, distracting me when the work seemed overwhelming, correcting me when my grammar wasn't quite right, or simply making me realize that there are things in life much more important than work, her contributions to my work and my life have been immeasurable.

My parents, Stan and Elaine, always provided me with inspiration, support, and love. They've been there through it all, both leading up to and throughout my time at MIT. They've heard all the complaints, shared in the small victories, and helped me make the choices I've made to get to where I am today. They've been excellent role models and I'm proud to be their son. My brothers and sisters-in-law have been pulling for me for a long while, offering me respite from the rigors of Boston whenever I can escape. I'm glad to be able to say I'm done!

And finally, I'd like to thank the organizations responsible for funding my studies. This work was supported by the DoD Multidisciplinary University Research Initiative (MURI) program administered by the Army Research Office under Grant DAAD19-01-1-0566 and the National Science foundation under grant number DMR-9701699.

Thanks be to God!

## Table of Contents

# List of Figures

# List of Tables

# Chapter 1. Introduction

## *1.1. Motivation*

Cerium oxide has long been studied as an oxygen ion conducting solid electrolyte material. Typically acceptors (such as $Gd^{3+}$, $Y^{3+}$, $Sm^{3+}$, $Ca^{2+}$, etc) are added in order to increase the concentration of oxygen vacancies in the system and suppress electronic conductivity under reducing conditions. The solid solubility for such acceptors is quite high in the fluorite-like $CeO_2$ structure, giving the opportunity for heavily doped systems (>40%)[1,2]. The ionic conductivity of such $CeO_2$-based electrolytes is higher than that of the most common solid electrolyte, yttria-stabilized zirconia,[3] making it appealing as an electrolyte for solid oxide fuel cells. As a result, extensive research has been performed on such solid solution systems.[1-35]

Most research on the electrical behavior of the $CeO_2$ system has been directed at solid electrolytes. Doping with a multi-valent cation such as praseodymium can yield a mixed electronic-ionic conductor (MEIC). By varying the Pr to Ce ratio, it is possible to control the degree of electronic vs. ionic conductivity over a wide range of $pO_2$ values and temperatures.[36] In general, higher concentrations of multivalent Pr yield higher electronic conductivity at high $pO_2$ values (where a mix of $Pr^{3+}$ and $Pr^{4+}$ exists) and higher ionic conductivity under more reducing conditions, where nearly all Pr acts as an acceptor in the $Pr^{3+}$ state. Such mixed conductors have applications as fuel cell electrodes,[37-40] and oxygen separation membranes.[27,41,42] In addition, the wide range of solid solubility between $CeO_2$ and $Pr_6O_{11}$,[27,43,44] the large nonstoichiometry possible in the system,[36,45] and the dependence of electrical properties on thermal and $pO_2$ history result in a high degree of flexibility in tuning the low-temperature electrical properties of the material. Such flexibility could be helpful in low temperature devices such as surface-effect gas sensors.[46] Furthermore, few systems exist in which a large concentration of a multi-valent cation can be incorporated into a stable, well-studied host material without significantly altering the host material itself. As praseodymium-doped cerium oxide (PCO) is stable over a wide range of solid solution, it is an ideal material for basic investigation of the electrical properties in such systems.

While the potential applications and benefits of PCO are numerous, relatively few systematic studies of the pure binary system have been performed. Takasu first examined the electrical conductivity of the solid solution between 0 and 70% Pr as a function of temperature in air using solid solutions prepared by the mixed oxide route.[44] Shuk and coworkers examined a range of compositions containing less than 30% Pr prepared by hydrothermal synthesis, again as a function of temperature.[27] Several authors have examined the effects of small additions of Pr (less than 5%) to typical solid electrolyte materials (such as 10% Gd doped $CeO_2$).[16,22-24] Most studies have examined the suitability of a limited range of compositions for a specific application, yet few have investigated the conduction mechanisms in PCO. The goal of this work is to collect electrical conductivity data as a function of both temperature and $pO_2$ and develop a defect model which describes electrical conductivity in PCO solid solutions.

## *1.2. Cerium Oxide*

Cerium oxide has long been studied across a number of fields, most notably catalysis and solid state ionic conductors. A great deal is known about the system and it has been carefully characterized, making it a good starting point and reference in examination of new materials. The theory of electrical conductivity, nonstoichiometry, phase stability, and doping in the material is well understood. Large numbers of dopants have been added to the system and the defect chemistry of the material is generally well understood. The following is a brief review of research in the $CeO_2$ system.

### 1.2.1. The Fluorite Structure

Cerium oxide crystallizes in the cubic fluorite structure. Many solid state ion conductors share this structure, including $CeO_2$, $PrO_2$, $TbO_2$, $ThO_2$, and $UO_2$. In addition, cubic zirconia can be stabilized as the cubic fluorite phase with substantial additions of acceptor dopants. Yttrium is one of the most common, and yttria stabilized zirconia (YSZ) is one of the most commonly used solid oxide ion electrolytes in use.

The fluorite structure consists of a face centered cubic array of cations with all tetrahedral interstices filled with oxygen ions. There are four cations and eight oxygen ions per unit cell. Cations are tetrahedrally coordinated about the anions, and the oxygen ions are

8-fold coordinated about the cations. See Figure 1.1 for a diagram of the fluorite structure.

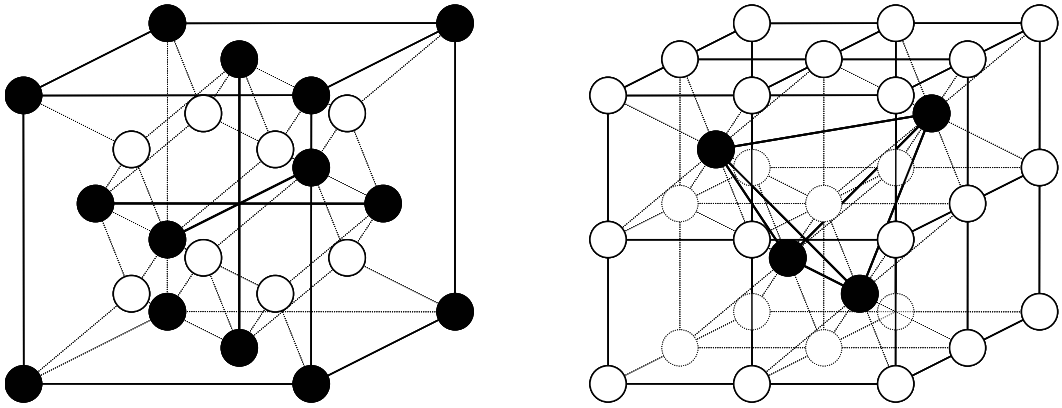

**Figure 1.1. The fluorite structure. Solid circles represent cations, open circles represent oxygen ions. The two unit cells are identical, the only difference being the choice of origin in the unit cell.**

### 1.2.2. Phase Stability

The basic fluorite array is very stable with respect to the removal of oxygen ions from the structure. It is easy to replace 20% of the cations in the system with triply-charged acceptors which are electrically compensated by the formation of doubly-charged oxygen vacancies, resulting in 5% of the total number of oxygen ions being removed from the structure. In the case of YSZ, this high oxygen vacancy concentration actually stabilizes the fluorite phase over the tetragonal or monoclinic structure. The solubility of rare earth oxides has been reported to be higher than 40% in some systems,[1,2] resulting in a 10% deficiency in oxygen content while still maintaining the cubic fluorite phase.

In pure $CeO_2$, the cerium ion can be reduced towards the $Ce^{3+}$ state by reduction of the oxygen partial pressure. The pure compound is not as stable with respect to oxygen nonstoichiometry as doped systems, however. Under reducing conditions, a large series of intermediate ordered phases may form (especially at low temperatures). Figure 1.2 shows phase diagrams for both the cerium-oxygen and praseodymium-oxygen systems.[47-53]

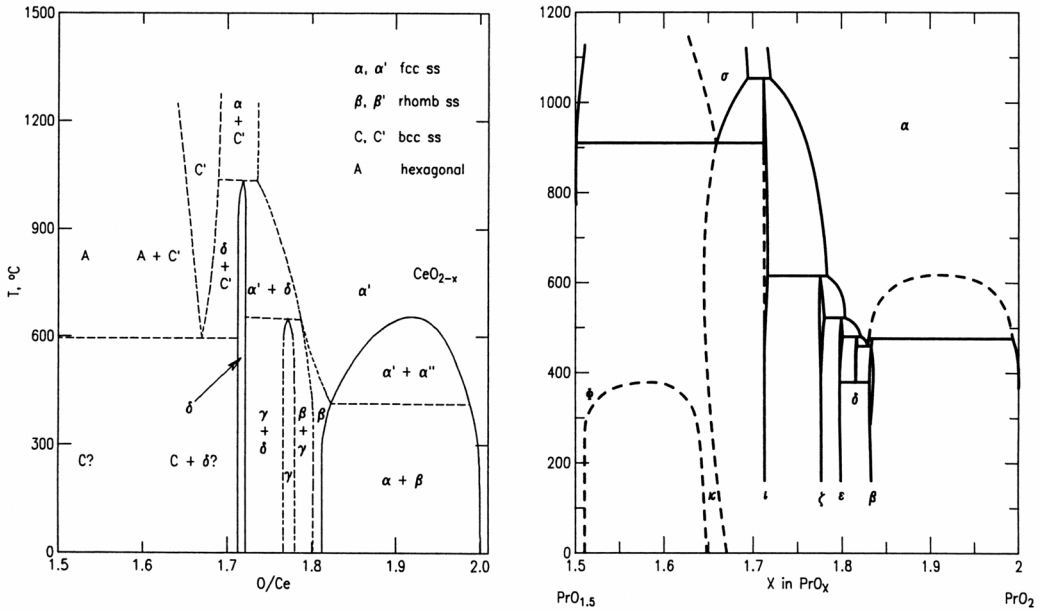


**Figure 1.2. Phase diagrams in the Ce-O and Pr-O systems. Ce-O diagram is #91-323 in Phase Diagrams for Ceramists[47] according to Lorenzelli[48], derived from data of Bevan[51,52] and Campserveux[50]. Pr-O diagram is #6263 in Phase Diagrams for Ceramists[53] according to Eyring[49].**

### 1.2.3. Conductivity in $CeO_2$

Pure $CeO_2$ is an n-type semiconductor at elevated temperatures. Reduction of the cerium ions enables electrons to move from one cation to the next (electrons can hop from a $Ce^{3+}$ to an adjacent $Ce^{4+}$ ion). When the reduction of Ce is electrically compensated by the formation of doubly-charged oxygen vacancies ($V_O^{\bullet\bullet}$), the electronic conductivity follows a $pO_2^{-1/6}$ dependence. If singly-charged acceptors are present in the system, the electronic conductivity follows a $pO_2^{-1/4}$ dependence. The defect chemistry of pure ceria will be discussed in more detail in the defect chemistry section.

Transport of electrons in $CeO_2$ occurs via hopping of polarons through the cerium sub-lattice. A polaron is the combination of an electron and the associated lattice distortion that its presence creates in the structure through which it moves. In order for conduction to occur, both the electron and the distortion must move together. The result, when the electron becomes self-trapped in the resultant potential well, is an activated hopping process (such that $\sigma = (\sigma^o/T)\exp(-E_H/kT)$) where $\sigma$ is conductivity, k is the Boltzman constant, T is the absolute temperature, and $E_H$ is the enthalpy of migration. The details of polaron hopping will be discussed further in the defect chemistry section.

Ionic conductivity also occurs in pure ceria. However, the contribution of oxide ions to the total conductivity is small relative to the electronic conductivity. Oxygen vacancies undergo a hopping process as well, resulting in a thermally activated ionic conductivity. While mixed conduction does occur in pure ceria, the ionic contribution is small, particularly at elevated temperatures and under reducing conditions. For instance, the ionic contribution to the total conductivity in pure ceria at 1000°C and $10^{-6}$ atm $pO_2$ is less than 3%.[54] This figure decreases further as $pO_2$ is reduced. Doping with acceptor cations increases the oxygen vacancy concentration and ionic conductivity in $CeO_2$ dramatically. Conduction in doped $CeO_2$ will be discussed below.

Figure 1.3 shows the electrical conductivity of $CeO_2$ over a range of $pO_2$ values for several temperatures.[55,56] The conductivity shown is largely electronic with an ionic contribution only evident at the lowest isotherm under oxidizing conditions. The regions labeled I through IV correspond to different defect regimes. Region I corresponds to conductivity determined by extrinsic doping due to impurities in the samples measured. Region II is the region where doubly-charged oxygen vacancies compensate the reduction of $Ce^{4+}$ to $Ce^{3+}$, resulting in a $pO_2^{-1/6}$ conductivity dependence. In region III, reduction is compensated by singly-charged vacancies, yielding a $pO_2^{-1/4}$ dependence. In region IV, significant deviations from stoichiometry result in anomalous conductivity trends. Again, the relevant defect chemical equilibria will be discussed further in the defect chemistry section. This plot was included here in order to introduce the general trends and magnitude of conductivity in pure $CeO_2$.

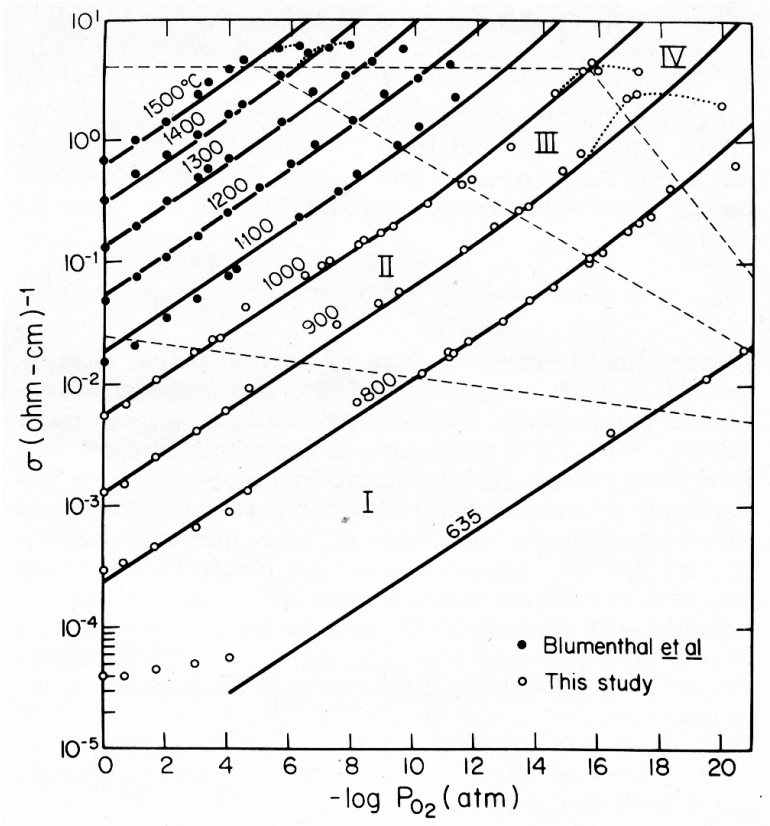


**Figure 1.3. Conductivity (σ) in pure $CeO_2$ as a function of $pO_2$. The regions noted in the graph represent different defect regimes. See text for details.[55,56]**

### 1.2.4. Doped $CeO_2$ Systems

When $CeO_2$ is doped with divalent or trivalent cations, the incorporation of these acceptors into the structure is compensated by the formation of anion vacancies. This elevated vacancy concentration increases the ionic conductivity by orders of magnitude. The resulting doped $CeO_2$ systems are excellent solid electrolytes. Figure 1.4 compares the ionic conductivities of several electrolyte systems as a function of temperature.[57] Most notable is that 20% Gd-doped $CeO_2$ exhibits higher ionic conductivity than that of the zirconias, the most widely used electrolytes. This makes doped ceria particularly attractive as a low temperature solid electrolyte.

While very high amounts of rare earth elements can be incorporated into $CeO_2$, there is a maximum in ionic conductivity as a function of dopant concentration. Above this maximum, defect association reduces the mobility of the oxygen vacancies and the total conductivity drops again. Figure 1.5 shows the variation in conductivity as a function of

samarium concentration in $CeO_2$ at several temperatures.[34] Similar behavior is observed for all acceptor dopants in $CeO_2$, though the composition of maximum conductivity varies with individual dopants.

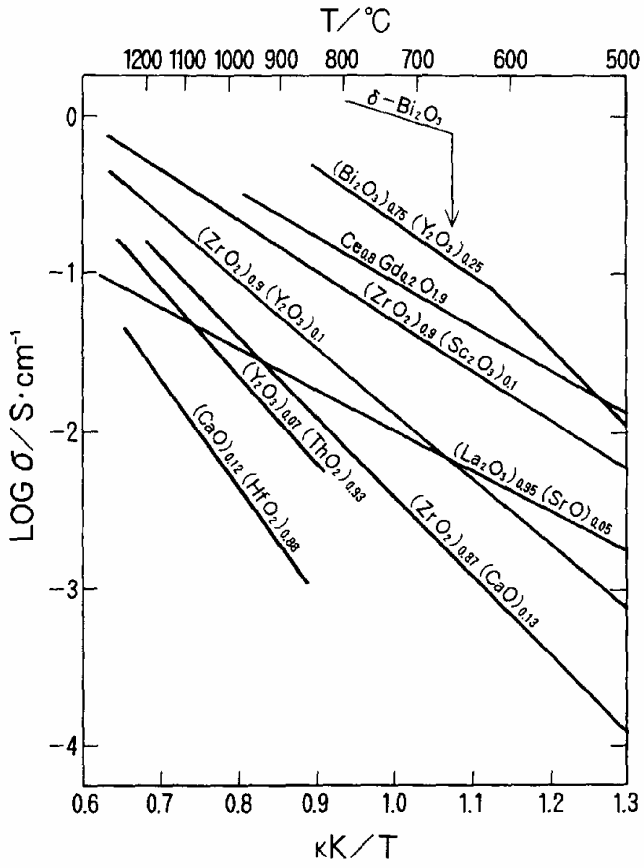


**Figure 1.4. Ionic conductivities (σ) of several fluorite-based oxide ion conductors.[57]**

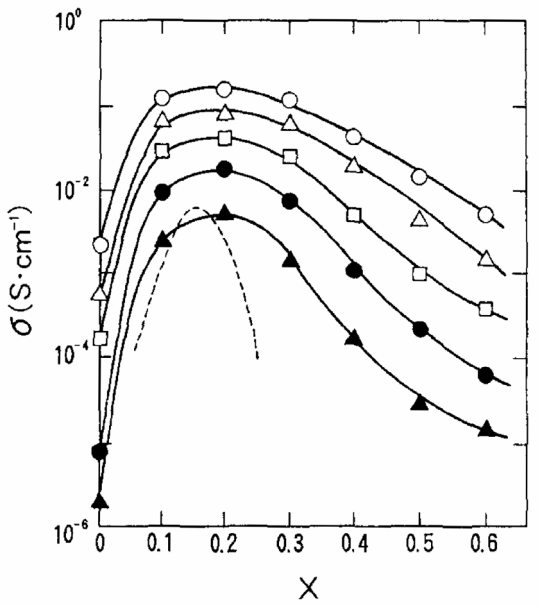


**Figure 1.5. The variation of ionic conductivity (σ) with samarium content (x) in samaria doped ceria. The individual graphs represent conductivity at 500-900°C in 100°C increments, starting with the lowest conductivity at 500°C. The dotted line represents calcia doped zirconia at 800°C[34]**

One of the major problems with using $CeO_2$-based solid electrolyte systems is related to the reduction of the Ce host material under reducing conditions. While doping with acceptors does increase the ionic conductivity well beyond the magnitude of the intrinsic electrical conductivity of $CeO_2$ at high $pO_2$ values, at lower $pO_2$ values and high temperatures, reduction gives rise to a significant electronic conductivity. Figure 1.6 and Figure 1.7 show the electrical conductivity of 10% yttria doped ceria as a function of $pO_2$ and the ionic transference number ($\sigma_{ion}/\sigma_{total}$) for several temperatures.[29] Figure 1.7 demonstrates a primary concern for researchers in the field of $CeO_2$-based solid electrolytes. Reduction of Ce at low $pO_2$ limits the utility of $CeO_2$ based electrolyte systems. Numerous studies focus on methods by which the electronic conductivity in the systems at low $pO_2$ can be suppressed.

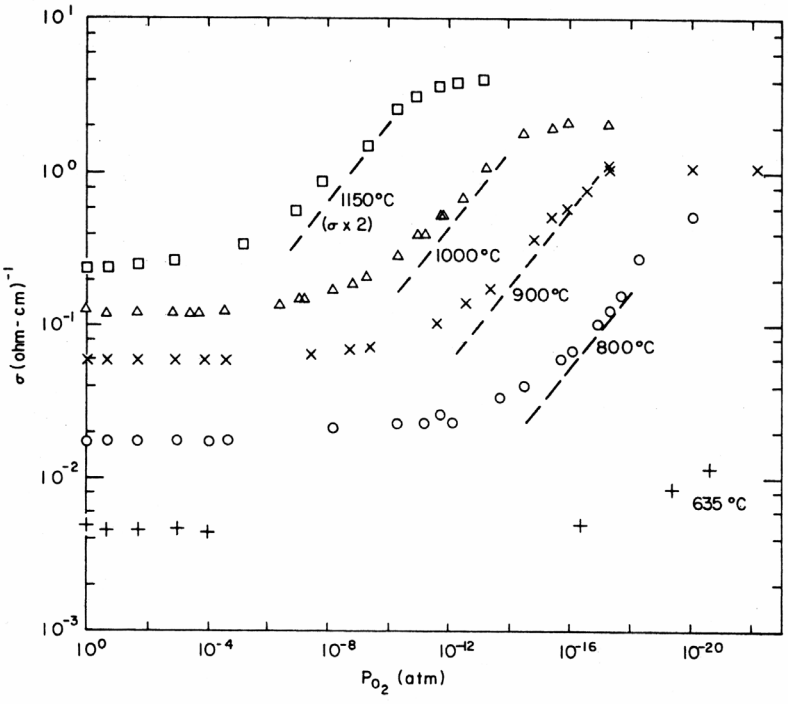


**Figure 1.6. Total conductivity in 10% yttria doped ceria. Dashed lines represent the electronic component of the conductivity.[29]**

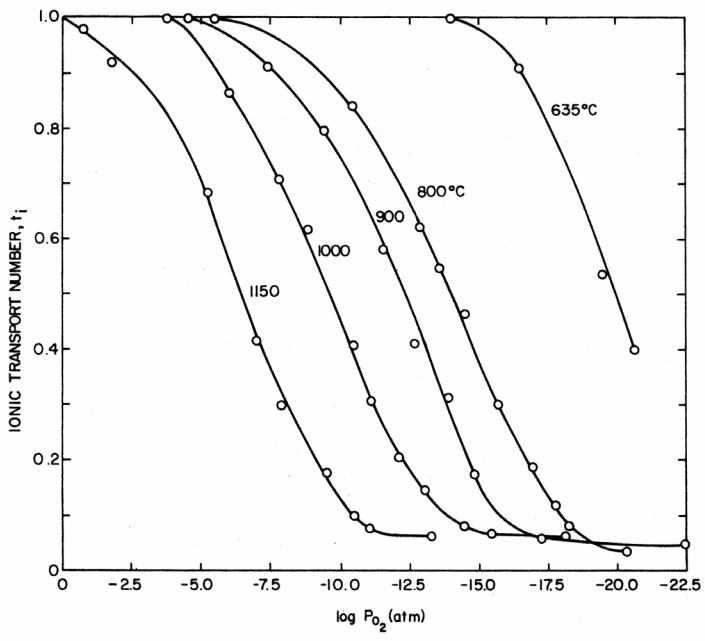


**Figure 1.7. Ionic transference numbers as a function of $pO_2$ and temperature corresponding to the conductivity data presented in Figure 1.6.[29]**

## *1.3. Praseodymium-Cerium Oxide (PCO)*

### 1.3.1. Motivation

While a large focus of research in the field of $CeO_2$ based systems involves enhancing ionic conductivity and suppressing electronic conductivity, not all applications require perfect solid electrolytes. To the contrary, some applications require mixed electronic-ionic conductors (MEIC's). Solid oxide fuel cell electrodes, for instance, often rely on so called "triple point boundaries" to bring oxygen ions from the electrolyte, electrons from the external circuit, and oxygen gas from the atmosphere together in order for the electrode reaction to occur. An MIEC electrode would allow the reaction to occur across all surfaces of the material, rather than just at the triple point boundaries, potentially increasing the efficiency of the electrode. Oxygen separation membranes are used to produce high purity oxygen simply by allowing oxygen to diffuse through a solid electrolyte under an applied oxygen activity gradient. In order for this process to occur, however, a compensating flow of electronic charge must counteract the flow of oxygen vacancies through the material. An MIEC allows this to happen through a counter-flow of electrons.

Addition of Pr to $CeO_2$ enhances reduction in the solid solution. Pr, like Ce, can switch valence between $Pr^{4+}$ and $Pr^{3+}$, but is generally much more reducible than Ce. In fact, praseodymia is significantly reduced in its equilibrium form in air as $Pr_6O_{11}$. Adding Pr to Ce results in reduction at much higher $pO_2$ values than those required to reduce pure $CeO_2$. The increased oxygen availability can be utilized in such applications as three way catalysts for reacting exhaust gasses (where the catalyst serves as a supply/sink for oxygen in the oxidation/reduction reactions being performed)[58] or in sorption compressors, where a change in temperature is used to pressurize a gas.[59]

There are a host of applications which could benefit form a fundamental understanding of defect chemistry and transport in PCO. To date, however, no such studies have been performed. The few studies that have been done have typically focused on a relatively quick analysis of suitability for a given application. The goal of this study is to develop a defect model and provide an understanding of electrical transport in PCO.

### 1.3.2. Previous Studies of PCO

Takasu and coworkers carried out some of the first investigations of electrical conductivity in PCO in the mid 1980's.[44] They realized that the catalytic activity and mixed conductivity possible in PCO could be useful in solid oxide fuel cell electrode materials. Compositions ranging from 0-100% Pr were fabricated using a mixed oxide technique. Phase stability was maintained through 70% Pr, as determined by X-ray diffraction analysis. Figure 1.8 shows the lattice parameter in PCO as a function of composition as found by Takasu and coworkers. The lattice constant decreases linearly with added Pr content and phase separates into two separate fluorite phases at compositions of 80% Pr and higher. The total electrical conductivity of the samples was measured at 10kHz as a function of temperature (Figure 1.9). The total conductivity in the system was found to increase with increasing Pr content. The data does not obey Arrhenius behavior. No explanation or discussion of the results was presented.

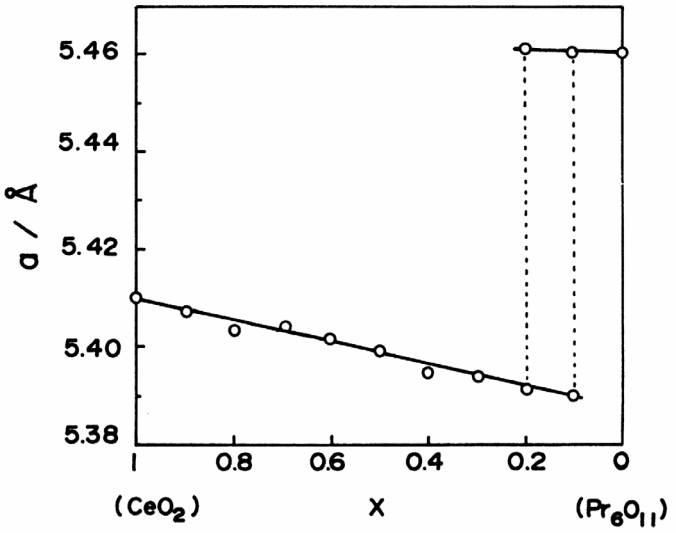


**Figure 1.8. Lattice constant as a function of Pr content in PCO as determined by Takasu and coworkers.[44]**

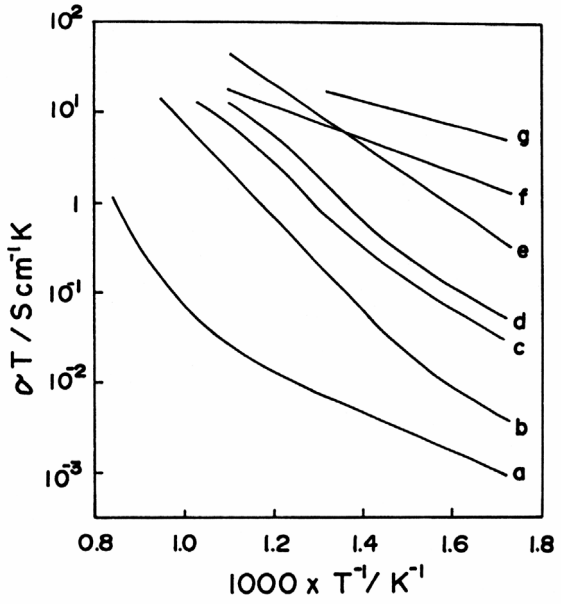


**Figure 1.9. Total conductivity (σ) in PCO as determined by Takasu and coworkers. Compositions range from 10% Pr (a) to 70% Pr (g) in steps of 10%.[44]**

In addition, the ionic transference number ($\sigma_{ion}/\sigma_{total}$) was determined using a concentration cell. A disk of the material to be tested was exposed to air on one side (0.21 atm $pO_2$) and pure oxygen on the other side (1 atm $pO_2$). If the material were a perfect oxygen ion conductor, a Nernst voltage would develop across the disk of material equal to (RT/4F)ln(0.21 atm/1 atm), where R is the gas constant, F the Faraday constant, and T is absolute temperature. If the material is a mixed conductor, the observed voltage is decreased by an amount proportional to the ionic transference number ($V_{observed} = t_i \bullet V_{theoretical}$). The ionic transference numbers are shown as a function of temperature in Figure 1.10. Increasing the concentration of Pr in the system increases the electronic conductivity and decreases the ionic transference number.

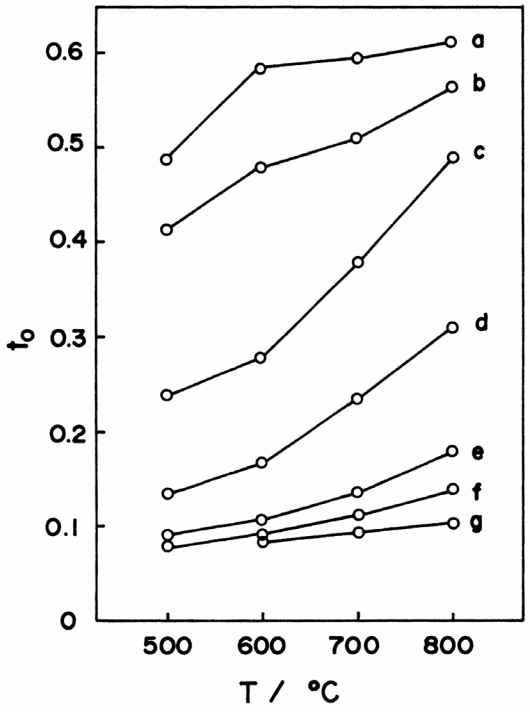


**Figure 1.10. Ionic transference numbers in PCO measured by Takasu and coworkers.[44]**

Nauer and coworkers[43] performed similar experiments to those conducted by Takasu. Their results, however, were significantly different. Figure 1.11 shows the lattice parameter of the materials produced in Nauer's study. The lattice parameters are in reasonable agreement with Takasu's results, but the region of phase stability is significantly different. Nauer observed second phases at compositions as low as 40% Pr. Nauer also observed significantly higher conductivities than those reported by Takasu, though measurements of two different samples in Nauer's study yielded different results (changes in conductivity by factors of 2-3X were observed depending on the sample measured). No explanation for these discrepancies was offered.

Shuk and coworkers[27] fabricated compositions of PCO using a hydrothermal process. They found a different composition dependence of lattice parameter than did Takasu and Nauer (Figure 1.12). The solubility limit of approximately 30% Pr was in agreement with the limit found by Nauer, but the lattice parameter in single phase compositions increased with increasing Pr content. The method of processing and lower processing temperatures was assumed to result in a higher concentration of $Pr^{3+}$ ions than that

produced by higher temperature techniques, yielding the reverse trend in lattice parameter variation. The total conductivities reported in the work of Shuk appear to be comparable to those determined by Nauer. Concentration cell measurements seem to be in reasonable agreement with those presented by Takasu (Figure 1.13), at least for heavily doped samples. The ionic transference number for 10% PCO reported by Shuk was considerably higher than that reported by Takasu.

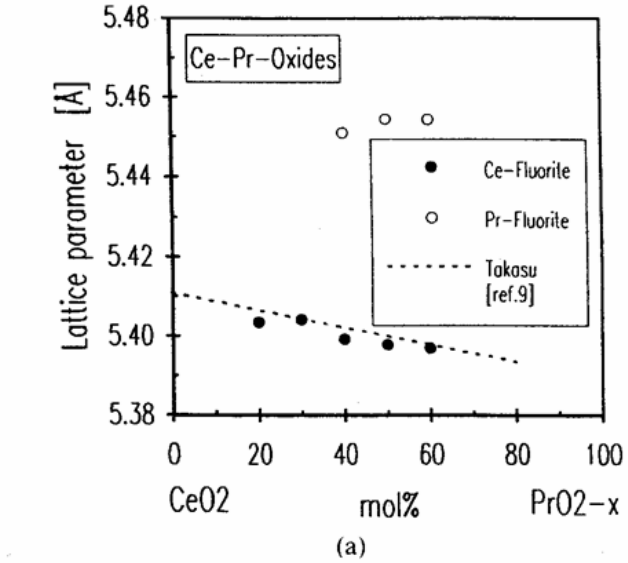


**Figure 1.11. Lattice parameters in PCO as determined by Nauer and coworkers.[43]**

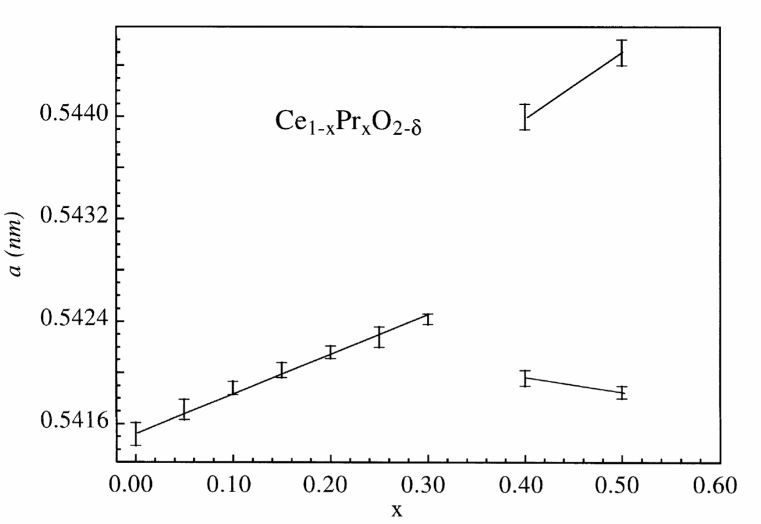


**Figure 1.12. Lattice parameters in PCO as determined by Shuk and coworkers.[27]**

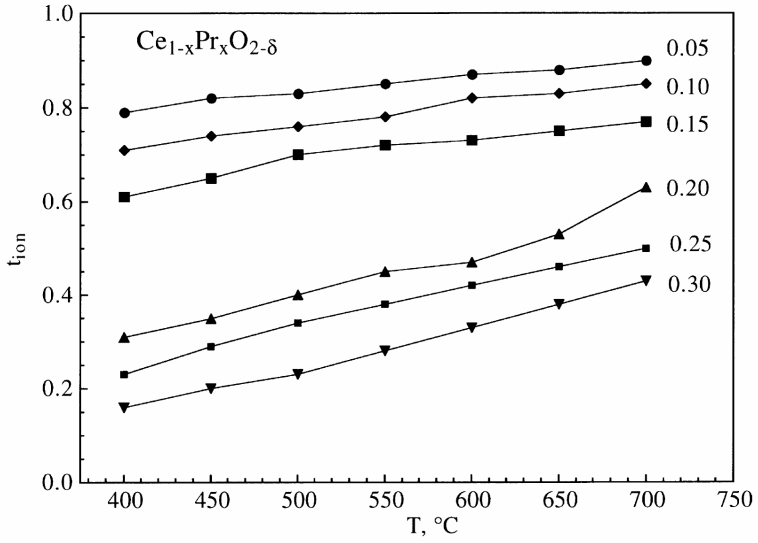


**Figure 1.13. Ionic transference numbers in PCO as determined by Shuk. [27]**

Porat and coworkers[36] examined electrical conductivity as a function of $pO_2$ in a 55% PCO sample. They observed a p-n transition in the material at low temperatures and relatively high $pO_2$ values (Figure 1.14). They attributed this transition to an impurity band conductivity, but did not extensively analyze their results. No detailed defect model was developed. In addition, Porat measured the total nonstoichiometry in 55% PCO. The results are shown in Figure 1.15. Based on the changes in slope observed, Porat suggested that the material passed through phase changes at the boundaries of the regions

marked I through IV on the plot of log($pO_2$) vs. nonstoichiometry. Changes in total nonstoichiometry at relatively fixed $pO_2$ values (in region II) are indicative of a two phase region and likely miscibility gap. Porat's work pointed to some of the interesting features present in the PCO system, but did not fully explore conductivity behavior in the material, nor did it present a defect model to describe the characteristics observed.

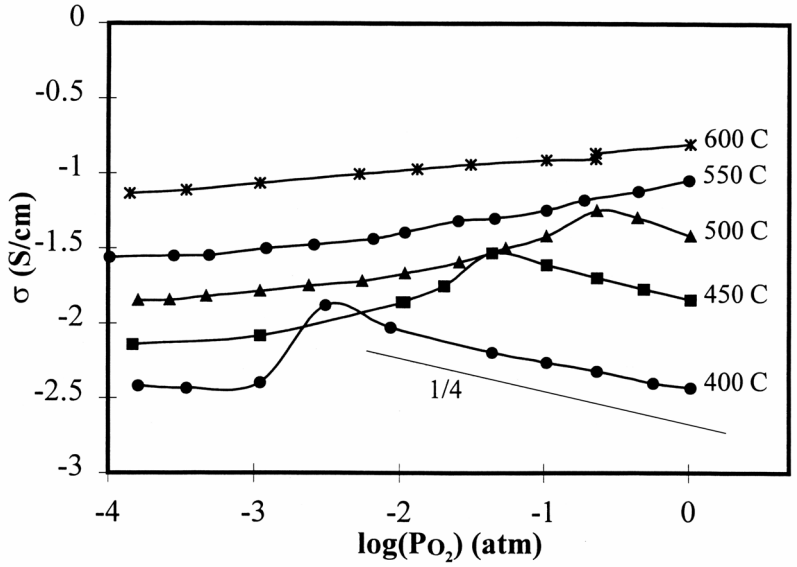


**Figure 1.14. Conductivity in $Pr_{0.55}Ce_{0.45}O_{2-\delta}$ as a function of $pO_2$ determined by Porat.[36]**

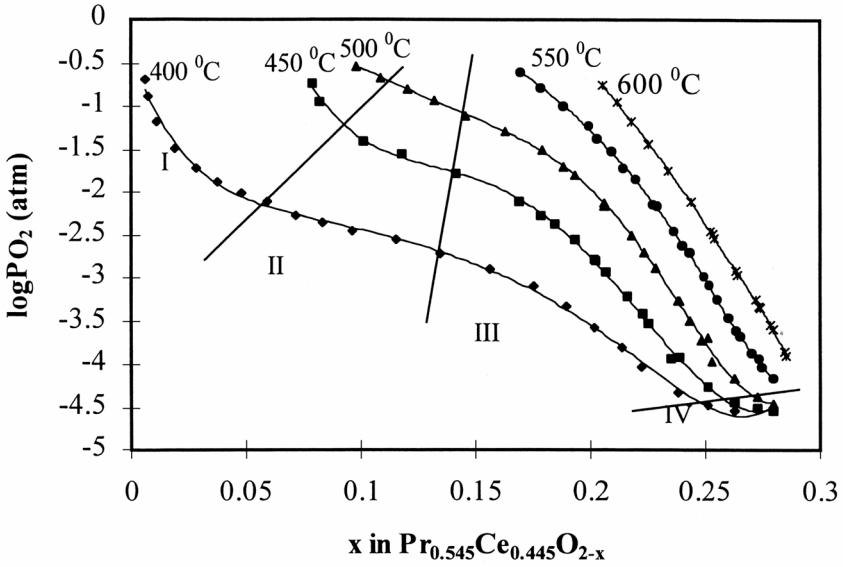


**Figure 1.15. Nonstoichiometry in $Pr_{0.55}Ce_{0.45}O_{2-\delta}$ as determined by Porat.[36]**

A number of published works examine the large amounts of nonstoichiometry possible in heavily doped PCO.[45,58,59] These works point to the interest in the large oxygen storage capability of the system, but typically do not address defect chemical issues. Knauth and Tuller[45] performed nonstoichiometry measurements in a 70% PCO sample and extracted diffusion coefficients based on relaxation during electrochemical titration. They found a reduction enthalpy for the system of approximately 2.9eV. Other studies were only interested in total evolution of oxygen per unit mass of PCO (for compressor and three way catalyst applications).

Several studies have examined very low doping of gadolinia-ceria solid electrolytes (3% Pr or less).[16,22-24] This work stemmed primarily from a patent[60] which suggested that a double doping scheme using low levels of Pr might further suppress electronic conductivity in the solid electrolyte. In general the double-doping scheme was found to be ineffective. These studies are outside the realm of interest of the work presented here.

## *1.4. Conclusions of the Literature Review*

While a significant number of studies exist, no authors have systematically examined conductivity in praseodymium-cerium oxide solid solutions. The high total conductivity, mixed conductivity, and high nonstoichiometry make it an attractive candidate for a host of applications, though a basic understanding of conductivity in the system and an accurate defect model have not been devised.

## Chapter 2. Objectives

There is a clear opportunity to contribute to the understanding of electrical conductivity and defect transport in the PCO system. The goal of this work was to obtain systematic conductivity data as a function of $pO_2$, temperature, and Pr content in PCO and understand those results in terms of the defect chemical equilibria in the system. Suitable experimental characterization techniques were identified and executed in order to collect useful conductivity data at temperatures between 600 and 1000C°. A defect model was developed and quantitatively fit to the experimental data. Thermodynamic parameters that govern conductivity in the system were determined and their temperature dependence was obtained. The model developed is capable of identifying individual components of the total conductivity in the system and their dependence on $pO_2$ and temperature.

Coulometric titration measurements were performed in order to directly measure the nonstoichiometry in PCO. The nonstoichiometry data was then compared to that obtained via electrical conductivity measurements as a verification of the parameters derived.

The compositions investigated during this study included Pr contents of up to 20%. The literature suggested that these percentages of PCO would exist as single phase materials, allowing accurate defect models to be developed. Studies of materials in this composition range also allowed reference to and comparison with the wealth of information previously studied in the field of doped ceria electrolytes.

Not only was this study an opportunity to clarify the mechanisms of defect formation and transport in a technologically relevant material, it provided a model platform on which to study the effects of high concentrations of multivalent dopant cations in oxide semiconductors. It is hoped that the results can be transferred to other such systems.

# Chapter 3. Experimental Details

## *3.1. Sample Preparation*

### 3.1.1. Oxalate Precipitation

Powders of praseodymium cerium oxide were produced using a wet-chemical coprecipitation route, as previously described by several other researchers.[30,58,61] This technique offers a number of advantages over traditional mixed oxide processing methods. In the solid oxide powder preparation method, precursor oxides (or carbonates, sulfates, chlorides, etc) are mixed in the powder state, then calcined at high temperature in order to promote reaction and diffusion between the various phases, producing the desired single phase material. If diffusion is slow in the precursors or in the desired phase, such a reaction may not be completed uniformly. If mixing of the initial precursor powders is insufficient, inhomogeneities in the final powder will result. In addition, the high calcining temperatures required result in a final agglomerated powder with large particle/grain size and relatively low reactivity for sintering.

Coprecipitation processing offers intimate mixing of precursors in solution prior to the precipitation of an insoluble phase. The resulting precipitate is then calcined to decompose organics, drive off water of hydration, etc. The temperatures required for such calcination are much lower than those used in mixed oxide processing, often resulting in less grain growth and more reactive powders.

In these studies, cerium nitrate and praseodymium nitrate were added to oxalic acid to form insoluble oxalate salts. Figure 3.1 shows a flow chart of the steps employed during the coprecipitation process. For compositions containing 1% or less Pr, high purity $Ce(NO_3)_3 \cdot 6H_2O$ was used (99.99%, Alfa-Aesar[62] #11330). For samples with greater Pr levels, a lower purity $Ce(NO_3)_3 \cdot 6H_2O$ was used (99.5%, Alfa-Aesar[62] #11329). The $Pr(NO_3)_3 \cdot xH_2O$ used in all Pr containing samples was 99.9% pure (Alfa-Aesar[62] #12909). As the nitrates are hygroscopic and very difficult to weigh accurately, stock solutions were made using deionized water in concentrations of approximately 2.5M.

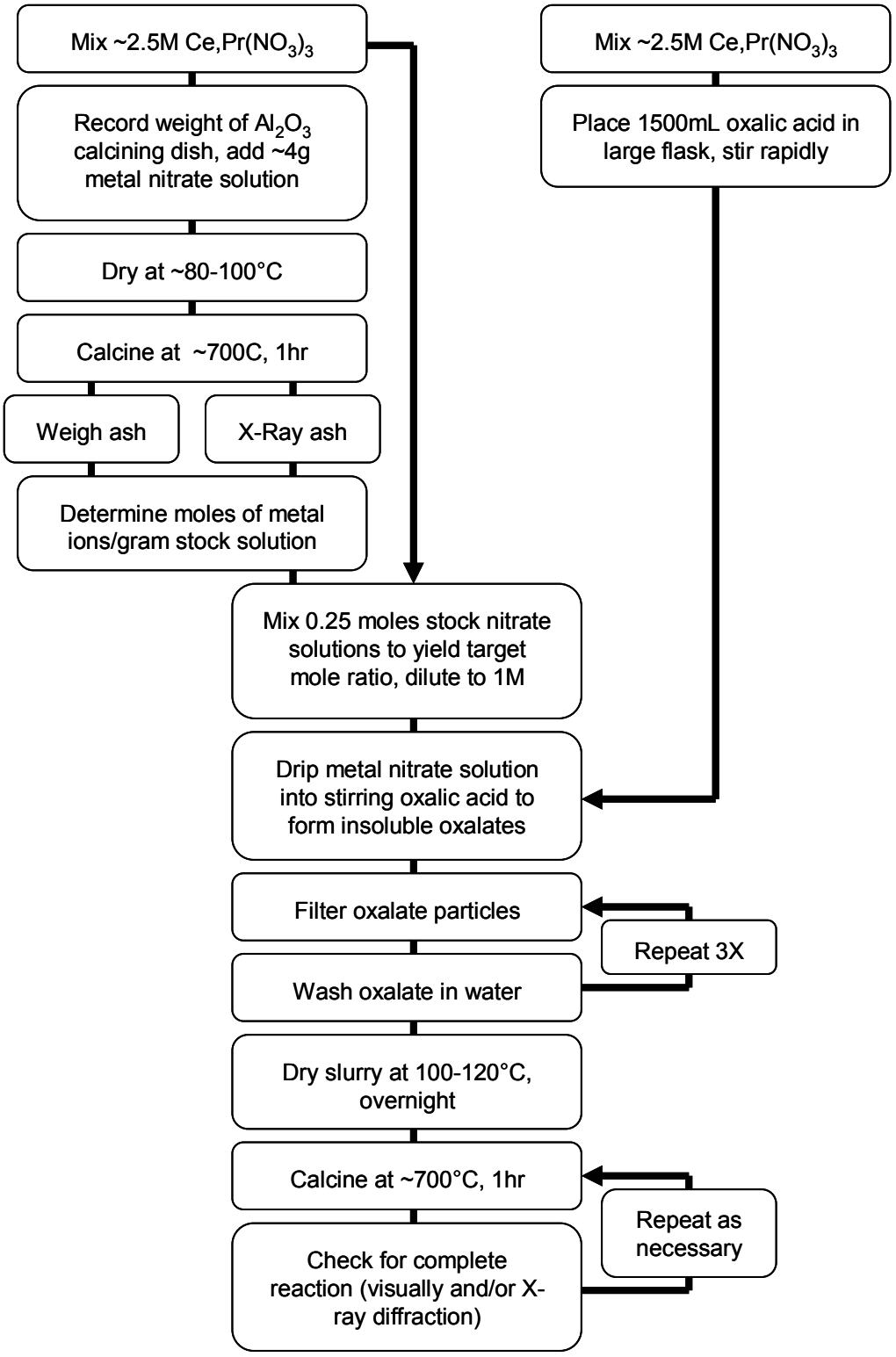


**Figure 3.1. A flow diagram of the coprecipitation process used to create the $Pr_xCe_{1-x}O_{2-\delta}$ materials examined during this study.**

Initially, stock solutions were calibrated using a colorimetric titration technique[63] (yielding results on a volume basis). This method was both inconvenient and inaccurate, so a mass calibration technique was adopted. A given amount of stock solution was weighed into a calcining dish, dried, and fired to 700°C in order to fully decompose the nitrate, yielding a pure oxide phase. Pure $CeO_2$ and $Pr_6O_{11}$ were identified as the phases present after calcining using X-ray diffraction (see below for a description of the diffraction experiment). Based on the mass yield of oxide from each stock solution, the concentrations of the stock solutions were accurately determined.

Solutions for precipitation were prepared by weighing a total of 0.25 moles of $Ce/Pr(NO_3)_3$ from stock solutions and diluting the mixture to 250 mL total volume with deionized water (yielding a concentration of approximately 1M metal nitrate). A 0.5M oxalic acid solution was prepared from dry oxalic acid, $H_2C_2O_4$ (Alfa-Aesar[62] #33262) and deionized water and allowed to warm up to room temperature (dissolution of oxalic acid in water is endothermic). 1500 mL of this oxalic acid solution was placed in a 2 L Erlenmeyer flask and stirred using a cross-shaped stir bar on a magnetic stir plate such that a deep vortex formed. The 1M metal nitrate solution was then dripped into the flask from a 500 mL burette. The total amount of oxalate ion required for the complete precipitation of $(Ce/Pr)_2(C_2O_4)_3$ is 1.5 times the total amount of metal ions in solution or 0.25 moles x 1.5 = 0.375 moles oxalate. An excess of twice as much oxalate as stoichiometrically required (0.75 moles of oxalate total) was used to ensure immediate and complete precipitation upon the addition of metal nitrate solution.

Upon completion of precipitation, the slurry of oxalate powder was vacuum filtered through a 1μm paper filter using a standard faucet-type vacuum aspirator and filtering flask. The oxalate cake was then re-dispersed in deionized water and filtered to rinse excess oxalic acid from the powder. This rinsing step was repeated three times. The oxalate slurry was then placed in a polypropylene bottle and allowed to settle overnight. Excess liquid was decanted and the remaining slurry was placed in a cylindrical aluminum oxide crucible. After drying at 100°C, the oxalates were calcined to 700°C for one hour (the heating rate used was approximately 10°C/min). After calcining, if any evidence of oxalate still remained (either visually or by X-ray diffraction), the calcining

step was repeated. The maximum calcining temperature used was limited to 700°C to avoid significant grain growth.

### 3.1.2. Pellet Pressing and Sintering

Pellets of PCO samples were prepared using a combination of uniaxial and isostatic pressing. A 0.75" diameter hardened steel pressing die was coated with stearic acid by swabbing with a solution of stearic acid in acetone. Approximately 7g of powder was loaded into the die and was pressed to 2000 pounds using a Carver[64] model M 25 ton press, yielding a net pressure of 4500 psi (31 MPa). No binder was used. The resulting pellets were loaded into a polyethylene bag (Consolidated Plastics[65] #89983), evacuated using a faucet-type sink aspirator, and heat sealed with an impulse sealer. The sealed samples were then isostatically pressed to 40,000 psi (275 MPa).

The pellets were placed on a bed powder of identical composition in a zirconia tray, loaded into a Lindberg[66] #54434 tube furnace, and a mechanical pump was used to evacuate the sintering tube to approximately 1 mTorr base pressure. It was found that sintering without evacuation resulted in frequent cracking of the pellets, especially those containing more than 5% Pr. A possible explanation for this cracking will be offered with respect to the defect chemistry of the material in the discussion section.

### 3.1.3. Bar Sample Preparation and Mounting

A rectangular bar shaped specimen was cut from each pellet for use in electrical measurements using a Buehler[67] low speed cutting saw. The approximate dimensions of each bar were 3mm x 3mm x 10mm. Notches were cut into the bars in order to hold wires used to contact the samples. A layer of platinum ink (Eglehard[68] #6082), thinned using ethyl acetate (Alfa-Aesar[62] #42957), was then applied to form 4 contacts to the bar sample. The two end contacts were extended to cover the end of the bar, while the two center contacts were simply painted around the exterior. The samples were then wrapped with platinum wire leads and another layer of platinum ink was applied to ensure good contact. Each sample was wired with 4 leads for conductivity measurements. In addition, two type S thermocouple leads (Pt/10%Rh) were welded to the Pt wires at each end of the sample in order to accurately measure both the sample temperature and the thermal

gradient across the same at any given time. See Figure 3.2 for a diagram of the sample wiring. Each of the leads connected to the sample was fed through a separate bore of a 2' long, 0.25" diameter 6-bore alumina tube. The leads were sealed to the alumina tube at the end opposite the sample using silicone sealant.

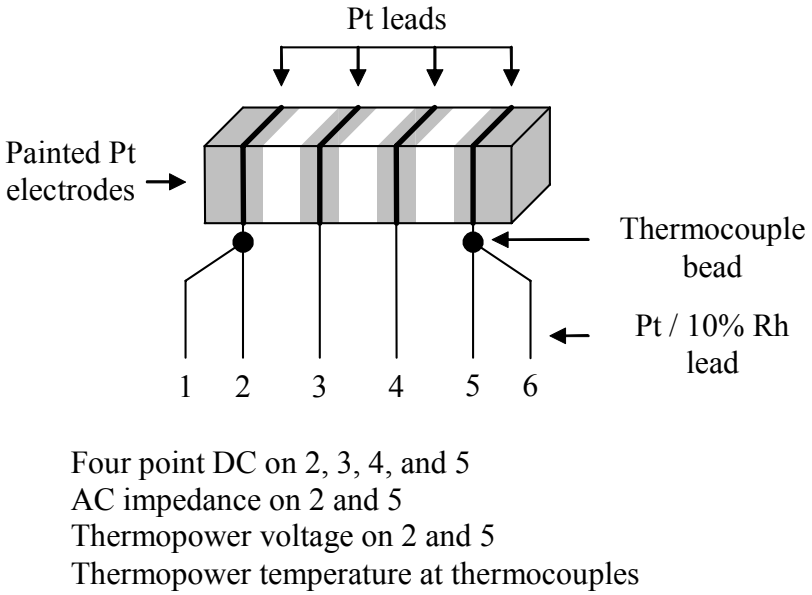


**Figure 3.2. A schematic of the wiring configuration used for electrical experiments during this study.**

Three samples were mounted to each of two specially designed end caps sized to a 2" outside diameter furnace tube. Each end cap was designed to resemble a compression fitting similar to a Cajon Ultra-Torr[69] fitting machined from aluminum. A silicone o-ring was used for resistance to heat conducted from the furnace by the furnace tube. Electrical connection panels holding thermocouple connectors and BNC breakouts were attached to each end cap. Each platinum lead from the sample was attached to the corresponding connector using either a screw connector (thermocouples) or a solder joint (BNC connectors). In addition, a 0.25" diameter zirconia oxygen sensor was inserted through the center of one end cap (between the three mounted samples), and a resistance heater was inserted through the center of the opposite end cap. Finally, a gas inlet/outlet was connected to each end cap. See Figure 1.4 for a picture of the end caps used for sample mounting and of the mounted samples. The two end caps, loaded and wired with samples, were inserted into opposite ends of a triple zone furnace (Lindberg[66] #STF55346C-1).

Fans were installed to help dissipate heat conducted through the furnace tube to the end caps.

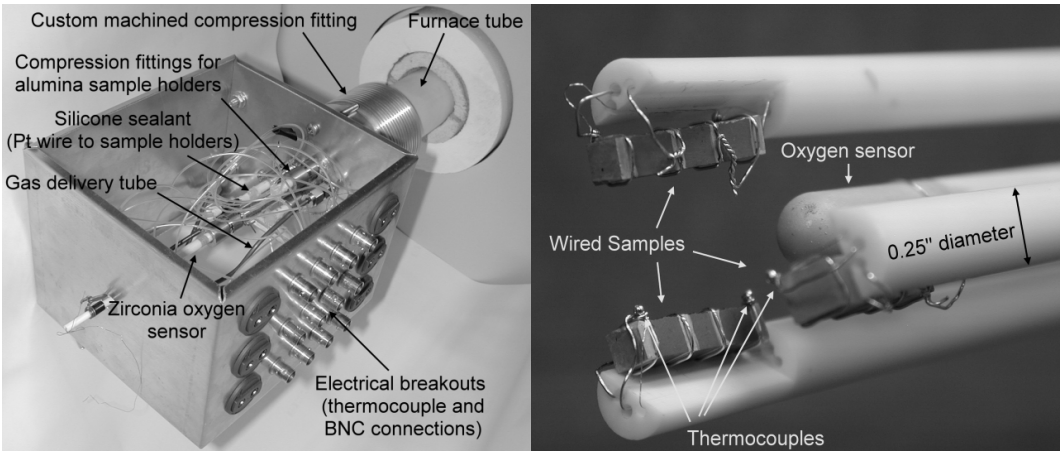


**Figure 3.3. Picture of the end caps used to mount and contact the conductivity samples used in these experiments (left) and of the wired samples (right).**

## *3.2. Physical Characterization*

### 3.2.1. Scanning Electron Microscopy - SEM

SEM micrographs of the bar and powder samples used during this experiment were taken using a Hitachi[70] #S-530 SEM in order to observe microstructures in the materials. The samples were gold or carbon coated prior to analysis in order to avoid charging under the impinging electron beam. The accelerating voltage used was 25kV. Both fracture surfaces and polished samples were examined. In addition, images of the PCO powder obtained via the coprecipitation route were collected in order to gauge the agglomerate size in the starting powder.

### 3.2.2. Optical Microscopy

Optical micrographs of selected sintered specimens were collected using an Olympus[71] BX51 microscope equipped with polarizing reflected light illumination, a Wollaston prism for collection of differential interference contrast (DIC) images, and a high resolution digital imaging system. DIC imaging enhances surface relief on the specimen, resulting in a 3-dimensional effect when observing surface roughness. Samples observed using optical microscopy were first polished flat using metallographic sample preparation techniques to a final smoothness of 0.25 μm diamond grit.

### 3.2.3. X-ray Diffraction

X-Ray diffraction was used for phase identification and crystallite size estimation at several points during powder and pellet processing and for lattice constant determination of fired PCO samples. A Rigaku[72] rotating anode source and 210mm diffractometer were used. Copper $K_\alpha$ radiation was generated with an accelerating voltage of 60kV and current of 300mA. The diffraction and scatter slits used were 0.5° wide, while the receiving slit was 0.15°. Jade software[73] was used in conjunction with the JCPDF database[74] in order to identify phases, measure peak broadening to estimate crystallite size, and determine lattice parameters. Powder samples were either mounted on double-sided tape on a piece of a glass slide and then mounted into an aluminum sample holder using a small piece of modeling clay or packed into a recess in an aluminum holder. Bulk ceramic pieces were cut and ground to produce a flat side, then mounted on double stick tape in the same way as powder samples. See Figure 3.4 for a diagram of the sample mounts used during X-ray analysis.

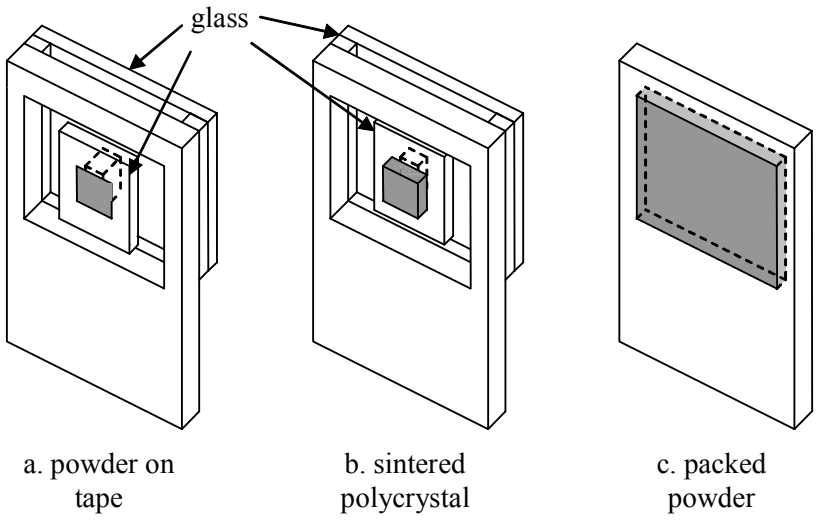


**Figure 3.4. Specimen holders used during X-ray analysis. The diffraction plane is flush with the face of the aluminum sample holder in all cases. In (a), a small amount of powder is held on double sided tape on a piece of a glass slide, then mounted to the holder using modeling clay. In (b), a polycrystalline sample replaces the powder in (a). In (c), loose powder is packed into a depression in the aluminum holder.**

### 3.2.4. Wavelength Dispersive Spectroscopy

Wavelength dispersive spectroscopy (WDS) was used for verification of the chemical composition of PCO samples produced during this study. A JEOL[75] electron microprobe (JXA-733 Superprobe) was used for these analyses. The system is essentially a scanning electron microscope equipped with several X-ray diffractometers (each one designed to cover a specific wavelength range). The impingement of the electron beam on the sample generates characteristic X-rays, and the X-rays are then spectrally analyzed and matched against calibration standards, yielding a high accuracy elemental analysis. Samples were polished flat to 0.25 μm using diamond grit in preparation for the microprobe. A coating of carbon was applied to avoid charging of the samples under the impinging electron beam. The accelerating voltage used was 15 kV and the beam current was held constant at 10nA. Calibration of the instrument was performed immediately prior to analysis using cerium and praseodymium phosphate standards.

## *3.3. $pO_2$ Control*

### 3.3.1. Limitations of $CO/CO_2$ Mixes at Low Temperature

The study of defect chemistry in oxides is commonly performed at temperatures greater than 800°C where standard buffer gas mixtures can be used to obtain a relatively continuous range of $pO_2$ values. The temperature range of interest in this study, however, was considerably lower (600-850°C). Using the least reducing mixture of $CO/CO_2$ readily available (100ppm CO / balance $CO_2$), the maximum $pO_2$ which can be achieved is approximately $2x10^{-17}$ atm at 600°C. Pure Ar yields a $pO_2$ of $10^{-4}$-$10^{-5}$ atm in a perfectly leak-tight system. This leaves a wide range of pO2 values inaccessible. Figure 3.5 shows a graph of the inaccessible $pO_2$ range as a function of temperature.

The $pO_2$ range of interest during this study was approximately 1atm to $1x10^{-15}$ atm. At 600°C, this leaves nearly the entire range of interest unreachable using $CO/CO_2$ buffer gases. While this range of inaccessible $pO_2$ decreases at higher temperatures, clearly mixed buffer gas control of $pO_2$ is insufficient for defect chemical studies at reduced temperatures.

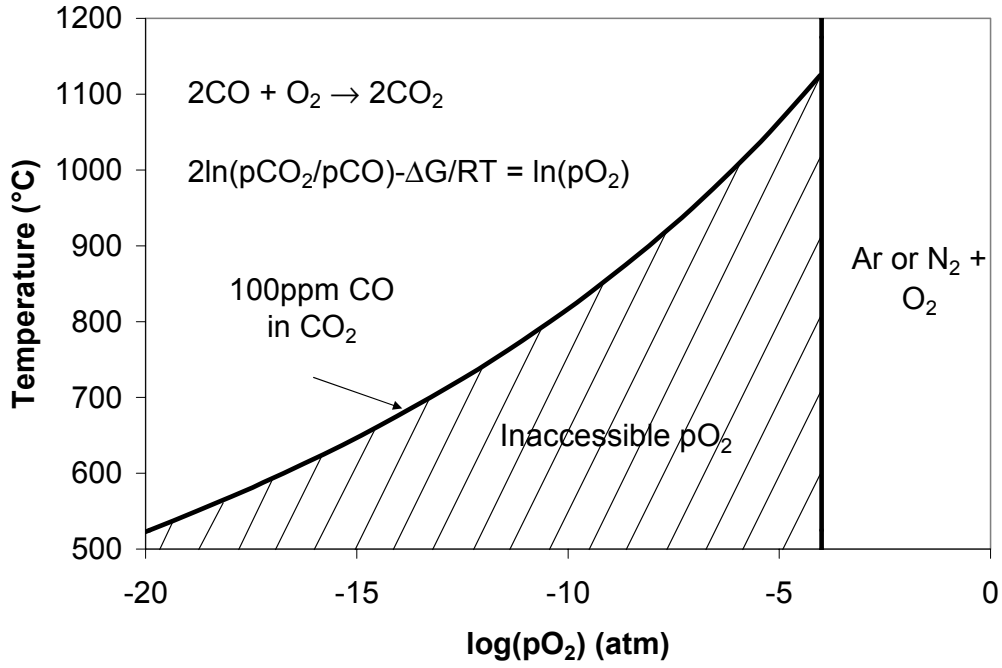


**Figure 3.5. Different regions of oxygen partial pressure control. Above $10^{-4}$ atm, $Ar/O_2$ mixtures can be used. The 100ppm CO in $CO_2$ line represents the maximum $pO_2$ which can be achieved using readily available gas mixtures. This leaves a wide range of inaccessible $pO_2$ values, especially at low temperatures.**

### 3.3.2. The Zirconia Oxygen Pump

In order to control $pO_2$ values in the $10^{-15}$-$10^{-4}$ atm regime at lower temperatures, a zirconia oxygen pump was used to electrochemically control the amount of oxygen pumped into a carrier gas. A zirconia tube, 0.75" OD, was electroded along the length of the tube, both inside and out, using platinum ink (Englehard[68] #6082). The inner electrode was painted around the end of the tube and a short length along the outside so that a wire could be wrapped on the outside of the tube to contact the inner electrode. The tube was fitted with Swagelock end caps using Teflon ferrules (Swagelock[69] #B-1210-6-4, #T-1213-1, #T-1214-1) and heated to 900°C in a tube furnace (Lindberg[66] #TF55035A-1). Initially, argon gas was flowed through the tube and a current was applied to the electrodes to draw oxygen out of the argon gas flow. The gas stream then passed into a second tube furnace at 700°C containing a zirconia oxygen sensor (a Nernst cell). From there, the gas was flowed into the sample furnace. While similar systems have been used previously, [76] the furnace containing the samples was insufficiently leak

tight to hold the $pO_2$ set by the pump. Although the external zirconia sensor indicated that low $pO_2$ values could be achieved, the $pO_2$ in the sample furnace could not be decreased below approximately $1x10^{-5}$ atm. Many attempts were made to more completely seal the sample furnace, but the desired $pO_2$ values were never achieved using argon as the carrier gas.

In order to circumvent this leak-proofing problem, the argon gas was replaced with a 1000ppm CO in $CO_2$ buffer gas mixture. The equilibrium $pO_2$ for this gas mixture is very low (approximately $2x10^{-19}$ atm). However, when oxygen is pumped into the gas stream with the zirconia pump, the equilibrium $pO_2$ can be varied continuously from $10^{-19}$ to $10^{-4}$ atm. Very fine control of the current applied to the oxygen pump must be maintained (on the order of 1nA variations of a total current of 1-3mA, or 1ppm, were required) and continuous feedback must be applied in order to accurately control such a system. A LabVIEW[77] routine was written in order to provide such dynamic feedback and control. An EDC[78] 520A source was used as pump control current source, and the pump voltage and input from the controlling oxygen sensor (located in the sample furnace) were measured using an HP[79] 3478A multimeter multiplexed with an HP[79] 34701A data switch. See Figure 3.6 for a schematic of the oxygen pump design.

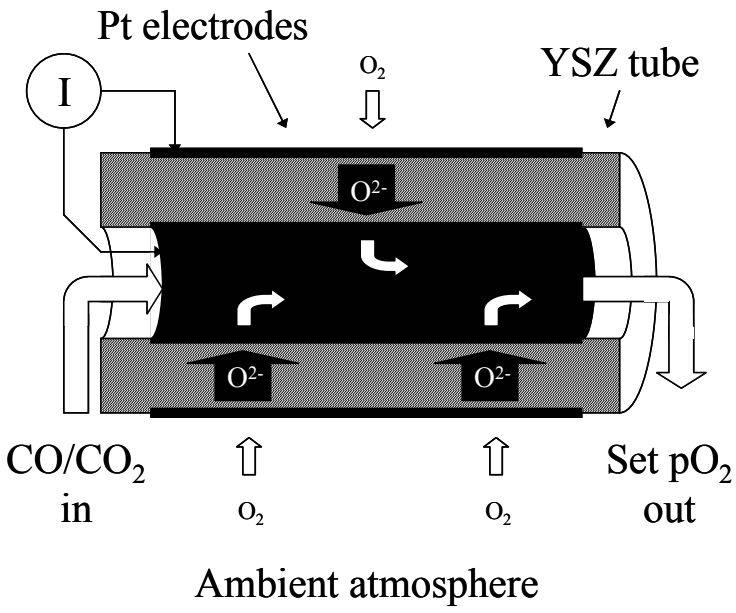


**Figure 3.6. A diagram of the oxygen pump used to control intermediate $pO_2$ values at low temperatures.**

### 3.3.3. Pump Control Algorithm

At its most basic level, controlling an oxygen pump is an easy task. If the $pO_2$ produced by the pump is too high, the pump current is altered such that the amount of oxygen pumped into the gas stream is decreased. If the $pO_2$ is too low, more oxygen is pumped in. In practice, however, several details complicate this scenario. There is a significant time lag between a change in pump current and the resulting change in $pO_2$, dependent on the flow rate used and the total volume of the system. As more and more oxygen is added to the $CO/CO_2$ mixture flowing through the system, the buffering capability of the gas decreases. As a result, at some given pump current (and corresponding $pO_2$, all the buffer is exhausted and very abrupt changes in $pO_2$ per change in pump current result. Polarization of the zirconia pump itself may contribute to irregular response. The total voltage on the pump must be held low enough to avoid reduction of the zirconia electrolyte. Control of such a sensitive system is not easy and requires a comprehensive system of control.

The pump used in the study was controlled using a dynamic feedback routine written in LabVIEW.[77] The $pO_2$ was measured and compared to the target $pO_2$ value at a given

interval (3 minutes for the system used in these experiments). Appropriate changes in pump current were applied in order to decrease difference in the measured and target $pO_2$. Changes in pump current and the time interval between these changes both scaled with the difference between the measured and target $pO_2$ values. Before each $pO_2$ update, the voltage on the oxygen pump was measured. This voltage was limited to a maximum of approximately 1.1V to avoid reduction of the zirconia pump. See Figure 3.7 for a flow diagram of the oxygen pressure control algorithm used during these studies.

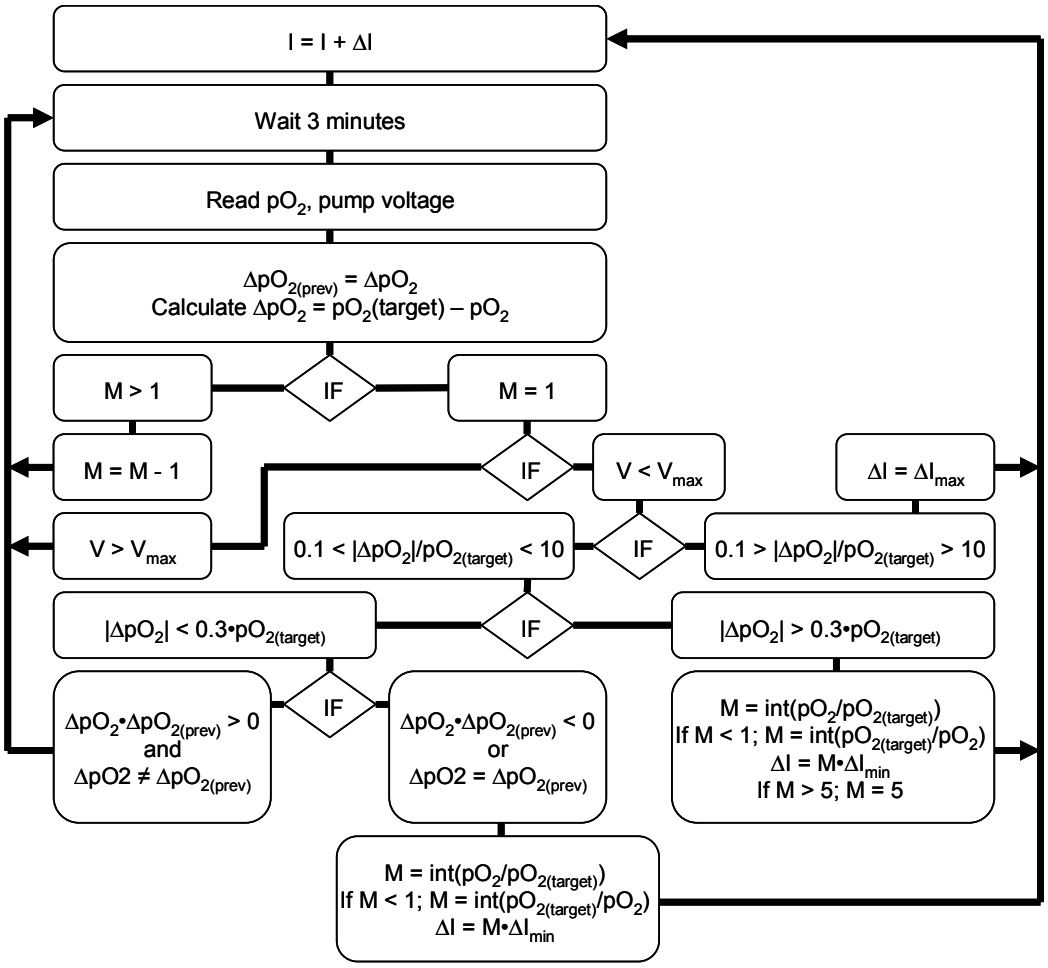


**Figure 3.7. Flow diagram of the algorithm used to control the oxygen pump during conductivity experiments. Note that I is the pump control current and M is a loop counter.**

Overall, the control routine for the oxygen pump was rather complex and required both a significant amount of "fine tuning" to the control algorithm and a certain degree of experience in order to chose the proper parameters to yield control at a given partial

pressure. While functional, more sophisticated control algorithms are commonly used in industrial controls (PID temperature controllers for furnaces, for instance). If further work with an oxygen pump is to be performed, it is recommended that an auto-tuning PID temperature controller equipped with a linear voltage input (from the oxygen sensor) and a 0-20mA control output (such as an Omega[80] #CN8261-FH1) be examined as an oxygen pump control. These controllers are relatively inexpensive (considerably less expensive than the current source/multimeter combination used to control the pump in these experiments) and may even offer more flexible control of the pump than a non-PID control routine.

## *3.4. Electrical Measurements*

### 3.4.1. DC Conductivity

The primary characterization technique used in this study was DC electrical conductivity. In four point measurements, current is applied to the sample under test through one set of leads and voltage is measured through a separate set of contacts. The current passing through the voltage measurement leads is essentially zero and therefore there is no resistance drop (R=I/V) at the contacts, ensuring that imperfect contacts do not interfere with the measurement of material properties.

Samples were wired as shown in Figure 3.2. See Figure 3.8 for a schematic of the furnace setup. The furnace temperature was set and balanced using the zones of a triple zone furnace. The temperature range examined during this study was 600-850°C. Each sample had a thermocouple at both ends, allowing the thermal gradient on the samples to be accurately measured and compensated. At each temperature measured, the furnace was adjusted such that no greater than a 1°C difference existed between the ends of each sample. The $pO_2$ was controlled using either an $Ar/O_2$ gas mixture ($pO_2 > 1x10^{-4}$ atm) or 1000 ppm CO in $CO_2$ adjusted using an oxygen pump ($pO_2 \leq 1x10^{-4}$ atm) as previously described. The furnace temperature and $pO_2$ were measured and recorded at intervals of 15 minutes to monitor the stability of the experimental conditions.

The average temperature and a single measurement of four point resistance at a source current of 1μA was measured for each sample at 15 minute intervals. A plot of resistance

vs. time was recorded for each sample to ensure that equilibrium values had been achieved prior to collection of an I-V sweep. Conditions were maintained and the sample allowed to equilibrate until the resistance of all 6 samples varied only within the experimental noise of the system and/or corresponded directly to small temperature and $pO_2$ variations. For instance, occasionally the temperature of the samples would change by a few degrees as the balance between different zones of the triple zone furnace shifted slightly. If the result was an overall increase in sample temperature, the resistance decreased slightly. Such small variations did not appreciably change the value of the measured resistance and were considered to be part of the experimental noise.

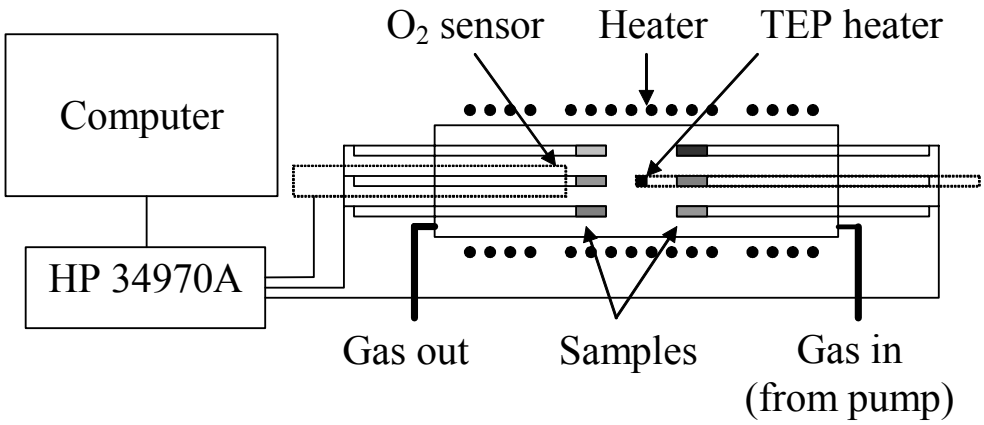


**Figure 3.8. Schematic of the furnace configuration used for simultaneous data collection from six samples.**

Once equilibrium had been achieved, an I-V sweep was performed. The source current was scanned from 1μA to 0.5mA using a logarithmic step spacing so that several values were collected at low currents, to avoid polarization of the sample, but some points were taken under high load to rigorously examine the ohmic behavior of the resistance. Low currents were measured first so that polarization was minimized for the majority of the data points measured. Both positive and negative polarities were collected, with a wait time of 20-30 seconds under no applied current before measurement of the reverse polarity. Each current value (forward and reverse polarity) was measured on each of six samples in succession prior to moving on to the next highest current, providing ample time to allow the sample to relax between collection of points in the I-V sweep. The

resistance value reported in the results section are those taken from a slope of the complete I-V curve. If any non-ohmic behavior was observed at the high current values, the points were deleted prior to calculation of the slope. Non-ohmic behavior was seldom observed. The conductivity of each sample ($\sigma$) was calculated using the relationship $\sigma = l/RA$ where l is the length between the sensing leads on the sample, A is the cross sectional area, and R is the measured resistance.

### 3.4.2. AC Impedance

AC impedance spectroscopy allows the total impedance of a sample to be separated into a number of frequency dependent components. The imaginary part of the impedance is plotted vs. the real resistance over a range of frequencies. An idealized spectrum exhibits distinct, isolated semicircles that correspond to different components in the total impedance of the measured specimen (such as bulk impedance, grain boundary impedance, contact impedance, etc). See Figure 3.9 for an idealized impedance spectrum and equivalent circuit model. Real spectra are often more convoluted, such that several semicircles overlap one another to form the spectrum. Appropriate modeling of the impedance can then be employed to isolate the individual components in the spectrum.

A Solartron[81] 1260 frequency response analyzer was used to collect AC impedance spectra at selected values of $pO_2$ and temperature in order to verify that the values obtained during four point resistance measurements were, in fact, the bulk conductivity values anticipated. Such measurements required a manual reconfiguration of the experimental wiring and were therefore not performed automatically at every $pO_2$ and temperature examined. An oscillation amplitude of 10mV was applied over a frequency range of 1Hz to 10MHz. Impedance spectra were collected using a range of applied DC bias varying from 0 to 0.5V. Equilibrium was verified via the four point DC measurement taken every 15 minutes. In many cases, the conductivity of the samples was too high to yield reliable impedance data. The resistance of the test leads, inductance of the cabling, etc, was comparable or greater than the resistance/capacitance of the sample being tested. For the lowest levels of Pr doping, where higher resistances resulted, AC impedance measurements could be correlated with the DC resistance values obtained.

### 3.4.3. Thermoelectric Power

The Seebeck coefficient or thermoelectric power of a material is the magnitude of the voltage that develops per unit of applied temperature gradient. The thermoelectric power of a number of semiconductors and ionic conductors has been examined by a number of authors.[82-89] In general, the thermoelectric power is related to both the charge and concentration of the charge carriers and, in the case of ionic conductors, to the entropy of oxygen in the gas phase. Combined with conductivity data, thermopower measurements can be used to obtain the mobilities of charge carriers in a material. Thermoelectric power data was collected over the same range of $pO_2$ and temperature as the DC resistance measurements in order to calculate carrier concentrations.

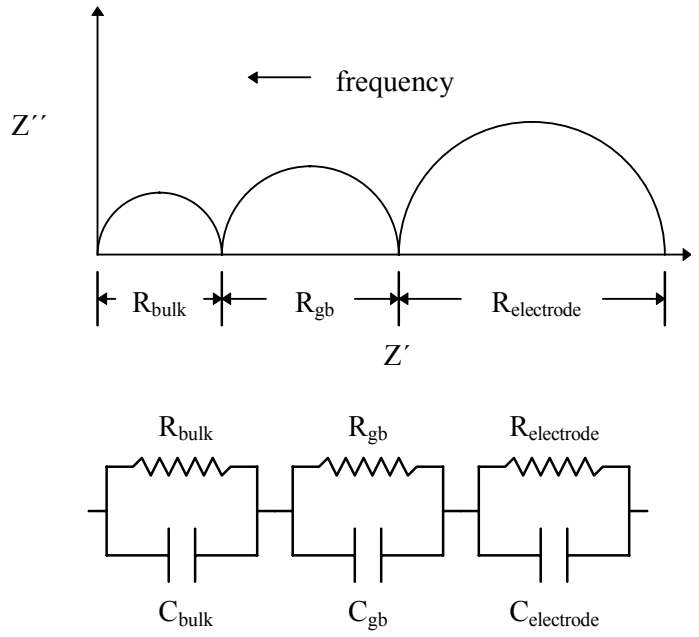


**Figure 3.9. An idealized impedance spectrum and equivalent circuit model consisting of bulk, grain boundary, and electrode effects from a polycrystalline ceramic sample.**

Following collection of resistance data, a thermal gradient was applied to the samples using a pulse heater located at the center of the furnace. The voltage difference that developed on the samples was measured as a function of this temperature gradient. The slope of the voltage vs. temperature plot that results (dV/dT) is the Seebeck coefficient or

thermoelectric power. Two schemes for measuring this value were examined. First, a brief heating pulse was applied for a short period of time, with the voltage being measured as the resulting thermal gradient decayed. This technique was found to produce relatively noisy results. A steady-state measurement was devised in which the power to the pulse heater was maintained at different levels for several minutes, then the resulting voltage and temperature difference on each sample was measured while the heater power remained fixed. This produced a much more stable thermopower value than the impulse technique.

## *3.5. Coulometric Titration*

Coulometric titration was used to measure the amount of oxygen evolved by powder PCO samples as a function of temperature and $pO_2$. Unlike conductivity measurements, all oxygen species are accounted for in such measurements, not only the charged species, as is the case in electrical conductivity testing. Samples are sealed in a closed volume and oxygen is removed from the system electrochemically. The total charge passed through the electrolyte in the closed cell can be converted into the total quantity of oxygen removed from the cell. The $pO_2$ that results after removal of a given amount of oxygen can be measured, yielding total nonstoichiometry in the oxide as a function of $pO_2$.

### 3.5.1. Experimental Setup

The experimental setup used during these studies was modeled after that of Schneider and coworkers[90]. A small zirconia crucible was electroded inside and out using platinum ink (Englehard[68] #6082). These electrodes were used to measure the difference in partial pressure between the external atmosphere (air) and the internal $pO_2$. A weighed mass of as-calcined PCO powder was placed into an alumina crucible and sealed inside the zirconia crucible using a zirconia lid (also electroded inside and out) and a glass seal. The electrodes on the lid were used to electrochemically remove oxygen from the cell. The alumina crucible prevented exposure of the powder to the glass sealing material. The integrated charge removed from the system (I•t) can then be converted to an equivalent amount of oxygen removed from the cell using equation (3.1) where F is Faraday's constant, $t_1$ and $t_2$ are the start time and end time of application of a current (I),

V is the "dead volume" of the cell, R is the gas constant, T is absolute temperature, and $P_1$ and $P_2$ are the oxygen partial pressure at the beginning and end of the application of current.. See Figure 3.10 for a diagram of the experimental setup.

$$moles\ O_2 \approx \left( \frac{1}{4F} \int_{t_1}^{t_2} Idt \right) - \left( \frac{V}{RT}(P_1 - P_2) \right) \qquad (3.1)$$

Identification of the appropriate glass for use as the sealing material was challenging. Ideally, a glass with a softening point above the maximum measurement temperature should be used such that diffusion of oxygen through the seal is low, but the thermal expansion must be close to that of zirconia (approximately $113x10^{-7}$ per °C[91])in order to avoid cracking upon cooling from the fusing temperature. In general, lowering the softening temperature of a glass also increases its thermal expansion. As a result, a high expansion glass with a high softening point is not easily obtained. The maximum temperature at which conductivity measurements were made was 850°C. No glasses with a softening temperature this high had suitable expansion coefficients. As a result, a lower temperature glass with high expansion was used and the range of measurement was limited to lower temperatures than those used in the conductivity studies (500-750°C). The glass seal was tested by sealing an empty crucible, electrochemically pumping it to a very low $pO_2$ value ($<1x10^{-20}$ atm), then monitoring the $pO_2$ in the cell as a function of time. At temperatures up to 700°C, the leakage rate was slow enough that the background pressure only increased to $1x10^{-10}$ atm over several days of monitoring. As the $pO_2$ range of interest in this study was only from atmospheric pressure to approximately $1x10^{-5}$ atm, this leak rate was several orders of magnitude below the range of interest in the study and was assumed to be negligible.

The seal was applied as a paste of Elan[92] #13 glass frit dispersed in water using a paint brush. The entire cell was then heated to 1000°C to fuse the glass, cooled to room temperature and examined for holes or cracks in the seal. It should be noted that while contacts to the inner electrodes were made by painting the electrodes through the glass seal (as in Figure 3.10), it is important to completely seal such metal electrodes from the external environment in order to avoid shorting the oxide ion conductor between the

inside and outside of the cell. Once properly sealed, the cells were wired with platinum wires and transferred to another furnace for measurements at temperatures of 500-750°C.

### 3.5.2. Titration Control Algorithm

The total amount of charge (current integrated over time) removed from each titration cell must be monitored and recorded during a coulometric titration experiment. In addition, the total voltage applied to the titration cell must be kept low enough to avoid electrolytic reduction of the zirconia electrolyte. If the voltage on the cell is too low, however, pumping times will be inordinately long, leading to errors due to very slow leaks in the seal or leakage of very low currents that result (nanoamps). The system should also be able to dynamically adapt to speed up or slow down the pumping process in order to achieve the most efficient measurement cycle possible.

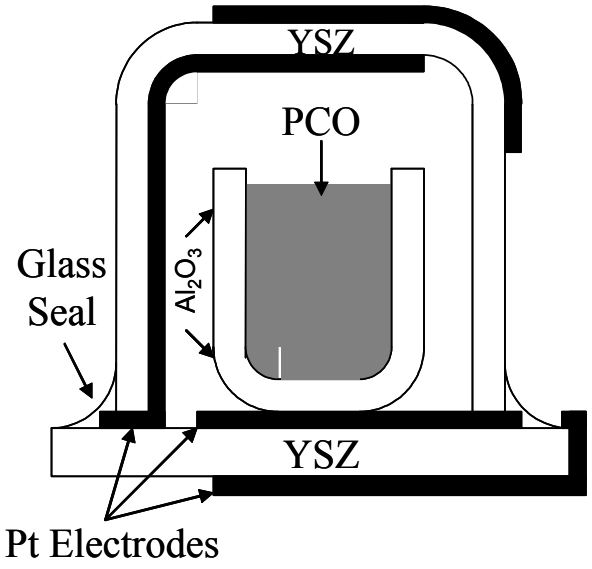


**Figure 3.10. Schematic of the coulometric titration setup. The alumina crucible serves to protect the sample from any glass that may leak through to the inside of the zirconia cell. Note that all inner Pt electrodes are covered by the glass seal when exposed to the external atmosphere.**

Six titration cells were placed in a triple zone furnace and the furnace was adjusted to minimize temperature gradients from one sample to the next. Based on the geometrically defined volume of the titration cell, the total charge removal to decrease the $pO_2$ by a predetermined step (typically one tenth to one quarter of an order of magnitude change in

$pO_2$) in an empty cell was calculated. This amount of charge was pumped from the cell at a current calculated such that the total cell voltage would not exceed 0.9V. The resulting change in $pO_2$ was measured, and if the desired step had not been achieved, the amount of charge previously removed was doubled and pumped from the cell. Eventually, the successively larger removals of charge resulted in the desired $pO_2$ change. A new initial value of charge to be removed was then calculated, based again on the assumption of an empty cell, and the process was repeated until the target $pO_2$ (typically $1x10^{-5}$ atm) was achieved.

Rather than applying continuous removal of charge until one sample reached the desired step in $pO_2$, a given step was applied to each sample in succession, leaving time between successive applications of current for the sample to equilibrate with the surrounding atmosphere, for the cell to de-polarize, etc.

The voltage of the cell was monitored during each application of current. If the cell voltage exceeded 0.9V, pumping was immediately stopped and the cell was allowed to equilibrate while other cells were pumped. The value of the effective resistance of the pump was used to determine the appropriate value of pump current to apply to the cell in successive applications of current. If the voltage on the cell increased slowly as a constant current was applied (due to an increase in the Nernst potential of the cell as oxygen was removed or polarization of the cell), the current was decreased in an attempt to keep the voltage from exceeding 0.9V. Likewise, if the current applied resulted in a very low pump voltage, the current applied was increased in order to speed pumping. See Figure 3.11 for a flow diagram of the algorithm used to perform coulometric titration experiments.

It should be noted that at low $pO_2$ values, the Nernst voltage across the pump electrodes increased, limiting the ability to remove oxygen from the cell (since only small currents could be applied without exceeding the 0.9V limit to avoid reduction of the zirconia cell). If it were necessary to study nonstoichiometry at low $pO_2$ values, a similar setup could be used, however placing the cells in an furnace controlled at lower $pO_2$ (close to that of the

samples) would decrease the $pO_2$ difference and therefore the Nernst voltage on the cell and thereby allow higher pump currents and faster titration.

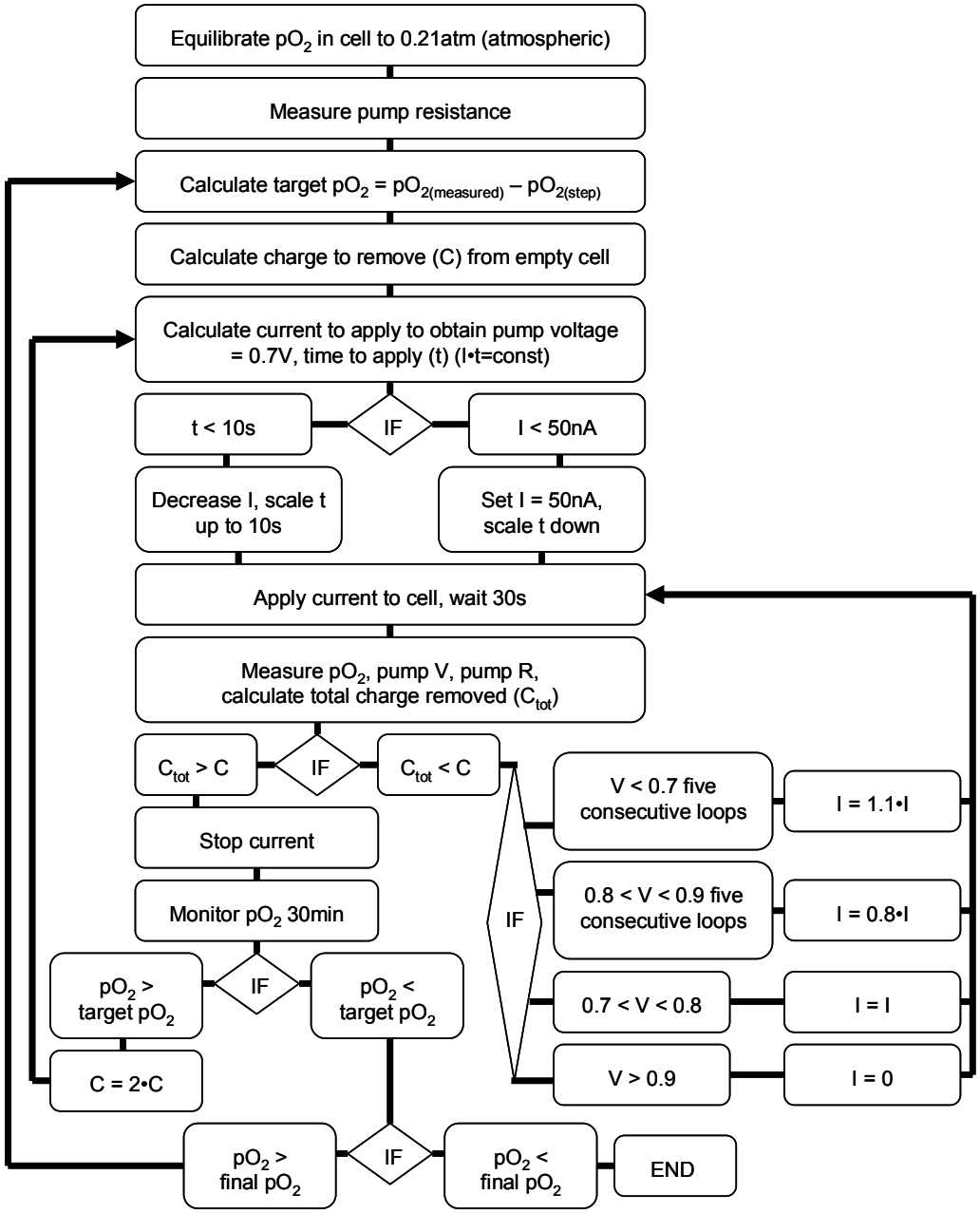


**Figure 3.11. Flow diagram of the algorithm used to perform coulometric titration experiments.**

# Chapter 4. Defect Modeling

Electrical conductivity in oxide semiconductors consists of both electronic and ionic conduction. Depending on the temperature, oxygen partial pressure, and the intrinsic defect mechanisms of the material, conductivity may be dominated by electrons, holes, oxygen vacancies, oxygen interstitials, metal vacancies, metal interstitials, defect complexes, etc. More often, the total conductivity consists of a combination of the motion of several different components rather than being completely determined by one type of carrier exclusively.

In general, the conductivity of a given species is the product of the charge on the given species ($Z_i e$), the carrier concentration ([i]), and the carrier mobility ($\mu_i$), as given in equation (4.1). The carrier mobility is generally not $pO_2$ dependent and the charge on the carrier is fixed; therefore, the experimentally observed variation in conductivity with $pO_2$ is a function of the carrier concentration. It is therefore necessary to examine the thermodynamic relationships between the experimental conditions and the concentrations of charge carrying defects in order to develop a model to describe conductivity in an oxide system.

$$\sigma_i = Z_i e[i]\mu_i \tag{4.1}$$

## *4.1. "Pure" $CeO_2$*

Pure cerium oxide ($CeO_2$) is the host material for solid solutions of praseodymium-cerium oxide (PCO), therefore the defect chemistry of nominally undoped $CeO_2$ will first be examined. The crystal structure of $CeO_2$ is cubic fluorite. It is known that the intrinsic ionic disorder in this material occurs by a Frenkel mechanism, that is, an oxygen ion moves from a lattice position to an interstitial position, creating anion vacancy and interstitial pairs. Cation defects are not believed to form in significant concentrations in the fluorite structure and will not be considered further here. Using standard Kroeger-Vink notation, The Frenkel mechanism is summarized in equation (4.2), where $K_F(T)$ is the reaction constant governing the reaction.

$$O_O^{\,x} \rightarrow V_O^{\bullet\bullet} + O_i^{//}; \quad [V_O^{\bullet\bullet}][O_i^{//}] = K_F(T) \tag{4.2}$$

Intrinsic electron-hole pair generation may occur by thermal excitation over the band gap by equation (4.3) where n and p are the concentrations of electrons and holes, respectively, and $K_e(T)$ is the reaction constant for the reaction.

$$nil \rightarrow e' + h^{\bullet}; \quad np = K_e(T) \tag{4.3}$$

Oxygen can be removed from the host material, generating oxygen vacancies and charge compensated by the formation of free electrons, as shown in equation (4.4), where $K_R(T)$ is the reduction constant.

$$O_O^{\,x} \rightarrow \tfrac{1}{2}O_2(g) + V_O^{\bullet\bullet} + 2e'; \quad [V_O^{\bullet\bullet}]n^2 pO_2^{1/2} = K_R(T) \tag{4.4}$$

These free electrons will be localized on Ce ions and hopping conduction will then occur over the $Ce^{3+}/Ce^{4+}$ sub-lattice.

In addition, there are always some impurities at low levels in the background of pure $CeO_2$. Many fixed valence acceptor cations (such as $Ca^{2+}$, $Y^{3+}$, $Gd^{3+}$, $Sr^{2+}$, etc.) have high solubility in $CeO_2$ and are impossible to eliminate completely. We shall assume trivalent background acceptors for the sake of this discussion (though divalent acceptors do not alter the analysis). Incorporation of these impurities into the host material results in the formation of oxygen vacancies according to equation (4.5).

$$A_2O_3 \xrightarrow{CeO_2} 2A_{Ce}^{\prime} + 3O_O^{\,x} + V_O^{\bullet\bullet} \tag{4.5}$$

In order to satisfy electroneutrality, the total positive species in the material must equal the sum of all negative species. Equation (4.6) demonstrates this charge balance for $CeO_2$.

$$2[O_i^{//}] + n + [A_{Ce}^{\prime}] = 2[V_O^{\bullet\bullet}] + p \tag{4.6}$$

At high $pO_2$ values, hole hopping conduction may be significant, but under reducing conditions, the concentration of both oxygen interstitials and holes will be negligible. Therefore, we may simplify the electroneutrality equation to equation (4.7).

$$n + [A_{Ce}^{/}] \approx 2[V_O^{\cdot\cdot}] \tag{4.7}$$

Under highly reducing conditions, the concentrations of electrons and vacancies will overwhelm that of background acceptors, as indicated in equation (4.4). In this case, the electroneutrality equation simplifies even further to equation (4.8)

$$n \approx 2[V_O^{\cdot\cdot}] \tag{4.8}$$

which when combined with equation (4.4) yields the concentration of vacancies or electrons in terms of $pO_2$ and the reduction constant $K_R$. The concentrations of electrons and vacancies are on the same order of magnitude, therefore the conductivity will be dominated by electrons (since the mobility of electrons is generally much higher than that of vacancies). The concentration of electrons is then given by equation (4.9).

$$n \approx \sqrt[3]{2K_R}\, pO_2^{-1/6} \tag{4.9}$$

Under less reducing conditions, the concentration of vacancies is dominated by the background acceptor concentration, simplifying electroneutrality to equation (4.10)

$$[A_{Ce}^{/}] \approx 2[V_O^{\cdot\cdot}] \tag{4.10}$$

and combining equation (4.4) and (4.10) yields the concentration of electrons in the extrinsically defined region as in equation (4.11).

$$n \approx \sqrt{\frac{2K_R}{[A_{Ce}^{/}]}}\, pO_2^{-1/4} \tag{4.11}$$

The relative mobilities of the two charge carrying species (electrons and vacancies) determine the transition between electronic and ionic conductivity in the extrinsically doped regime. The concentration of holes may also be calculated by combining equations (4.3) and (4.11) to yield equation (4.12).

$$p \approx K_e \sqrt{\frac{[A_{Ce}^{/}]}{2K_R}}\, pO_2^{+1/4} \tag{4.12}$$

Under extremely oxidizing conditions, it is theoretically possible that the concentration of oxygen interstitials will overwhelm the extrinsically fixed vacancy concentration and

result in a region of conductivity dominated by intrinsically generated holes, but these conditions are not observed experimentally and will therefore not be further examined.

With equations (4.8) through (4.12), the concentrations of the dominant charge carriers are defined over a wide range of $pO_2$ values. Assuming $pO_2$ independent mobilities for all carriers, the expected trends in conductivity can then be plotted. Figure 4.1 shows the expected variation in conductivity in nominally undoped $CeO_2$ based on the model described.

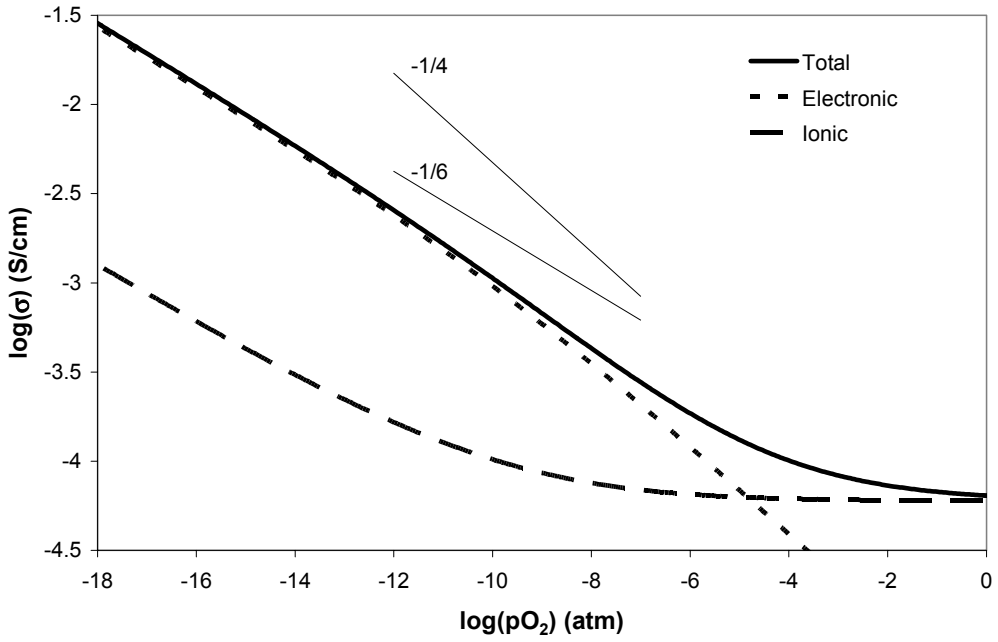


**Figure 4.1. Predicted conductivity behavior in nominally undoped $CeO_2$. Background impurities yield the ionic plateau in conductivity at high $pO_2$ values.**

## *4.2. Praseodymium-Cerium Oxide*

The primary difference between the defect chemistry of undoped $CeO_2$ and that of Pr doped ceria is that the background acceptors, previously assumed to be of fixed valence, are multivalent in the case of Pr. Pr, like Ce, exists in both a $Pr^{3+}$ and $Pr^{4+}$ state, but Pr is significantly more reducible than Ce, resulting in valence changes at high $pO_2$, rather than the low $pO_2$ values required to reduce $Ce^{4+}$ to $Ce^{3+}$.

Equations (4.2) through (4.4) still apply in the case of praseodymium-cerium oxide (PCO). In addition, the ionization of $Pr^{3+}$ to $Pr^{4+}$ must be accounted for, as described in equation (4.13), where $K_{Pr}(T)$ is the praseodymium ionization constant in PCO. Further, the total mass of Pr in the system must be conserved, as in equation (4.14).

$$Pr_{Ce}^{/} \rightarrow Pr_{Ce}^{x} + e'; \quad \frac{[Pr_{Ce}^{x}]n}{[Pr_{Ce}^{/}]} = K_{Pr}(T) \tag{4.13}$$

$$[Pr_{Ce}^{/}] + [Pr_{Ce}^{x}] = [Pr_{Ce(total)}] = Pr_{tot} \tag{4.14}$$

The addition of Pr to the system adds one more unique charged defect ($Pr_{Ce}^{/}$) to the electroneutrality condition as shown in equation (4.15).

$$2[O_i^{//}] + n + [Pr_{Ce}^{/}] + [A_{Ce}^{/}] = 2[V_O^{\cdot\cdot}] + p \tag{4.15}$$

Equations (4.2) through (4.4) and (4.13) through (4.15) constitute a system of six equations and six unknowns and, in theory, it should be possible to determine all defect concentrations analytically. In reality, the solution to this system is not easily obtained (even symbolic math software packages such as Maple[93] cannot determine an analytical solution). In addition, all the reaction constants corresponding to the various defect equations would have to be fitted in any application of an analytical solution. The likelihood of obtaining an accurate fit using six reaction constants and several mobilities as fitting parameters is very low. In order to simplify the task at hand, the assumption that oxygen interstitials and holes are both negligible contributions to the total conductivity will be made. As Pr enhances overall reduction in $CeO_2$, the concentration of oxygen vacancies will be high (suppressing the concentration of interstitials according to equation (4.2), and ensuring high ionic conductivity, overwhelming p-type electronic conductivity at high $pO_2$). The resulting electroneutrality condition is given in equation (4.16).

$$n + [Pr_{Ce}^{/}] + [A_{Ce}^{/}] \approx 2[V_O^{\cdot\cdot}] \tag{4.16}$$

Even with this simplification, an analytic solution for each defect concentration in terms of $pO_2$ cannot be written. A solution for the concentration of each defect in terms of n can be found, however, as can an expression for $pO_2$.[94] This $pO_2(n)$ is somewhat less

convenient than $n(pO_2)$ since the experimentally controlled variable in conductivity experiments is $pO_2$, but numerical methods can be applied in order fit such a model to the data.

The concentration of oxygen vacancies is given in equation (4.4) as:

$$[V_O^{\cdot\cdot}] = \frac{K_R}{n^2} pO_2^{-1/2} \tag{4.17}$$

The concentration of $Pr_{Ce}^{/}$ may be found by combining equations (4.13) and (4.14):

$$[Pr_{Ce}^{/}] = \frac{[Pr_{Ce}^{x}]n}{K_{Pr}} = \frac{nPr_{tot} - n[Pr_{Ce}^{/}]}{K_{Pr}};$$

$$[Pr_{Ce}^{/}]K_{Pr} = nPr_{tot} - n[Pr_{Ce}^{/}];$$

$$nPr_{tot} = (K_{Pr} + n)[Pr_{Ce}^{/}];$$

$$[Pr_{Ce}^{/}] = \frac{nPr_{tot}}{K_{Pr} + n} \tag{4.18}$$

The concentration of $Pr_{Ce}^{x}$ is then defined using equation (4.14):

$$[Pr_{Ce}^{x}] = Pr_{tot} - [Pr_{Ce}^{/}] = Pr_{tot}\left(1 - \frac{n}{K_{Pr} + n}\right) = \frac{Pr_{tot}K_{Pr}}{K_{Pr} + n} \tag{4.19}$$

Finally, using equation (4.16) and the relationships previously derived, $pO_2$ may be solved for in terms of n:

$$n + [Pr_{Ce}^{/}] + [A_{Ce}^{/}] \approx 2[V_O^{\cdot\cdot}]; \tag{4.16}$$

$$n = \frac{2K_R pO_2^{-1/2}}{n^2} - \frac{nPr_{tot}}{n + K_{Pr}} - [A_{Ce}^{/}];$$

$$n \bullet pO_2^{1/2} + \frac{nPr_{tot}}{n + K_{Pr}} pO_2^{1/2} - \frac{2K_R}{n^2} + [A_{Ce}^{/}]pO_2^{1/2} = 0;$$

$$pO_2^{1/2}\left(n + [A_{Ce}^{/}] + \frac{nPr_{tot}}{n + K_{Pr}}\right) = \frac{2K_R}{n^2};$$

$$pO_2^{1/2}\left(\frac{n(n+K_{Pr})}{n+K_{Pr}}+\frac{[A_{Ce}^{/}](n+K_{Pr})}{n+K_{Pr}}+\frac{nPr_{tot}}{n+K_{Pr}}\right)=\frac{2K_R}{n^2};$$

$$pO_2^{1/2}\left(\frac{(n+[A_{Ce}^{/}])(n+K_{Pr})}{n+K_{Pr}}+\frac{nPr_{tot}}{n+K_{Pr}}\right)=\frac{2K_R}{n^2};$$

$$pO_2=\left(\frac{2K_R}{n^2}\left(\frac{n+K_{Pr}}{(n+[A_{Ce}^{/}])(n+K_{Pr})+nPr_{tot}}\right)\right)^2 \qquad (4.20)$$

## *4.3. Polaron Hopping Conductivity and Impurity Band Formation*

Electronic conduction in ceria does not occur by the motion of free electrons. Electrons liberated through the reduction reaction given in equation (4.4) are localized on the cerium ions (effectively reducing $Ce^{4+}$ to $Ce^{3+}$). The result is a polaron, or the electron plus the lattice distortion resulting from the redistribution of ions around the excess electron at the $Ce^{3+}$ ion. In order for the electron to move, the lattice distortion must move with it. Tuller and Nowick[89] previously described small polaron hopping conduction in pure $CeO_2$. An outline of their analysis is presented below.

In an fcc lattice (such as the cerium sub-lattice in $CeO_2$), the drift mobility of charge carriers ($\mu$) is given as:

$$\mu=(1-c)ea^2\Gamma/kT \qquad (4.21)$$

where e is the elementary charge, k is the Boltzman constant, a is a geometric lattice parameter, and c is the fractional occupancy of electrons trapped on Ce ions (n/N where n is the number of $Ce^{3+}$ per unit volume and N is the volumetric density of cerium atoms in the material). $\Gamma$ is the jump rate of polarons from one site to another, given by equation (4.22)

$$\Gamma=P\upsilon_o exp\left(\frac{-E_H}{kT}\right) \qquad (4.22)$$

where $\nu_o$ is the phonon jump frequency, $E_H$ is the activation energy for hopping, and P is the probability of electron transfer after the polaron's lattice distortion has moved to an adjacent site. In the adiabatic case, where the time for the motion of lattice distortions is

much greater than the time required for electron transfer, P ≈ 1. In such a case, the conductivity can be written, according to equation (4.1) as:

$$\sigma_{polaron} = \frac{Ne^2 a^2 \upsilon_o c(1-c)exp(-E_H/kT)}{kT} = \frac{B}{T} Nc(1-c)exp(-E_H/kT) \qquad (4.23)$$

Note that here the concentration of charge carriers is Nc, and the mobility is defined as:

$$\mu_{polaron} = \frac{ea^2 \upsilon_o (1-c)}{kT} exp(-E_H/kT) \qquad (4.24)$$

The overall conductivity in a polaron conductor follows a concentration dependence of c(1-c). Not only does there have to be a charge carrier present to move (c), there also has to be a free location adjacent to it (1-c). The product c(1-c) is a parabolic function, maximized when the ratio of occupied states to unoccupied states is 1.

In modeling conductivity behavior in a polaron conductor, it is important to account for the concentration dependence of the system, as given in equation (4.23). At low concentrations of carriers, the term c(1-c) ≈ c. Such is the case for the reduction of the ceria host at low $pO_2$ values. Since c remains low, the concentration of electrons does not reach high enough values to make the c(1-c) behavior evident in the range of $pO_2$ values examined during this study. The concentration dependence observed is a simple proportionality, similar to that given in equation (4.1).

At low Pr concentrations, Pr behaves as a simple dopant in $CeO_2$. $Pr^{3+}$ is an acceptor compensated by the formation of oxygen ion vacancies, as given in equation (4.5). Increasing $Pr^{3+}$ concentration increases vacancy concentration and ionic conductivity. At high $pO_2$ values, however, $Pr^{3+}$ ions oxidize to $Pr^{4+}$, establishing another "sub-lattice" on which polaron hopping can occur. Praseodymia forms a solid solution with ceria. At low concentrations, the distance between Pr ions in the solution is large enough so that the probability of a polaron jump from one Pr to the next is very small (the lattice term a in equation (4.23) is very large). As the concentration of Pr increases, the distance from one Pr ion to the next decreases and the probability of polaron conduction increases. This can also be understood in terms of the band diagram. At low concentrations, discrete acceptor levels are introduced into the band gap of $CeO_2$ upon the addition of Pr. As the

Pr concentration increases, orbital overlap between the Pr levels becomes possible, leading to the formation of an impurity band within the $CeO_2$ band gap. The conductivity in that band is maximized when the band is half full, that is, when the ratio of $Pr^{3+}$ to $Pr^{4+}$ is 1. See Figure 4.2 for a band diagram schematic in PCO.

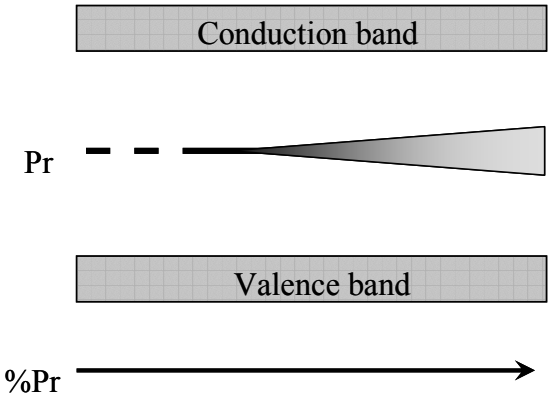


$$\sigma_H = \frac{B}{T}[Pr_{Ce,tot}]\frac{[Pr_{Ce}^{/}]}{[Pr_{Ce,tot}]}\frac{[Pr_{Ce}^{X}]}{[Pr_{Ce,tot}]}\exp\left(-E_H/kT\right)$$

(N) (c) (1-c)

**Figure 4.2. Band diagram of praseodymium doped cerium oxide. At low Pr concentrations, Pr acts as an acceptor in $CeO_2$. At sufficiently high concentrations, an impurity band may form as the orbitals of the "dopant" Pr ions begin to overlap.**

At low Pr concentrations, enhanced ionic conductivity will dominate the total conductivity of PCO solid solutions. As Pr content is increased, however, polaron hopping from one Pr ion to the next will add an electronic hopping component to the overall conductivity. This component will be maximized when the ratio of $Pr^{3+}$ to $Pr^{4+}$ is 1 and decrease as changes in $pO_2$ alter the ratio of Pr oxidation states. If the net electron hopping conductivity is comparable to the ionic conductivity, mixed electronic-ionic conduction results.

With the definitions of defect concentrations and $pO_2$ given in equations (4.17) through (4.20) and the Pr hopping conductivity defined in equation (4.23), it becomes possible to solve for a numerical fit to the experimental conductivity data. A running list of n values is created, with as fine a spacing as necessary to yield calculated $pO_2$ values in reasonable

agreement with experimentally measured values. Each experimental $pO_2$ value is matched with the nearest calculated $pO_2$ in the list, and the total conductivity at each point is calculated (using an arbitrary set of reaction constants and mobility values). The total error is calculated (as a sum of squares of the error at each point), then a given reaction constant or mobility is changed and the process repeated. The constant is changed until the sum of squares error is minimized, then the next constant is refined. Once all constants have been refined, the process is repeated. Eventually, the total error in the fit has been minimized by optimization of all reaction constants and mobilities, yielding the optimum set of fitting parameters for the given isotherm.

### *4.4. Anticipated Conductivity Behavior*

While it is not possible to solve for a closed form solution for defect concentrations in terms of $pO_2$, if specific simplified cases are examined, approximations for such relationships can be found. This process is the equivalent of making Brouwer approximations in order to find closed-form solutions for defect concentrations in simpler systems. Once approximations of the electron concentration are obtained, the corresponding vacancy concentration can be derived and total conductivity vs. $pO_2$ behavior in PCO can be predicted (assuming reasonable relationships between the magnitudes of the mobilities of electrons and vacancies).

Examination of equation (4.20) offers a number of obvious simplifying assumptions. For instance, if we assume that $n >> K_{Pr}$, then the expression for $pO_2$ simplifies to:

$$pO_2 \approx \left( \frac{2K_R}{n^2} \left( \frac{1}{n + [A_{Ce}^{/}] + Pr_{tot}} \right) \right)^2 \tag{4.25}$$

If it is also the case that $n >> [A_{Ce}^{/}]+Pr_{tot}$ then:

$$pO_2 \approx \left( \frac{2K_R}{n^2} \left( \frac{1}{n} \right) \right)^2 ; \quad n \approx \sqrt[3]{2K_R}\ pO_2^{-1/6} \tag{4.26}$$

which is identical to the case of pure ceria given in equation (4.9). Note that from equation (4.13) it is evident that if $n >> K_{Pr}$, then $[Pr_{Ce}^{/}] >> [Pr_{Ce}^{x}]$. The Pr in the system is nearly all reduced, implying low $pO_2$. The situation then simplifies to the case of pure

ceria with a trivalent dopant. At highly reducing conditions, where the concentration of free electrons in the system is greater than the concentrations of the total acceptor concentration ($n >> [A_{Ce}^{/}]+Pr_{tot}$), the dominant mechanism controlling electron concentration is reduction of the $CeO_2$ host material and is independent of the acceptor concentration. At less reducing conditions, such that $n >> K_{Pr}$ but $[A_{Ce}^{/}]+Pr_{tot} >> n$, the concentration of electrons reduces to:

$$pO_2 \approx \left( \frac{2K_R}{n^2} \left( \frac{1}{[A_{Ce}^{/}] + Pr_{tot}} \right) \right)^2; \quad n \approx \sqrt{\frac{2K_R}{[A_{Ce}^{/}] + Pr_{tot}}} \; pO_2^{-1/4} \tag{4.27}$$

which is identical to equation (4.11), the case where background acceptors determine the electronic conductivity in pure $CeO_2$ (again, provided that nearly all Pr is $Pr_{Ce}^{/}$).

In oxidizing conditions, $K_{Pr} >> n$ such that most Pr exists as $Pr^{4+}$. In this case, equation (4.20) simplifies to:

$$pO_2 \approx \left( \frac{2K_R}{n^2} \left( \frac{K_{Pr}}{K_{Pr}(n + [A_{Ce}^{/}]) + nPr_{tot}} \right) \right)^2 \tag{4.28}$$

If in addition $n >> [A_{Ce}^{/}]$ (the free electron concentration due to reduction of the Ce host material is significantly greater than the background acceptor concentration, as in the case of highly pure PCO), then:

$$pO_2 \approx \left( \frac{2K_R}{n^3} \frac{K_{Pr}}{K_{Pr} + Pr_{tot}} \right)^2 \tag{4.29}$$

Whether $K_{Pr} >> Pr_{tot}$ or $Pr_{tot} >> K_{Pr}$, the $pO_2$ dependence of carrier concentration is the same:

$$K_{Pr} >> Pr_{tot}: \quad pO_2 \approx \left( \frac{2K_R}{n^3} \right)^2; \quad n \approx \sqrt[3]{2K_R} \, pO_2^{-1/6} \tag{4.30}$$

$$Pr_{tot} >> K_{Pr}: \quad pO_2 \approx \left( \frac{2K_R}{n^3} \frac{K_{Pr}}{Pr_{tot}} \right)^2; \quad n \approx \sqrt[3]{\frac{2K_R K_{Pr}}{Pr_{tot}}} \, pO_2^{-1/6} \tag{4.31}$$

Note that equation (4.30) is simply the case of pure $CeO_2$, whereas equation (4.31) accounts for the valence change of Pr.

Finally, if $K_{Pr} >> n$ and $[A_{Ce}^{/}] >> n$ (most of the Pr is $Pr_{Ce}^{x}$ and the background acceptor concentration is larger than the free electron concentration), then equation (4.28) reduces to:

$$pO_2 \approx \left( \frac{2K_R}{n^2} \frac{K_{Pr}}{[A_{Ce}^{/}]K_{Pr} + nPr_{tot}} \right)^2 \tag{4.32}$$

and if $[A_{Ce}^{/}]K_{Pr} >> nPr_{tot}$ (such that the electrical behavior is dominated by background impurities, rather than Pr, then:

$$pO_2 \approx \left( \frac{2K_R}{n^2} \frac{1}{[A_{Ce}^{/}]} \right)^2; \quad n \approx \sqrt{\frac{2K_R}{[A_{Ce}^{/}]}} pO_2^{-1/4} \tag{4.33}$$

Notice that this is the same as equation (4.27) except that here it is assumed that $Pr_{tot}$ is negligible with respect to $[A_{Ce}^{/}]$. If, however, $nPr_{tot} >> [A_{Ce}^{/}]K_{Pr}$ (the effects of Pr in the system overwhelm the effects of the background acceptor concentration), the result is that:

$$pO_2 \approx \left( \frac{2K_R}{n^2} \frac{K_{Pr}}{nPr_{tot}} \right)^2; \quad n \approx \sqrt[3]{\frac{2K_R K_{Pr}}{Pr_{tot}}} pO_2^{-1/6} \tag{4.34}$$

Equation (4.34) is the same as equation (4.31). This is the relevant equation if $Pr_{tot}$ determines the electron concentration at high $pO_2$.

Using the relationships for $n(pO_2)$ derived in equations (4.25) through (4.34) and equation (4.17), $[V_O^{\bullet\bullet}]$ can be solved in terms of $pO_2$. With these concentrations, the $pO_2$ dependence of both the electronic and ionic conductivity can be determined. Figure 4.3 shows the anticipated electronic, ionic, and total conductivity behavior in PCO based on the model developed. Reduction of the $CeO_2$ material, oxidation of $Pr_{Ce}^{/}$ at high $pO_2$, and impurity band conduction are taken into consideration. Table 4.1 shows the relevant "Brouwer-type" assumptions and concentration of electrons and vacancies from low to high $pO_2$ values. The equations given assume that the compositions of PCO being

modeled are relatively pure such that [$A_{Ce}^{/}$] is low. The regions marked in Table 4.1 correspond to those identified in Figure 4.3.

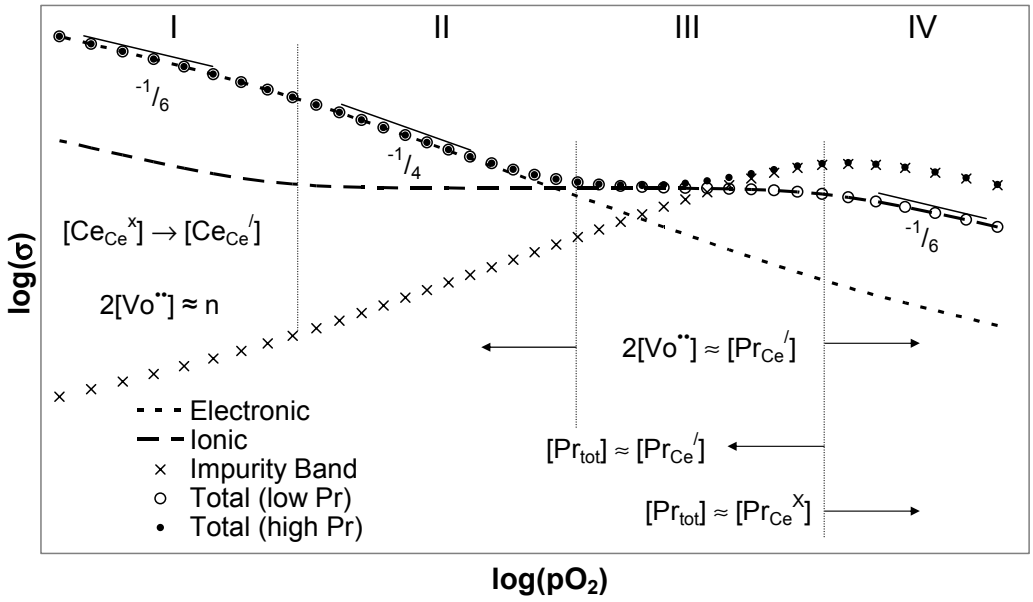


**Figure 4.3. Predicted conductivity behavior in $Pr_xCe_{1-x}O_{2-\delta}$. Regions marked I through IV correspond to the dominant defect regimes identified in Table 4.1.**

**Table 4.1. The relevant simplifying assumptions and defect concentrations for the various regions of conductivity behavior marked in Figure 4.3.**

| Region I | Region II | Region III | Region IV |
|---|---|---|---|
| $n >> K_{Pr}$<br>$[Pr_{Ce}^{/}] >> [Pr_{Ce}^{x}]$ | | | $K_{Pr} >> n$<br>$[Pr_{Ce}^{/}] >> [Pr_{Ce}^{x}]$ |
| $n >> [A_{Ce}^{/}]+Pr_{tot}$ | $[A_{Ce}^{/}]+Pr_{tot} >> n$ | | $[A_{Ce}^{/}] >> n$ (pure PCO) |
| $n \approx \sqrt[3]{2K_R}\ pO_2^{-1/6}$ | $n \approx \sqrt{\frac{2K_R}{[A_{Ce}^{/}]+Pr_{tot}}}\ pO_2^{-1/4}$ | | $n \approx \sqrt[3]{\frac{2K_RK_{Pr}}{Pr_{tot}}}pO_2^{-1/6}$ |
| $[V_O^{\cdot\cdot}] \approx \sqrt[3]{\frac{K_R}{4}}pO_2^{-1/6}$ | $[V_O^{\cdot\cdot}] \approx \frac{[A_{Ce}^{/}]+Pr_{tot}}{2}$ | | $[V_O^{\cdot\cdot}] \approx \sqrt[3]{\frac{K_RPr_{tot}^{2}}{4K_{Pr}^{2}}}pO_2^{-1/6}$ |
| $\sigma_e > \sigma_i$<br>$\sigma_e \propto pO_2^{-1/6}$ | $\sigma_e > \sigma_i$<br>$\sigma_e \propto pO_2^{-1/4}$ | $\sigma_i > \sigma_e$<br>$\sigma_i \propto [A_{Ce}^{/}]+Pr_{tot}$ | $\sigma_i > \sigma_e$<br>$\sigma_i \propto pO_2^{-1/6}$ |
| $\sigma_{e,Pr} \approx 0$ | | $\sigma_{e,Pr} = \frac{\sigma^{o}_{e,\mathrm{Pr}}}{T}Pr_{tot}\frac{[Pr_{Ce}^{x}]}{Pr_{tot}}\frac{[Pr_{Ce}^{/}]}{Pr_{tot}}exp\left(\frac{-E_H}{kT}\right)$ | |

# Chapter 5. Results

The results of this study will be presented here, with minimal analysis or interpretation of the results. Detailed discussion and analysis will be presented in the discussion chapter.

## *5.1. Physical Characterization*

Numerous techniques were used to characterize the physical attributes of both powder and sintered samples.

### 5.1.1. Electron Microprobe (Chemical Analysis)

A wavelength dispersive X-ray analyzer was used to measure the chemical compositions of the sintered samples analyzed during these studies. A series of samples was produced with nominal compositions of 0%, 0.5%, 1.0%, 5%, 10%, and 20% Pr (measured as an atom percent of the total cations in the $CeO_2$ host material). Based on the results of microprobe analysis, it is apparent that the 5% sample was replaced with a 10% sample, however, resulting in a duplicate sample. Table 5.1 shows the results of microprobe analysis for all samples used in this study, along with the certainty of each measurement. Samples will be referred to by the nominal composition batched in all further discussions. The precipitation route used to make the samples appears to be relatively accurate, though deviations from target compositions at low Pr percentages are obvious.

**Table 5.1. Microprobe compositional analysis of the conductivity samples characterized during these studies.**

| Batched %Pr | Measured %Pr | Measurement Uncertainty (%Pr) | Compositional difference (%) |
|---|---|---|---|
| 0 | 0.00 | 0.00 | 0 |
| 0.5 | 0.17 | 0.12 | -66 |
| 1 | 0.76 | 0.13 | -24 |
| 10 | 9.62 | 0.26 | -3.8 |
| 10 | 9.74 | 0.26 | -2.6 |
| 20 | 20.60 | 0.38 | +5 |

### 5.1.2. Scanning Electron Microscopy

Scanning electron micrographs of both powder and sintered samples were taken in order to characterize grain size, pore structure, and morphology. Selected micrographs of both

the cerium oxalate precursor powder and as calcined cerium oxide are shown in Figure 5.1. The apparent grain size of the powders is approximately 0.5-1 μm. X-ray analysis indicates that the ultimate crystallite size of the powders is much smaller, but the micrographs in Figure 5.1 indicate that these crystallites are agglomerated into much larger particles.

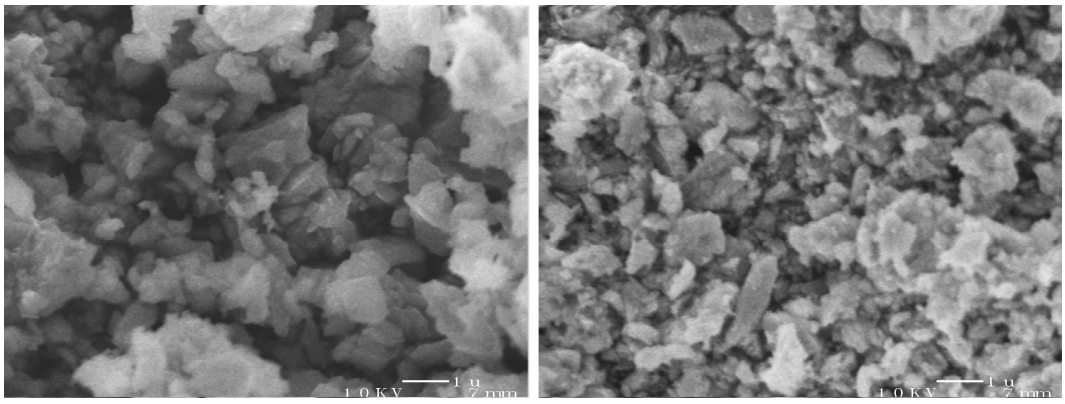

**Figure 5.1. SEM micrographs of cerium oxalate (right) and cerium oxide (left) produced by coprecipitation. The scale bar show is 1μm. The apparent agglomerate size of each powder is approximately 0.5-1μm.**

Micrographs of fracture surfaces of sintered specimens were collected. See Figure 5.2 for micrographs of the sintered specimens. The grain size of samples containing 1% or less Pr is approximately 5 μm. Trapped porosity is evident inside the grains of the material, indicating significant grain growth during sintering. Samples containing 10% or 20% Pr, however, demonstrate a smaller overall grain size (approximately 2 μm) and little or no trapped porosity (higher magnification shots were examined for trapped pores; none were observed). Grain growth and grain boundary motion was likely impeded in these samples by the high concentration of Pr ions in solution.

### 5.1.3. Optical Microscopy

Optical micrographs of polished sections were taken after collection of conductivity data. Figure 5.3 shows micrographs of the 1% and both 10% Pr samples. In samples containing 1% or less Pr, no cracks were observed after exposure to the temperature and $pO_2$ conditions of the conductivity studies. Samples of 10 and 20% Pr exhibited significant cracking on a scale of approximately 50 μm. This cracking alters the

conduction path through the material and therefore affects the conductivity values measured. The consequences of such cracking will be considered further in the discussion section.

### 5.1.4. X-Ray Diffraction

X-Ray diffractometry of the calcined powders was performed in order to verify initial phase purity and to obtain an estimate of the crystallite size in the material through the peak broadening analysis routine in Jade.[73] Figure 5.4 is a diffraction pattern for a representative sample. All peaks are identified as fluorite peaks. No peak splitting is observed. The amorphous "hump" at low angles is a result of the glass sample holder on which the powder sample was mounted for X-Ray analysis and is not characteristic of the sample itself. The peaks are relatively wide due to the small crystallite size of the powder. Based on this broadening (and assuming that no other factors contribute to the broadening, such as residual stress), the estimated grain size in the powders is approximately 20 nm. Nitrogen adsorption experiments (BET) on the same powders yielded similar results for the ultimate crystallite size of the oxide powders.

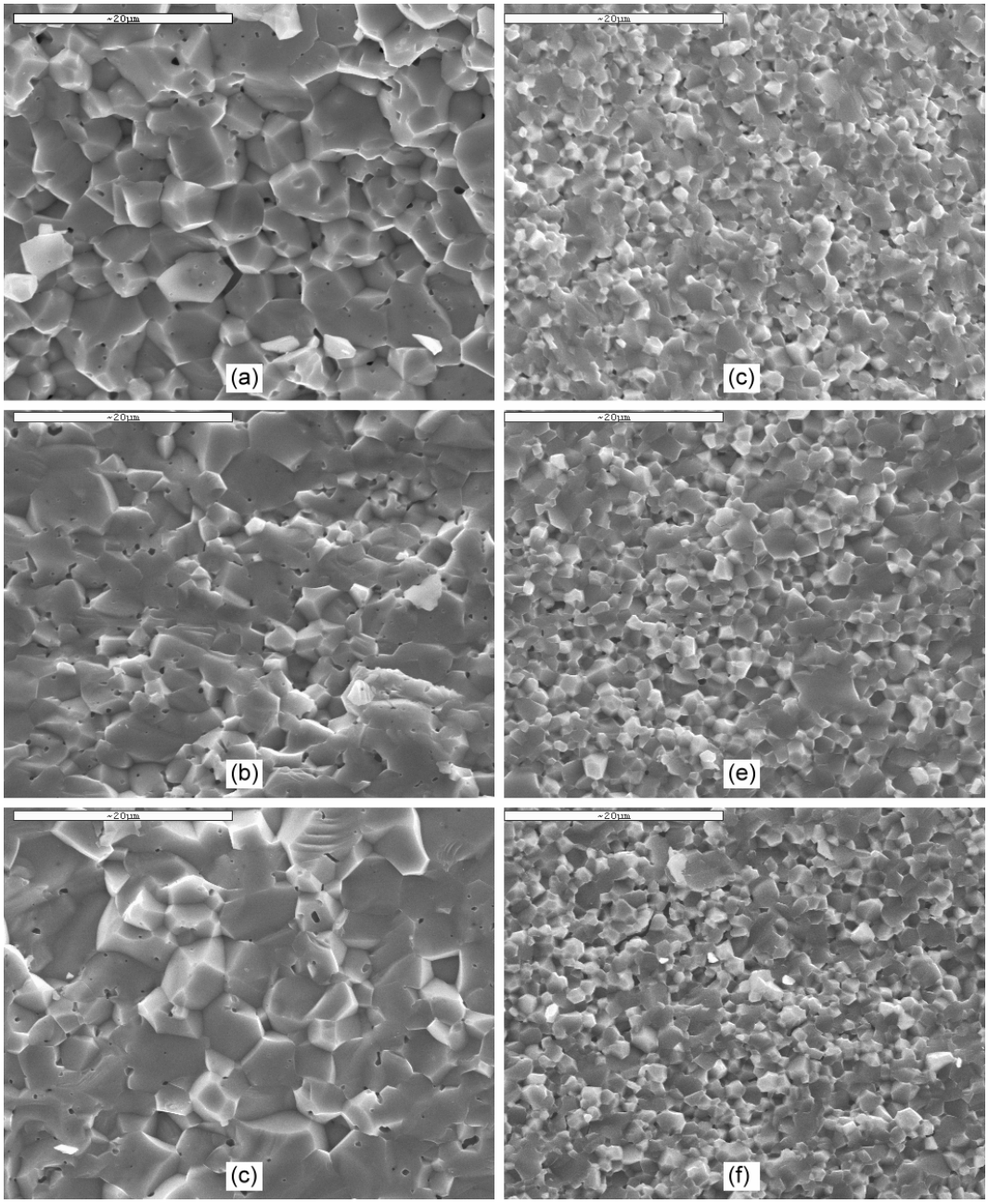


**Figure 5.2. SEM micrographs of sintered samples. (a) through (e) correspond to 0%, 0.5%, 1%, 10%, 10% (second sample), and 20% Pr. Note that the grain size of samples containing less Pr is greater than that of high Pr samples. Also note the closed porosity in samples containing low concentrations of Pr.**

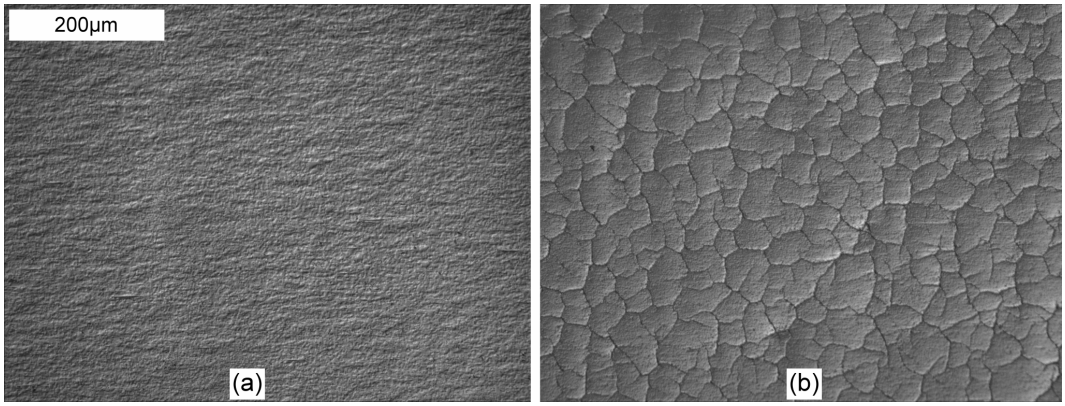


**Figure 5.3. Optical micrographs of sintered samples after collection of conductivity isotherms. Sample (a) shows no cracking in 1% PCO. Sample (b) shows extensive cracking in 10% PCO. Samples with 10% or greater Pr content cracked; samples with 1% or less Pr did not exhibit cracking.**

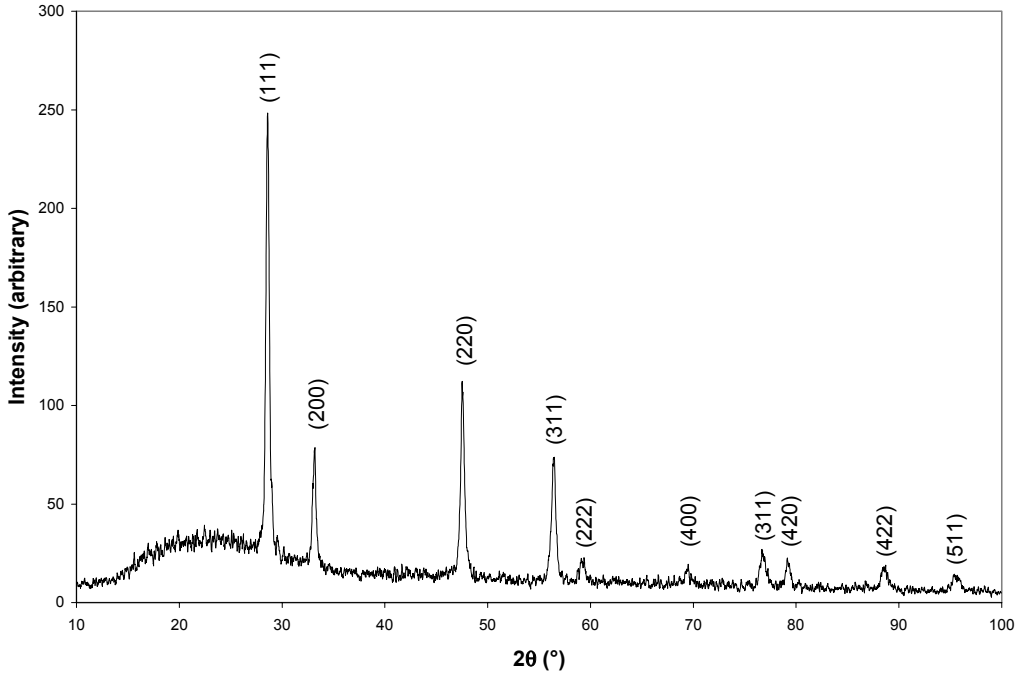


**Figure 5.4. X-ray diffraction pattern of $Pr_{0.05}Ce_{0.95}O_{2-\delta}$ powder after calcination of the oxalate precursor. Peak broadening indicates a grain size of approximately 20nm.**

X-Ray analysis of sintered samples was also performed in order to verify that the high temperatures used during sintering did not result in phase segregation of the material. Patterns were collected for each composition analyzed, and the lattice parameter of each sample was calculated based on the peak positions of all peaks in the spectrum using Jade

software.[73] See Figure 5.5 for a typical diffraction scan. The spectrum is similar to that obtained from powder samples, though no amorphous hump is present since the glass holder on which the sintered samples were mounted was not in the diffraction plane, as was the case with powder samples. Figure 5.6 shows a plot of the lattice parameter of the fluorite samples as a function of Pr content. The lattice constants were calculated from the first six peaks in the diffraction spectrum (the 111, 200, 220, 311, 222, and 400 peaks). The error bars plotted represent one standard deviation of the six values obtained for the lattice constant at each composition. Vegard's law is obeyed between 0% and 20% Pr. The change in lattice parameter is very small, making identification of mixed phases difficult (if not impossible), but the linear variation of the lattice parameter with composition is a good indication that phase purity is maintained. Note that an increase in lattice parameter with increasing Pr concentration is observed, as in the case of Shuk's work[27] and in contrast to the work of Takasu[44] and Nauer.[43]

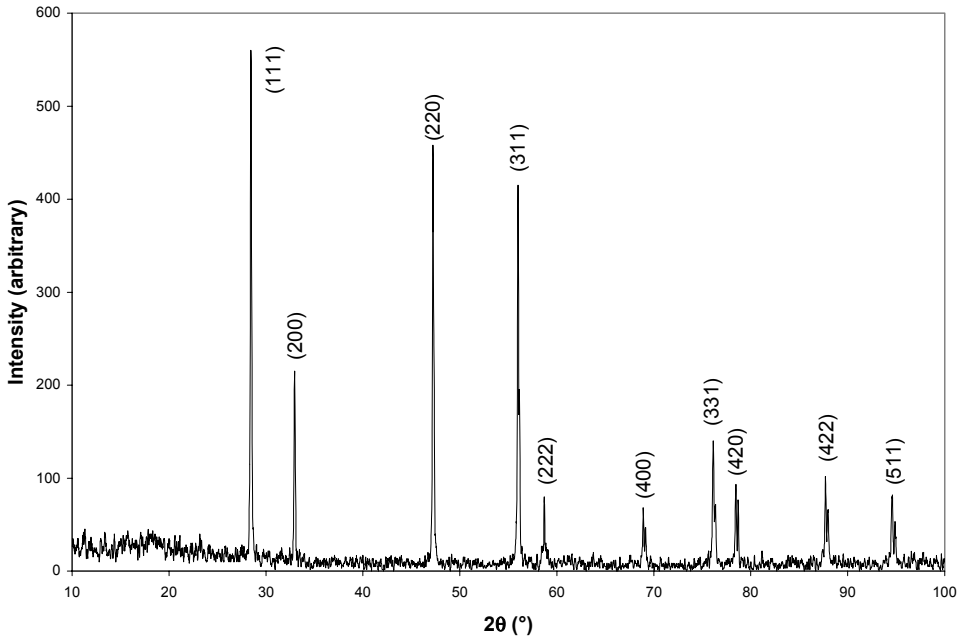


**Figure 5.5. X-ray diffraction scan of a sintered $Pr_{0.20}Ce_{0.80}O_{2-\delta}$ sample. All compositions yielded similar scans (with slight shifts in peak positions).**

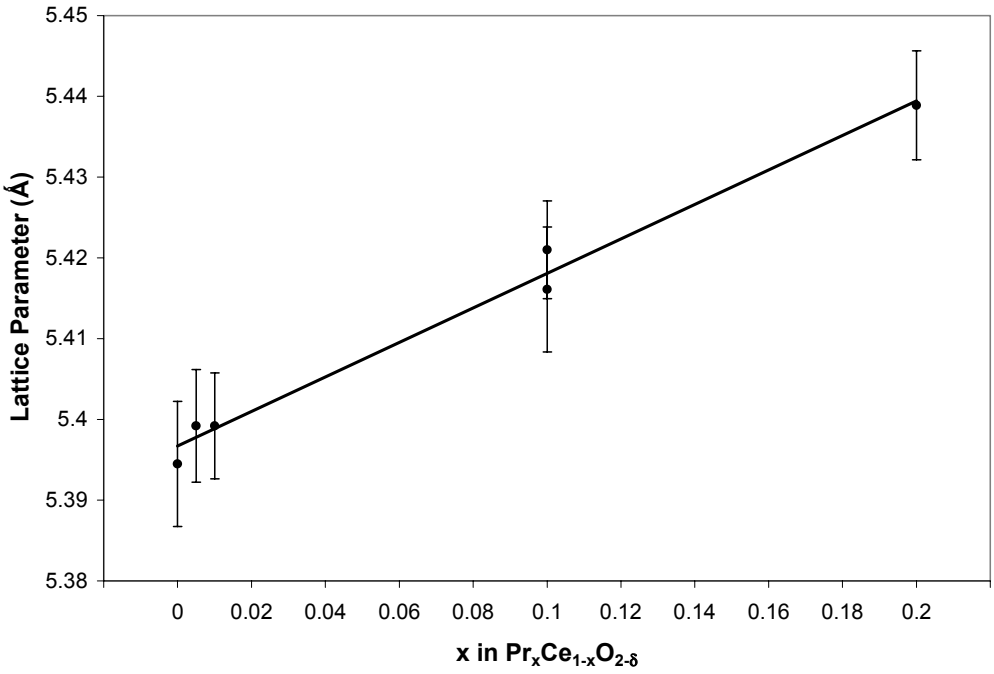


**Figure 5.6. Lattice parameter variation in PCO as a function of total Pr content. Lattice constants were calculated from the first six peaks in the diffraction scan. Error bars represent one standard deviation of those six values.**

### 5.1.5. Density Measurements

Density was measured geometrically. Parallelepiped samples were cut from sintered disks so that the volume could be determined as length x width x height. The samples used were quite small (approximately 3 mm per side). The mass of each sample was recorded, and the ratio of mass to volume was calculated. Table 5.2 shows the densities of the materials examined (after collection of conductivity isotherms). The theoretical density was calculated based on the average weight of the cations in the material and the lattice parameter as obtained from X-Ray diffraction measurements. The experimentally determined compositions were used for this calculation. The observed percent theoretical density was lower for the samples containing high percentages of Pr than those of samples with less Pr. The density of all samples was quite high (>90%).

**Table 5.2. Densities of PCO samples calculated from geometrically measured volumes. Densities were measured after collection of conductivity isotherms.**

| %Pr (batched) | Geometric Density | Lattice Constant (Å) | Theoretical Density | Percent Theoretical Density |
|---|---|---|---|---|
| 0 | 7.046 | 5.3945 | 7.283 | 96.7 |
| 0.5 | 7.006 | 5.3992 | 7.264 | 96.5 |
| 1 | 7.135 | 5.3992 | 7.264 | 98.2 |
| 10 | 7.027 | 5.4210 | 7.180 | 97.9 |
| 10 | 6.856 | 5.4161 | 7.199 | 95.2 |
| 20 | 6.513 | 5.4389 | 7.112 | 91.6 |

### 5.1.6. $pO_2$ Control

Control of oxygen pressure was performed using an oxygen pump system, as described in the experimental section. With such a system, control of $pO_2$ was possible in small increments over a wide range of $pO_2$ values, even at low temperature. Figure 5.7 shows a continuous plot of $pO_2$ as set during collection of the 600°C conductivity isotherm, along with the pump control current required to maintain the set $pO_2$. Note that control of $pO_2$ at each decade is possible. It is difficult to control $pO_2$ over a range of a few orders of magnitude ($10^{-10}$ to $10^{-7}$ in Figure 5.7), since the change in $pO_2$ per unit current in this area is very large. Nonetheless, it is possible to control $pO_2$ over the entire range of interest.

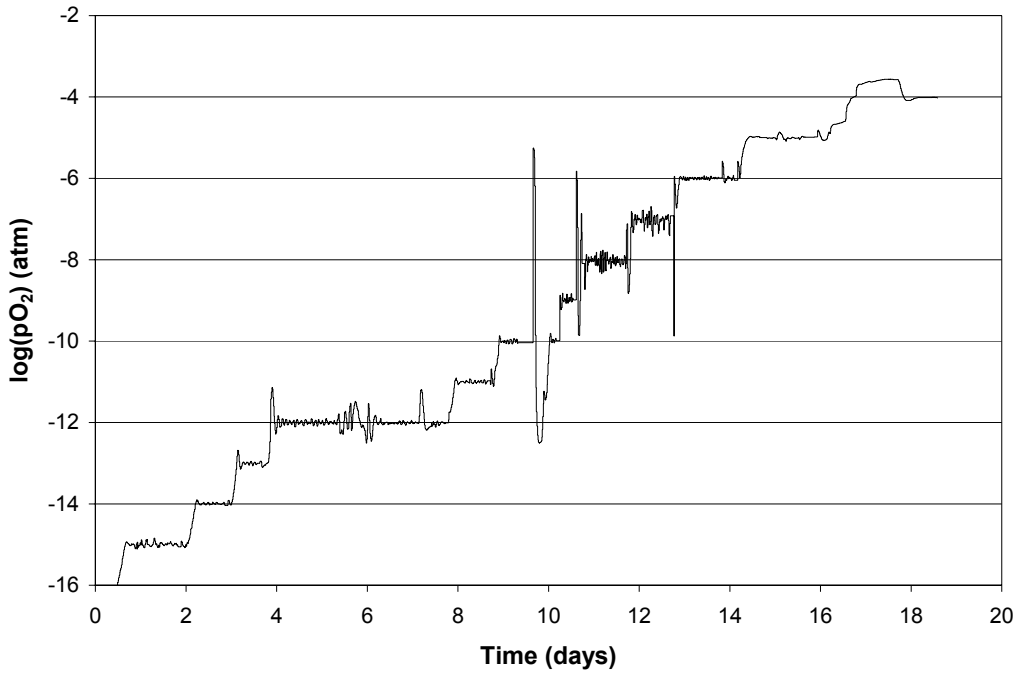


**Figure 5.7. Pump controlled oxygen partial pressure during collection of a 600°C isotherm. Note the instability of control between $10^{-7}$ and $10^{-10}$ $pO_2$.**

## *5.2. Conductivity Measurements*

### 5.2.1. DC Conductivity

Conductivity isotherms were collected at six different temperatures ranging from 600-850°C. It is relevant to compare the conductivities of a given composition at different temperatures and those of different compositions at constant temperature. Figure 5.8 through Figure 5.13 show conductivity as a function of $pO_2$ in a given material composition over a range of temperatures. Figure 5.14 through Figure 5.19 show conductivity as a function of $pO_2$ in each composition studied at the temperature indicated in each figure. The solid lines shown in each plot represent the best fits of the conductivity model described in the defect modeling section. Details of trends in the fitting parameters used to generate the best fit curves will be presented in the discussion section.

Note that all conductivity data presented follows the trends predicted by the defect model previously described. At low $pO_2$ values and high temperatures, reduction of the host cerium ions results in increased electron conductivity. At intermediate $pO_2$ values, a

plateau in ionic conductivity is observed. In compositions containing less than 5% Pr, a decreasing $pO_2$ dependent ionic conductivity is observed at high $pO_2$ values as $Pr^{3+}$ is oxidized to $Pr^{4+}$. In compositions containing higher levels of Pr, impurity band formation results in electronic hopping conductivity, which demonstrates a maximum where $[Pr_{Ce}^{/}] = [Pr_{Ce}^{x}]$.

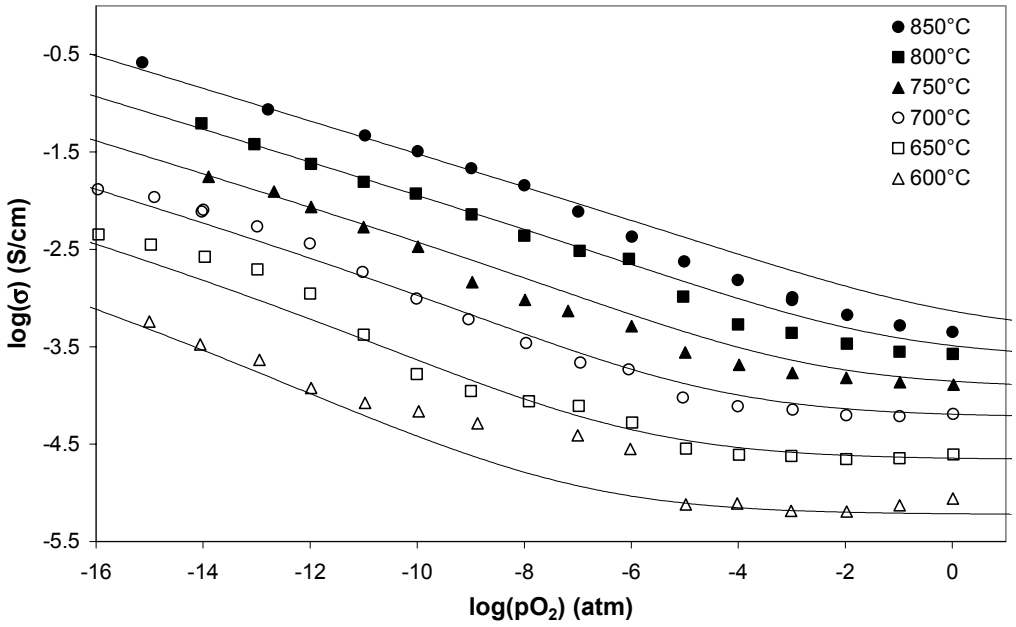


**Figure 5.8. Electrical conductivity isotherms for nominally undoped $CeO_2$ from 600-850°C.**

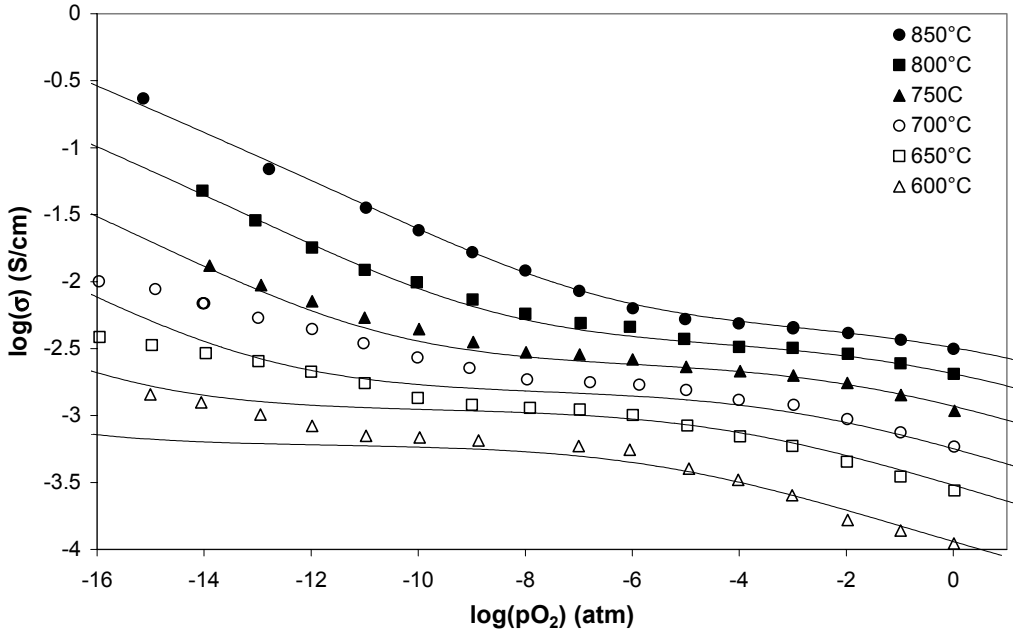


**Figure 5.9. Electrical conductivity isotherms for $Pr_{0.005}Ce_{0.995}O_{2-\delta}$ from 600-850°C.**

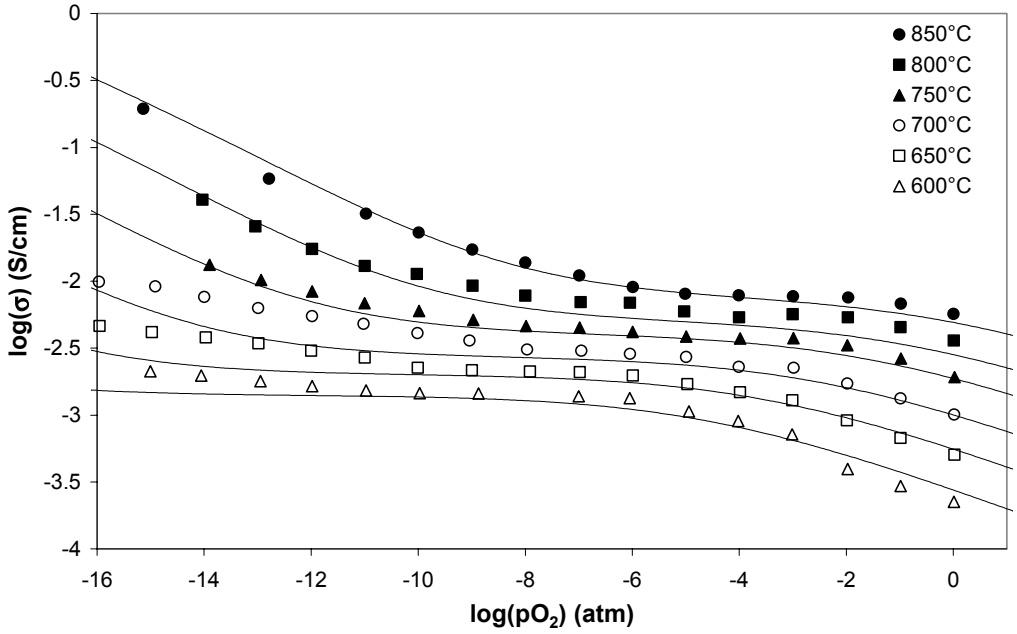


**Figure 5.10. Electrical conductivity isotherms for $Pr_{0.01}Ce_{0.99}O_{2-\delta}$ from 600-850°C.**

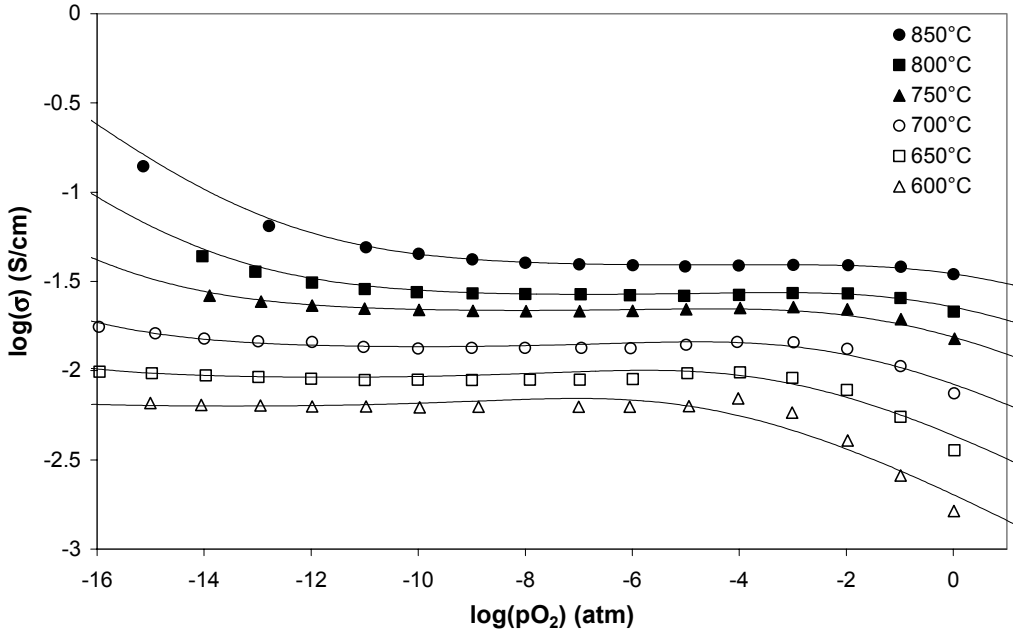


**Figure 5.11. Electrical conductivity isotherms for $Pr_{0.10}Ce0_{.90}O_{2-\delta}$ from 600-850°C.**

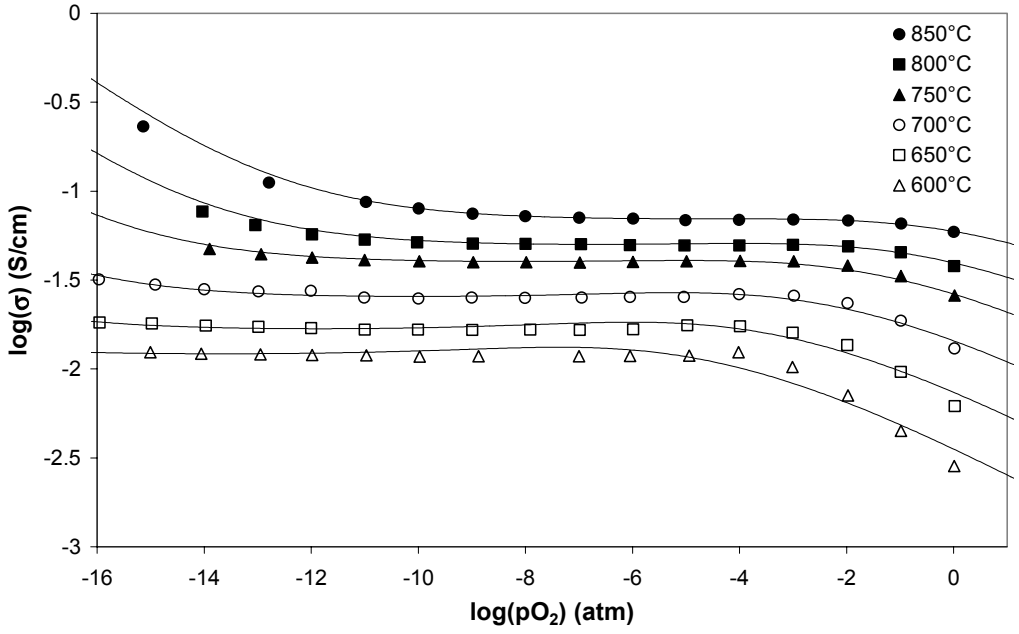


**Figure 5.12. Electrical conductivity isotherms for $Pr_{0.10}Ce_{0.90}O_{2-\delta}$ (sample b) from 600-850°C.**

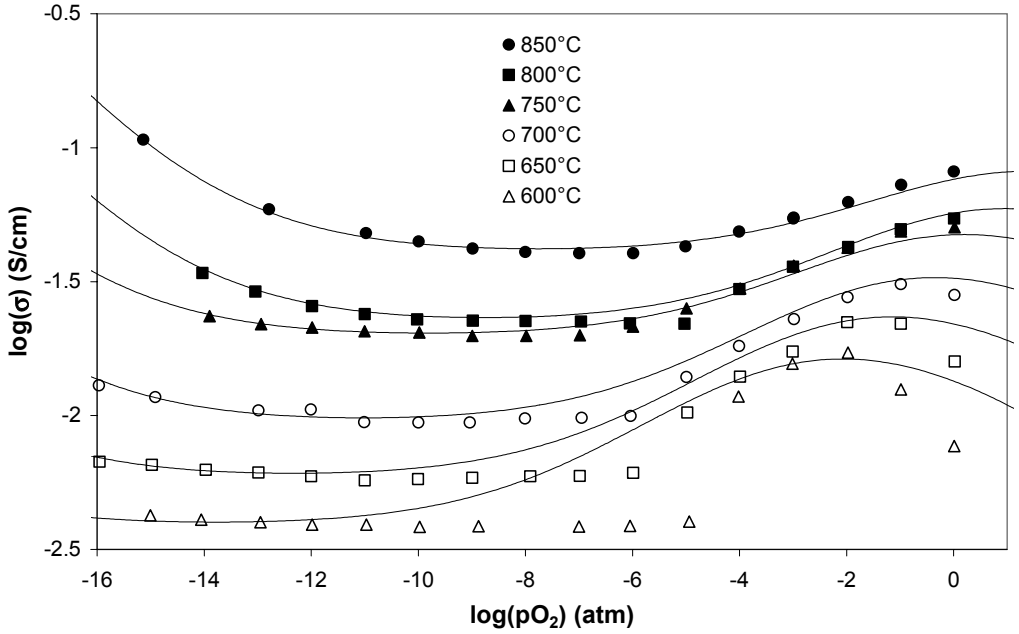


**Figure 5.13. Electrical conductivity isotherms for $Pr_{0.20}Ce_{0.80}O_{2-\delta}$ from 600-850°C.**

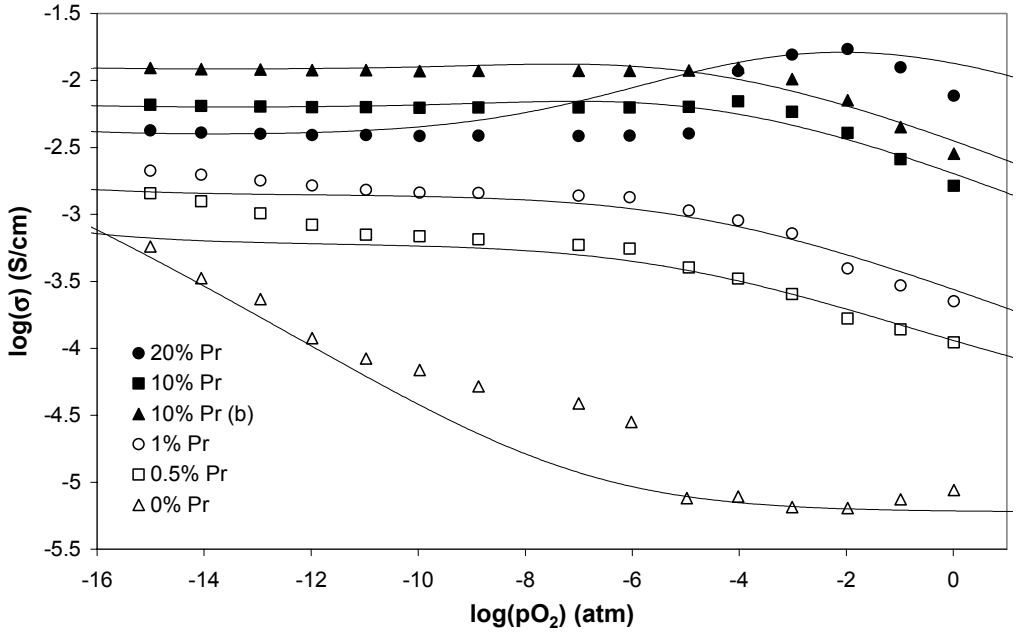


**Figure 5.14. Electrical conductivity isotherms for $Pr_xCe_{1-x}O_{2-\delta}$ at 600°C.**

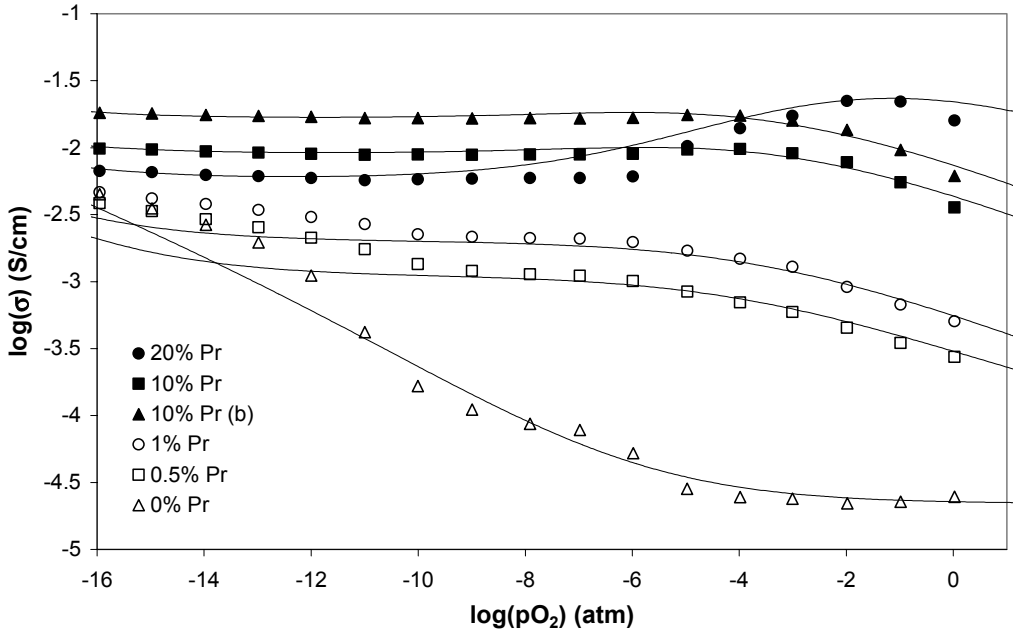


**Figure 5.15. Electrical conductivity isotherms for $Pr_xCe_{1-x}O_{2-\delta}$ at 650°C.**

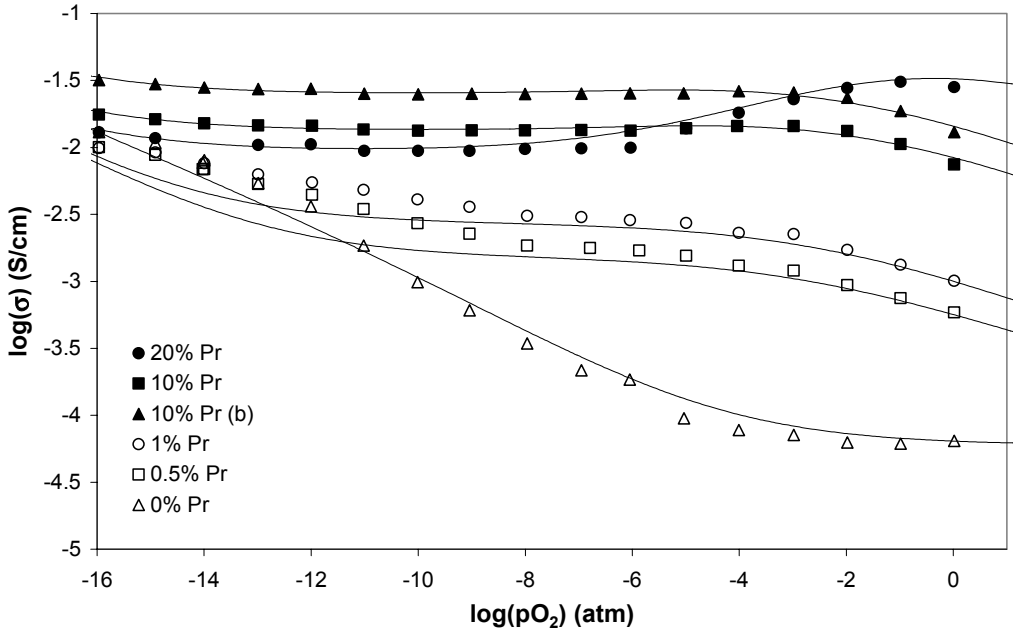


**Figure 5.16. Electrical conductivity isotherms for $Pr_xCe_{1-x}O_{2-\delta}$ at 700°C.**

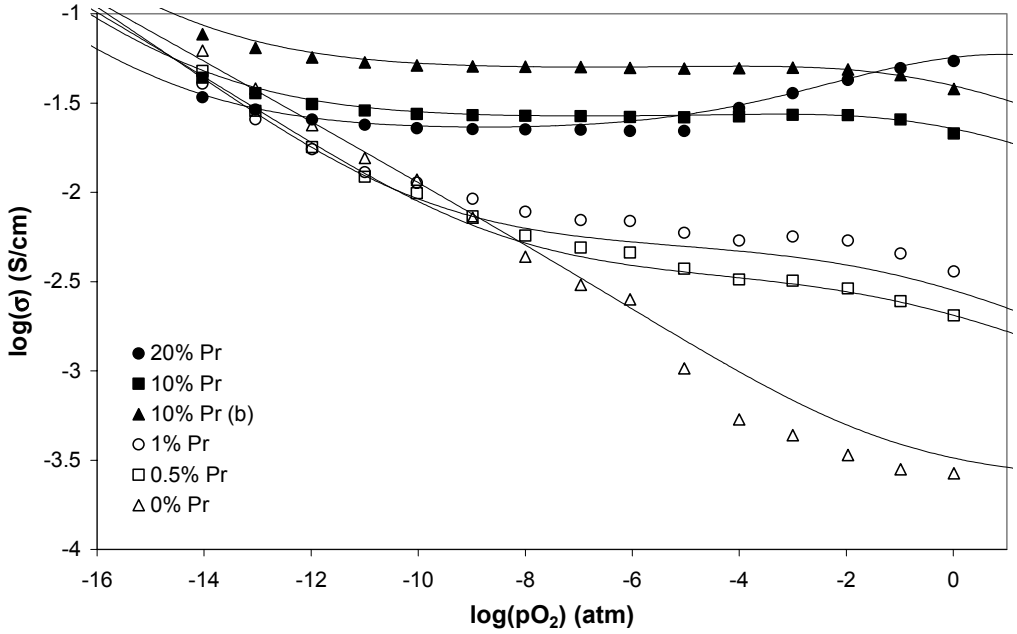


**Figure 5.17. Electrical conductivity isotherms for $Pr_xCe_{1-x}O_{2-\delta}$ at 750°C.**

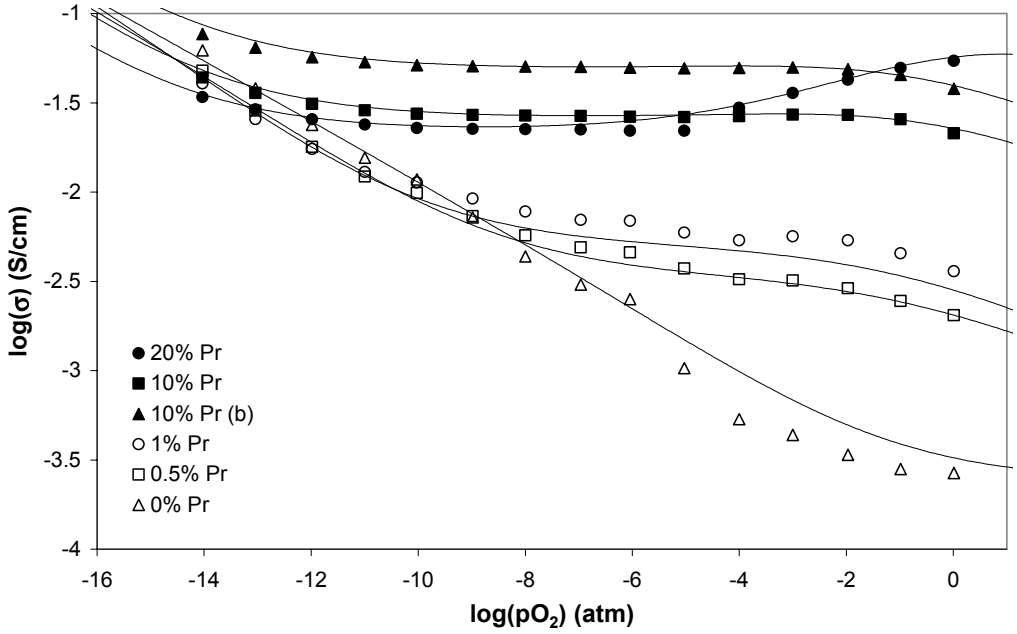


**Figure 5.18. Electrical conductivity isotherms for $Pr_xCe_{1-x}O_{2-\delta}$ at 800°C.**

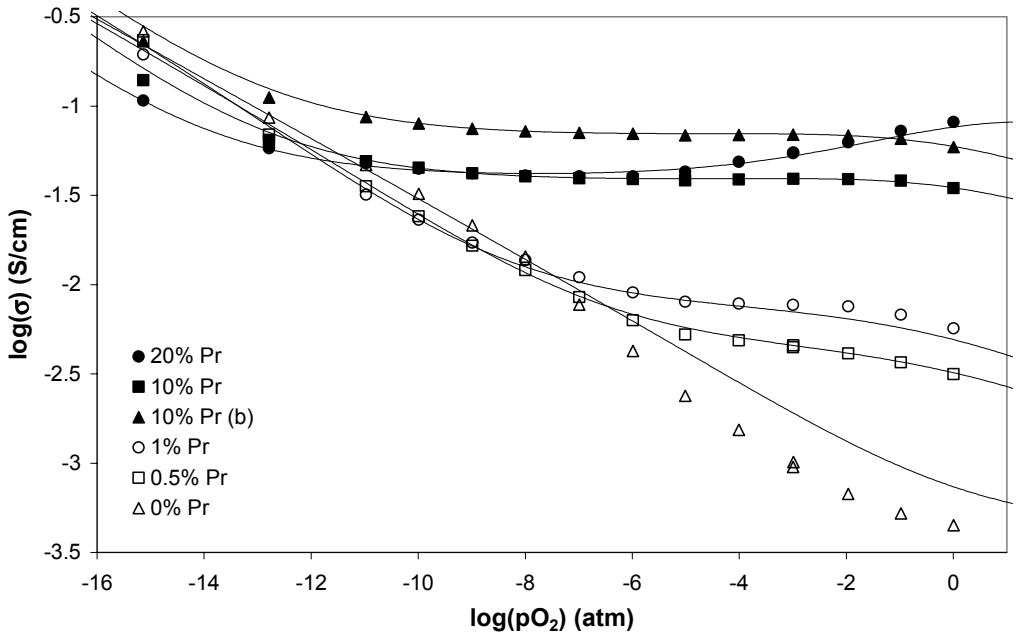


**Figure 5.19. Electrical conductivity isotherms for $Pr_xCe_{1-x}O_{2-\delta}$ at 850°C.**

In fitting the data, it was found that the limited range of Ce reduction observed at low $pO_2$, particularly for heavily doped samples at low temperatures, presented difficulties in obtaining reasonable values of the reduction constant for $CeO_2$ ($K_R$) and mobility of electron ($\mu_e$) in the system. Since the conductivity showed only a slight upturn representative of cerium reduction, fitting of the two parameters yielded very noisy, often non-physical results. In order to more accurately determine these constants (on which much of the rest of the conductivity fitting hinged), measurements at higher temperature and lower $pO_2$ were performed. The results of fitting at high temperatures were then extrapolated to lower temperatures for use in fitting total conductivity isotherms at the temperature range of interest. Figure 5.20 through Figure 5.25 show conductivity in each sample composition at low $pO_2$ and high temperatures (800-1000°C). Solid lines represent the best fits to the data, as obtained by varying only the cerium reduction constant ($K_R$). See the discussion section for further details.

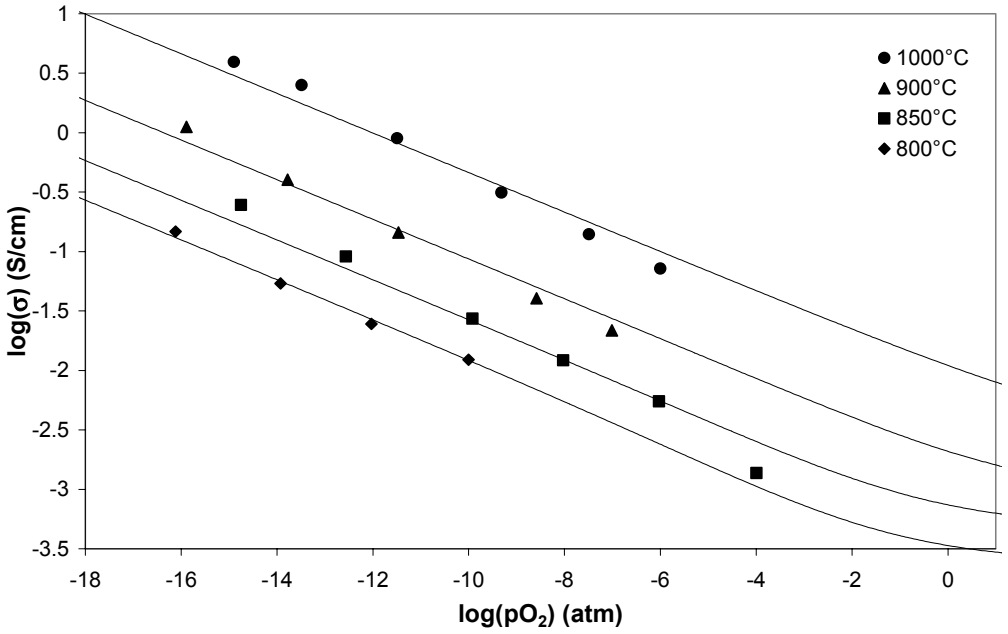


**Figure 5.20. Electrical conductivity isotherms for nominally undoped $CeO_2$ from 800-1000°C.**

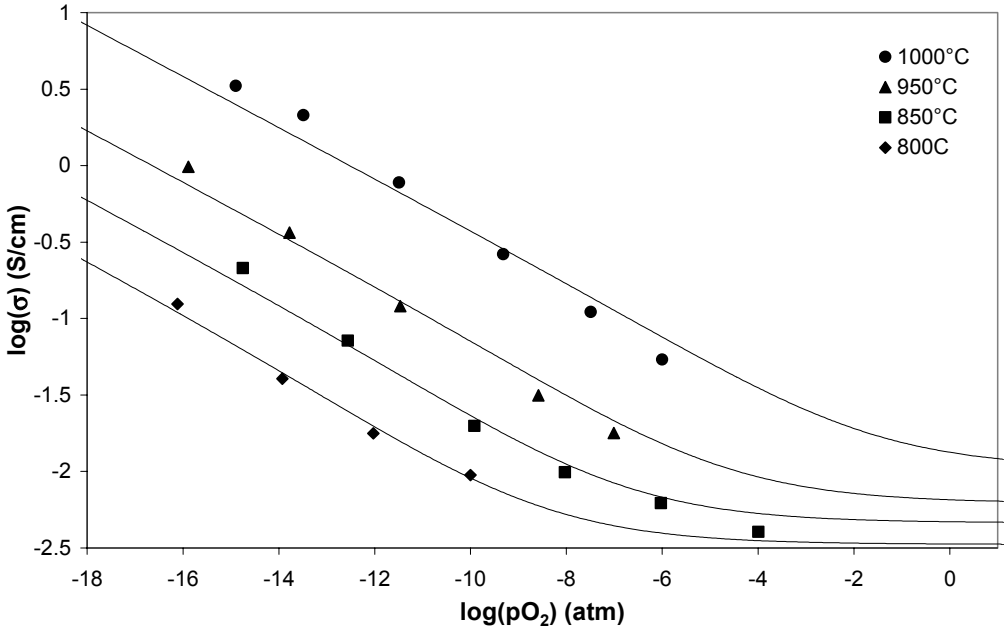


**Figure 5.21. Electrical conductivity isotherms for $Pr_{0.005}Ce_{0.995}O_{2-\delta}$ from 800-1000°C.**

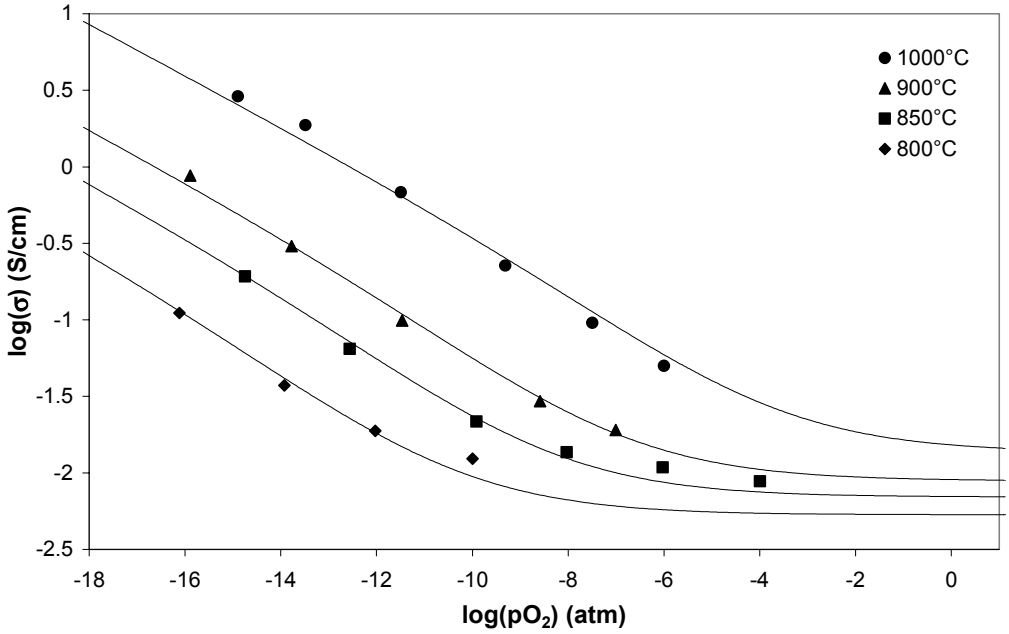


**Figure 5.22. Electrical conductivity isotherms for $Pr_{0.01}Ce_{0.99}O_{2-\delta}$ from 800-1000°C.**

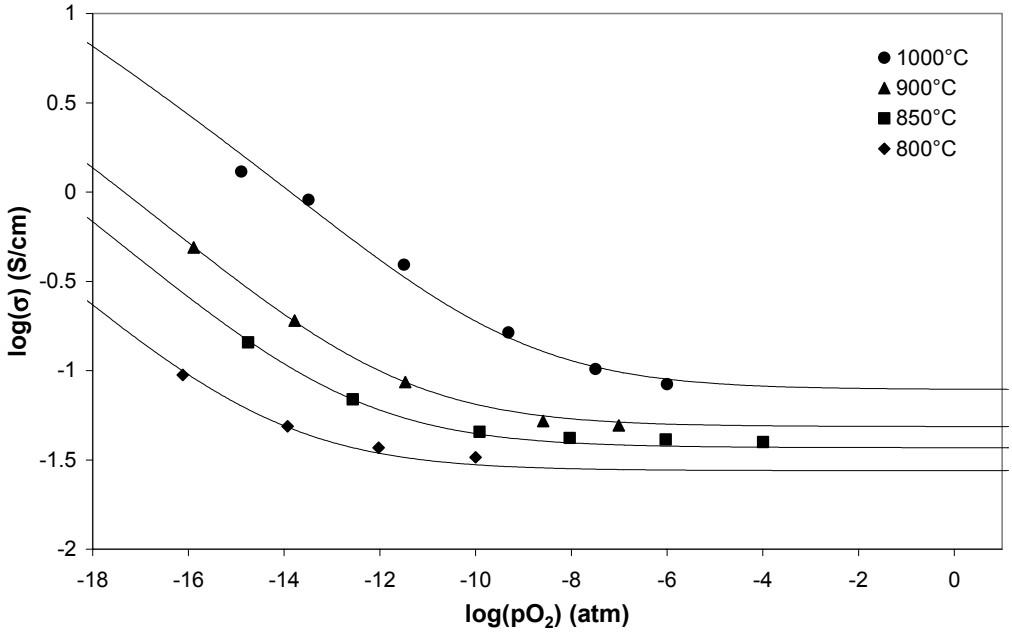


**Figure 5.23. Electrical conductivity isotherms for $Pr_{0.10}Ce_{0.90}O_{2-\delta}$ from 800-1000°C.**

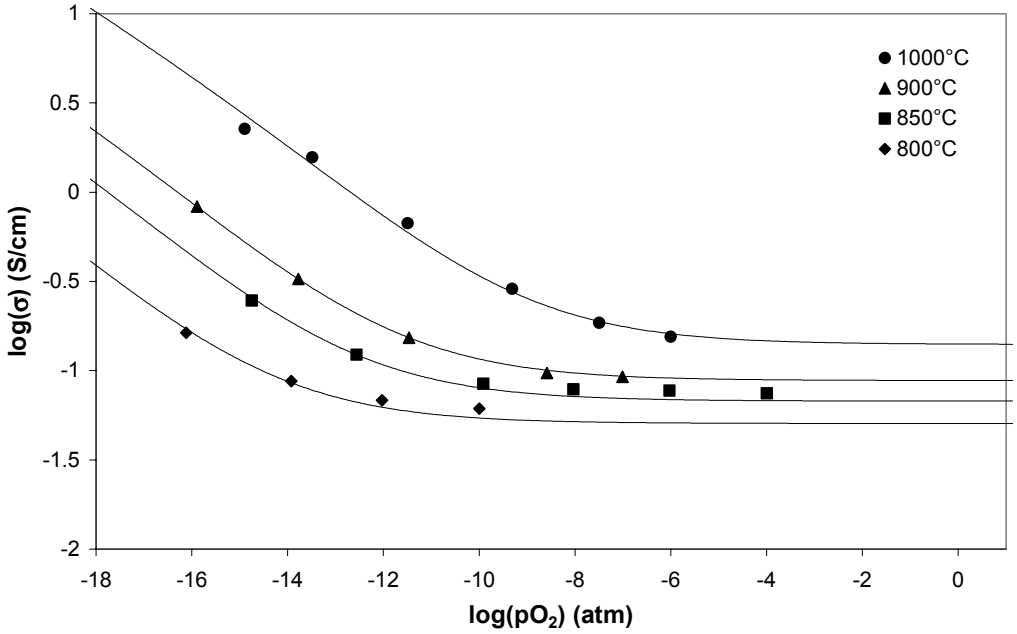


**Figure 5.24. Electrical conductivity isotherms for $Pr_{0.10}Ce_{0.90}O_{2-\delta}$ from 800-1000°C (sample b).**

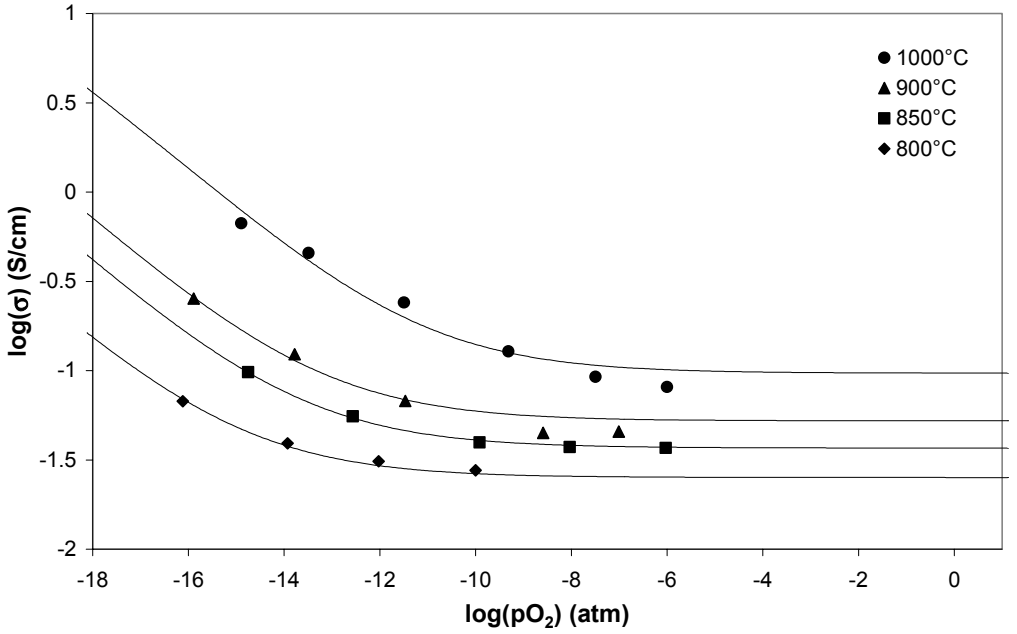


**Figure 5.25. Electrical conductivity isotherms for $Pr_{0.20}Ce_{0.80}O_{2-\delta}$ from 800-1000°C.**

### 5.2.2. AC Impedance

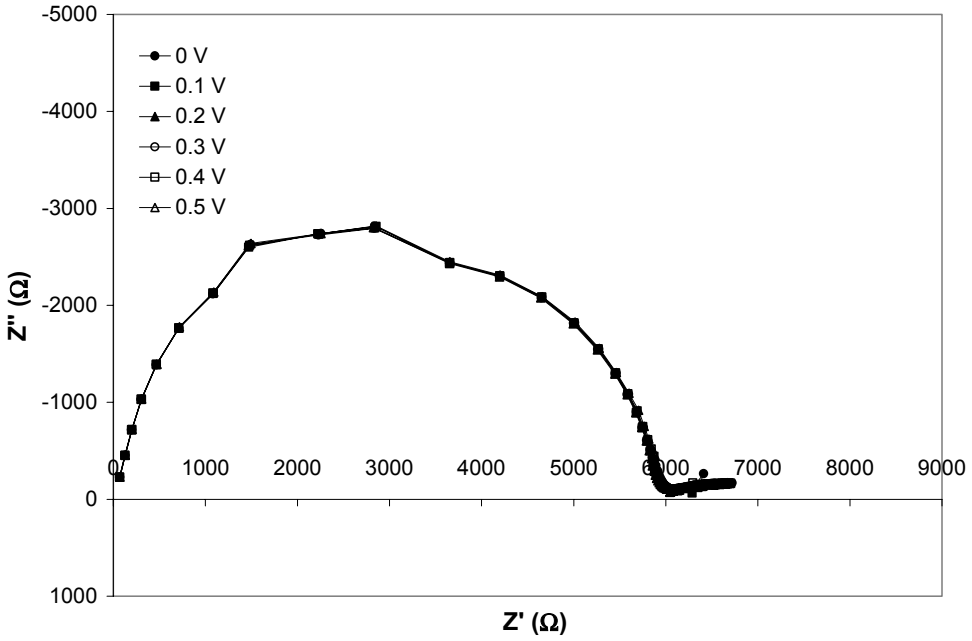


**Figure 5.26. AC Impedance spectrum of $Pr_{0.01}Ce_{0.99}O_{2-\delta}$ at 700°C and $10^{-1}$ atm $pO_2$ at applied DC bias ranging from 0-0.5V. Z' is the real component of the impedance; Z'' is the imaginary component. No bias effect is observed (all biases overlap). The apparent discontinuities at approximately 1500 and 3500 ohms are reproducible machine errors (a ranging issue on the impedance analyzer used to collect the data).**

AC impedance scans were collected at a limited number of temperatures and oxygen partial pressures in order to verify that the DC values collected over a wide range of conditions represented the bulk conductivity of the sample. Figure 5.26 shows the AC impedance spectra of the $Pr_{0.01}Ce_{0.99}O_{2-\delta}$ sample at 700°C and $10^{-1}$ atm $pO_2$ as a function of the DC bias applied during the measurement. In this case, two impedance arcs were observed. Neither arc exhibited a significant bias dependence. The lower frequency arc (at low Z' values) was attributed to the bulk resistance of the ceramic sample, while the higher frequency arc (Z' > 6000 Ω) was attributed to a grain boundary effect. Figure 5.26 is representative of the general behavior observed in the $Pr_{0.005}Ce_{0.995}O_{2-\delta}$ and $CeO_2$ samples as well. Figure 5.27 shows the AC impedance of the $Pr_{0.20}Ce_{0.80}O_{2-\delta}$ sample under the same conditions as shown in Figure 5.26. Here, the total resistance of the sample is low and the effects of a high contact resistance in the 2-point AC measurement

mask the response of the sample itself. Note that the measured resistance varies with applied bias, indicative of a contact resistance measurement. Comparisons of DC and AC conductivity measurements will be presented in the discussion section.

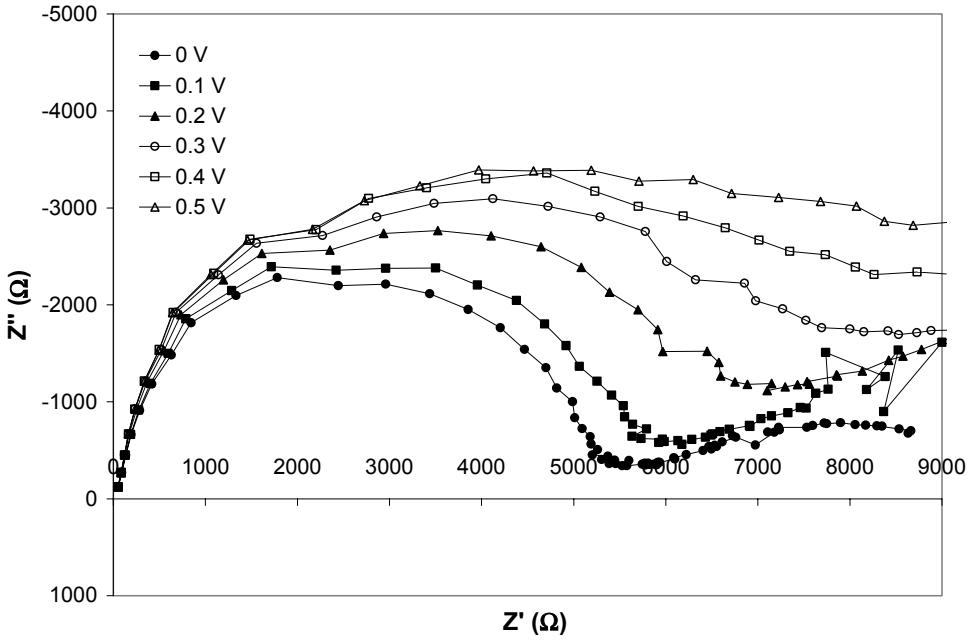


**Figure 5.27. AC impedance spectrum of $Pr_{0.20}Ce_{0.80}O_{2-\delta}$ at 700°C and $10^{-1}$ atm $pO_2$ at applied DC bias ranging from 0-0.5V. Note the bias dependence of the response.**

## *5.3. Coulometric Titration Measurements*

During a coulometric titration experiment, the amount of oxygen removed from the sample cell and the resulting $pO_2$ are measured. This allows the total change in nonstoichiometry to be plotted as a function of $pO_2$ for a given temperature. It is important to note, however, that the data plotted is in fact a change in nonstoichiometry, not the absolute nonstoichiometry of the material being studied (unless the starting state of the material happens to find it exactly at stoichiometry). In the case of PCO, there is a given oxygen deficiency at 0.21atm $pO_2$ where the sample is equilibrated prior to titration. As a result, the changes in nonstoichiometry plotted in the raw coulometric titration data are not representative of the total nonstoichiometry of PCO. Further analysis of the raw data is required in order to determine the initial nonstoichiometry prior to meaningful interpretation of the data. Such analysis will be presented in the discussion section.

Figure 5.28 through Figure 5.30 show the raw changes in oxygen stoichiometry in 1%, 5%, and 20% PCO, the only compositions examined during this study. The dotted lines in the plots represent the theoretical maximum nonstoichiometry one would expect if the defect mechanism presented (reduction of $Pr^{4+}$ to $Pr^{3+}$ accompanied by the creation of doubly-charged oxygen vacancies) is the only mechanism by which oxygen leaves the material. The data themselves show no obvious trends as a function of temperature in their raw form. In Figure 5.30 it is evident that data collected at temperatures lower than 600°C are qualitatively different than those collected at higher temperatures. The low temperature data produces linear regions of stoichiometry variation on a log(x) vs. log($pO_2$) scale, whereas higher temperatures yield smoothly varying, asymptotic variation of nonstoichiometry with $pO_2$. Possible explanations for this difference will be presented in the discussion section. Also note that the total nonstoichiometry of the 1% sample exceeds that predicted by the model. It is possible that there was a leak in the 1% cell which contributed to this apparent discrepancy. Again, see the discussion section for possible explanations.

Figure 5.31 shows the raw change in stoichiometry for all three compositions examined at 600°C. Horizontal lines indicate the maximum nonstoichiometry predicted by the defect model for each composition. The total nonstoichiometry change as a function of $pO_2$ is expected, that is, higher overall changes in nonstoichiometry for samples containing more praseodymium. It also appears that the initial abrupt increase in measured nonstoichiometry upon reduction from 0.21atm $pO_2$ is faster for samples containing less Pr.

In order to see any meaningful trends in the titration data or to extract any useful parameters from the curves, fitting of the initial nonstoichiometry is required. The results of such fitting will be examined in the discussion section.

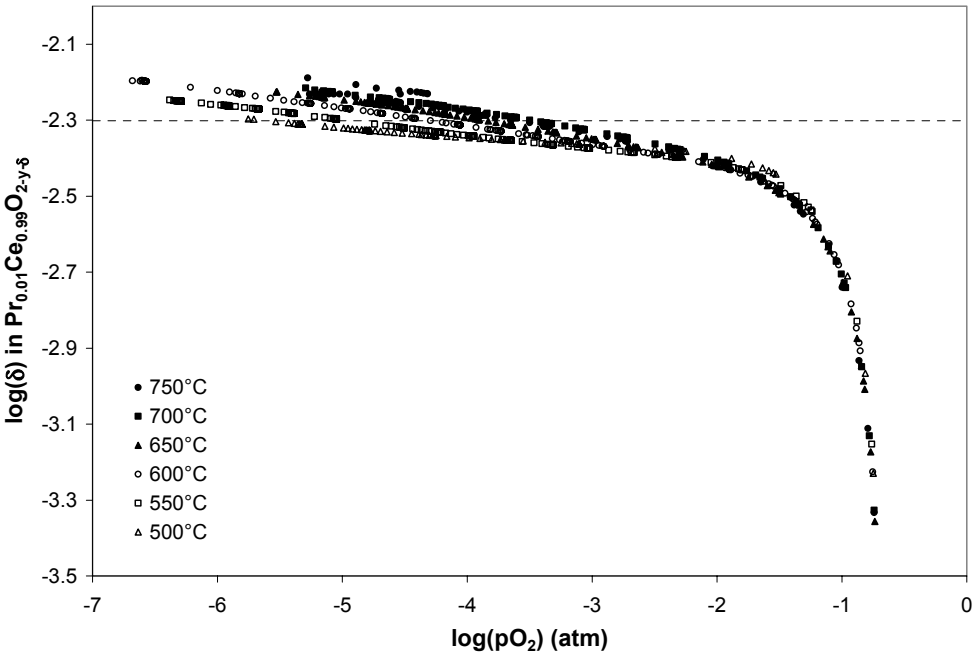


**Figure 5.28. Change in nonstoichiometry (δ) during coulometric titration of $Pr_{0.01}Ce_{0.99}O_{2-y-\delta}$ from 500-750°C. The dotted line represents maximum nonstoichiometry predicted by the defect model presented.**

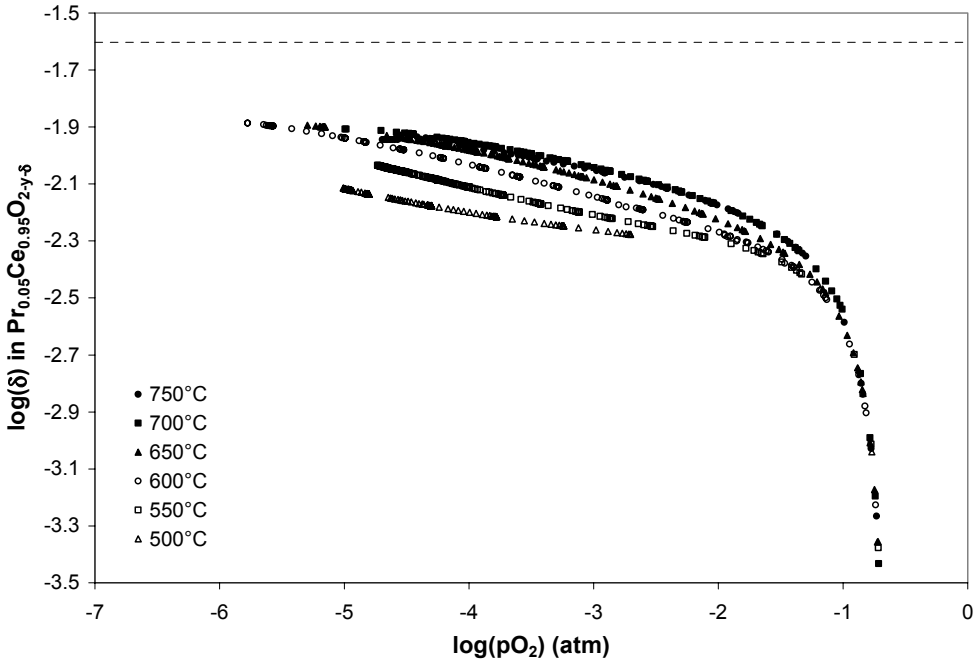


**Figure 5.29. Change in nonstoichiometry (δ) during coulometric titration of $Pr_{0.05}Ce_{0.95}O_{2-y-\delta}$ from 500-750°C. The dotted line represents maximum nonstoichiometry predicted by the defect model presented.**

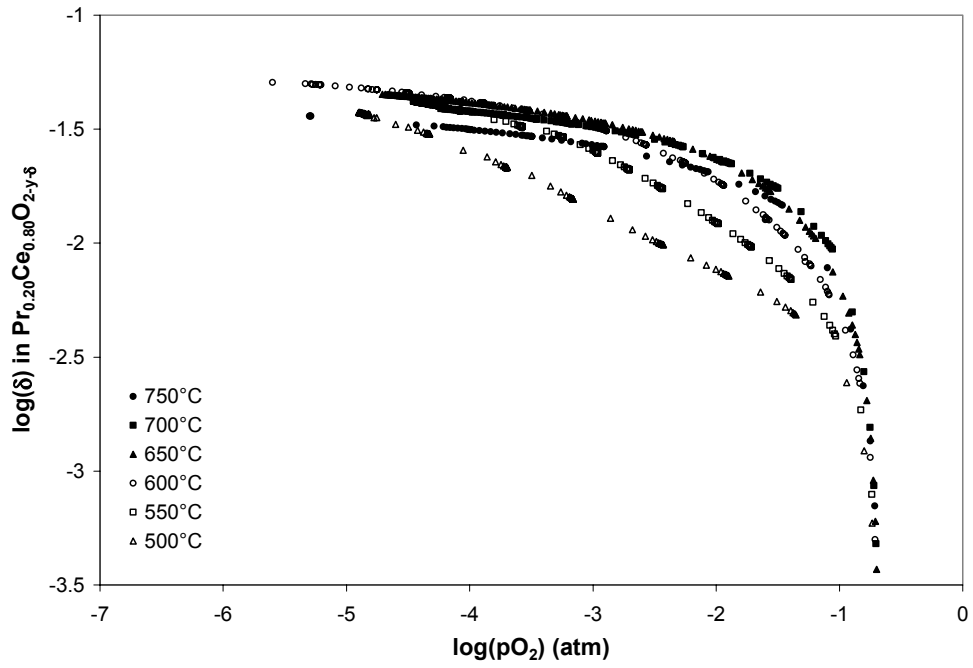


**Figure 5.30. Change in nonstoichiometry (δ) during coulometric titration of $Pr_{0.20}Ce_{0.80}O_{2-y-\delta}$ from 500-750°C. The maximum nonstoichiometry predicted by the defect model presented is 0.1, the upper limit of the y axis.**

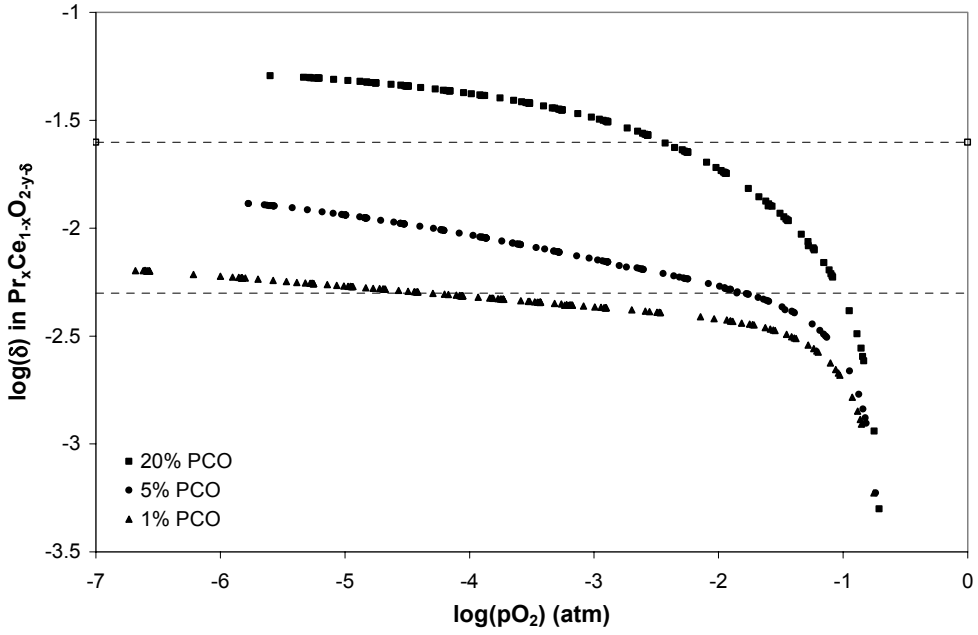


**Figure 5.31. Change in nonstoichiometry (δ) during coulometric titration of $Pr_xCe_{1-x}O_{2-\delta}$ at 600°C. Dotted lines represent the maximum nonstoichiometry predicted by the defect model presented for each composition.**

## *5.4. Thermoelectric Power*

Examination of the thermoelectric power revealed that the data collected were not of sufficient quality to extract meaningful parameters. The Seebeck coefficient is the slope of the $\Delta V$ vs. $\Delta T$ curve that results when a thermal gradient is applied to a sample. In many cases, the response measured was not at all linear, making determination of the slope impossible. In addition, the $\Delta V$ vs. $\Delta T$ curve should pass through the origin. Oftentimes the intercept of the data collected was very large relative to the estimated Seebeck coefficient (for example, the slope of the $\Delta V$ vs. $\Delta T$ curve might be 400 $\mu V/K$ with an intercept of 20mV). While some qualitative trends appeared to be valid, the overall quality of the data was insufficient to warrant full analysis.

# Chapter 6. Discussion

## *6.1. Physical Characterization*

### 6.1.1. Particle Size

The powder particle size observed in the SEM micrographs shown in Figure 5.1 and the crystallite size determined by X-ray peak broadening measurements are orders of magnitude apart (approximately 1 μm in the SEM images, 20nm by peak broadening). Agglomeration of the powder during precipitation explains this difference. The oxalate powder precipitated as polycrystalline particles. Calcining at 700°C was sufficient to decompose the organic material in the oxalate precursor, but insufficient to yield significant grain growth. The resulting oxide powders consists of hard agglomerates of approximately 0.5-1 μm diameter, made up of crystallites of approximately 20nm.

The micrographs of sintered specimens in Figure 5.2 show that more grain growth occurred in samples containing 1% or less Pr than in those with higher Pr content. The amount of grain boundary drag presented by 1% Pr was not significant enough to alter the sintering behavior of the material. At 10% Pr, however, grain boundary motion is slowed such that the grain size of the resulting sample is significantly smaller than that of the samples containing less Pr. This phenomenon is generally attributed to solute segregation and grain boundary drag. It is possible that some degree of Pr segregation does occur at the grain boundaries during sintering, though a continuous variation of grain size with increasing Pr content would be expected. If grain boundary segregation does occur, it is not expected that additions of 1% Pr would have no effect on the final grain size. X-ray diffraction did not detect significant amounts of second phase present, however, it is possible that a small quantity of grain boundary phase exists, perhaps as an enriched Pr-region with lattice constant similar to that of the bulk composition.

### 6.1.2. X-Ray Diffraction

The diffraction scans used to determine lattice parameters and phase purity were collected from sintered specimens using no internal standard. As a result, the accuracy of the peak positions cannot be verified. All scans were collected on successive diffraction

scans using the same instrument and same sample mount, however, so it is likely that the variation of peak position from one scan to the next is consistent.

The lattice parameters shown in Figure 5.6 are an average value of the lattice parameter calculated from the positions of six diffraction peaks. The standard deviation of that average value is shown on the error bars. Within the experimental error, there is a linear dependence of lattice parameter on the Pr content of the material. This linear relationship is a good indicator that the materials in question are phase pure. If there were multiple phases present, a discontinuity in the variation of lattice parameter with composition would be expected at the phase boundary. At high Pr contents, a second fluorite phase is expected to form. There is no evidence of such phase separation in the diffraction data, however. There is an observed increase in lattice parameter with increasing Pr content. According to Shuk,[27] this indicates a high concentration of $Pr^{3+}$ in the samples. Diffraction scans were collected after electrical characterization. The last isotherms collected prior to X-ray analysis were those at high temperature and $pO_2$, which would have resulted in a high $Pr^{3+}$ composition. Presumably the processing techniques used by Takasu[44] and Nauer[43] resulted in a higher concentration of $Pr^{4+}$, yielding lattice parameter variations in contrast with the work of Shuk[27] and or this study.

### 6.1.3. Compositional Analysis

Batches of 10 and 20% Pr yielded final materials within 5% of the target value. These materials were batched using stock solutions that had been calibrated using the mass calibration technique shown in Figure 3.1. Lower percentages, however, were batched using calibrations obtained through the colorimetric titration calibration procedure. In addition, the low quantities of Pr stock solution required for the 0.5% and 1% Pr batches amplified any measurement errors. For instance, if 0.5 mL stock solution was required for a 0.5% Pr batch, an error of 0.05 mL represents a 10% error in batch composition, whereas the same measurement error would represent only a 1% error in a batch targeted for 5% Pr. The combination of the lower accuracy of the stock solution calibration and the low quantities of $Pr(NO_3)_3$ solution required for 0.5% and 1% Pr batches yielded significantly higher error in the resulting oxide powder.

### 6.1.4. Sample Cracking

The optical micrographs shown in Figure 5.3 exhibit extensive cracking in samples containing high percentages of Pr. Compositions containing less than 1% Pr do not appear to exhibit the same mechanical instability. It is known that pure ceria dilates upon reducing.[95] This dilation produces stresses which can result in cracking of the material. The same mechanism is likely active in PCO. As Pr reduces from $Pr^{4+}$ to $Pr^{3+}$, the structure dilates and the resulting stress cracks the sample. A highly porous microstructure might alleviate this stress and allow the material to be cycled through oxidation/reduction without cracking. It is unlikely, however, that PCO containing 10% or more Pr can be used in applications requiring dense, monolithic structures.

For the purposes of these experiments, this cracking can be expected to alter the conductivity isotherms collected. The isotherms presented can only be interpreted as lower bounds for conductivity in the material. An examination of the overall quality of the conductivity data will be presented below.

As noted in the experimental section, pellets were fired under a mechanical vacuum (approximately $10^{-2}$ Torr) in order to avoid pellet cracking during sintering. This corresponds to approximately $10^{-5}$ atmospheres. Note that in Figure 5.14 through Figure 5.19, most of the Pr reduction behavior occurs at $pO_2$ values higher than $10^{-5}$ atm. The mechanical pump provided sufficient reduction to prevent Pr from oxidizing upon cooling. During the sintering ramp, most of the Pr reduced to $Pr^{3+}$. Sintering occurred at high temperature, then during the cooling ramp, the Pr was prevented from significantly re-oxidizing. Avoiding this re-oxidation (and the stresses it generated) allowed samples to be sintered without cracking. It is likely that cracking occurred upon exposure to cycles of reducing and oxidizing conditions during collection of electrical conductivity isotherms.

### 6.1.5. Density

The primary source of error in density measurements is flaws in the geometry of the samples used. Small cube-like samples, approximately 3mm per side were used. If the faces of the samples were not perfectly parallel, any imperfections such as chips were

present, or the sample was cracked, then the volume measured would be erroneous. These errors would all result in the volume measured being higher than the true volume. As a result, the densities presented are most likely lower than the true density of the samples if any such errors existed.

It should be noted that the cracking observed in the 10 and 20% Pr samples almost certainly resulted in a lower volume measurement than the true volume of the specimens. Trapped porosity observed in samples containing lower amounts of Pr (see Figure 5.2) decreased their density values.

### 6.1.6. $pO_2$ Control

As shown in Figure 5.7, it is possible to control $pO_2$ across a wide range of values at relatively low temperatures using an electrochemical oxygen pump. As noted, it is still difficult to control values in some $pO_2$ range, however, this range is much narrower than that presented by buffer gas mixture systems. According to Figure 3.5, more than 10 orders of magnitude of $pO_2$ are inaccessible at 600°C using buffer gasses alone, whereas using the oxygen pump, no pressure is completely inaccessible and only 4 orders of magnitude are difficult to control. It should be noted, however, that the instability of control observed makes measurements of systems in which equilibration times are long rather difficult. $pO_2$ control may be lost prior to equilibration of the sample. Using a system with a smaller total volume would likely alleviate this problem to some degree. The sample furnace used in this experiment was large so that many samples could be studied simultaneously. A four foot long, two inch diameter furnace tube held the samples. If a smaller furnace were used, $pO_2$ control would likely be quicker and more responsive to deviations from the target value. In addition, the sensitivity of the system to small variations in temperature presents challenges for thermoelectric power measurements. When a heat pulse is applied, the oxygen pressure changes with the applied pulse. Despite the difficulties associated with the oxygen pump system, the ability to achieve the desired $pO_2$ values at low temperatures makes in an invaluable tool for characterization of conductive oxides at relatively low temperatures (600-800°C).

## *6.2. Electrical Conductivity*

### 6.2.1. Sources of Error in DC Measurements

There are a number of sources of error in the conductivity data deserving of mention. The cracking of the high Pr content samples was already discussed briefly. As a result of this cracking, the values measured are certainly lower than the true conductivity of the samples. Two samples of 10% Pr were analyzed. As observed in Figure 5.14 through Figure 5.19, the isotherms for the two different samples are qualitatively identical with a constant offset for the entire range of $pO_2$ values. The difference between these two isotherms can be taken as the minimum error introduced by the sample cracking. At 750°C, the offset is approximately 0.25 on the log(σ) scale. A constant error of 0.3 on the log(σ) scale was added to the total estimated error in conductivity to account for cracking. It is possible (and likely) that the error is in fact higher, given that both 10% samples were extensively cracked and the actual conductivity of un-cracked 10% PCO is likely higher than either value obtained. The error will always result in an erroneously low conductivity, so in defining error bars for the data, this factor was only added to the measured conductivity.

In addition to cracking, errors may arise due to inaccuracies in the measurement of the spacing of the electrodes on the sample, deviations from the target temperature, and deviations from the target $pO_2$ values. The electrode spacing was measured using a hand caliper. The accuracy of this measurement is estimated to be approximately 0.02 cm out of an average electrode spacing of 0.30 cm (the spacing between electrode 3 and 4 in Figure 3.2), resulting in an error of approximately 7% which was added to the total error bar calculation.

Errors in $pO_2$ vary in their importance depending on where they occur in the isotherm. For instance, an error under highly reducing conditions would result in a significant change in total conductivity since the electronic conductivity follows a strong $pO_2$ dependence in that region of the isotherm. In contrast, a deviation of a full order of magnitude in $pO_2$ would make little or no difference in the ionic plateau region in the center of the isotherm. In order to take these errors into account, a maximum $pO_2$

deviation of a factor of 2 was assumed, and the corresponding conductivity errors were calculated and added to the total estimated error.

The effect of temperature variations on the conductivity data also vary as a function of $pO_2$. The electronic conductivity (dominant at low $pO_2$ values) does not exhibit the same temperature dependence as the ionic conductivity (dominant at intermediate $pO_2$ values) or the impurity band conductivity (which dominates at high $pO_2$ values, if present). The measurement temperature for each sample was recorded on a regular basis throughout these studies. The standard deviation of the temperature was approximately 2-3 degrees. Taking a worst-case scenario, a maximum error in temperature of 5°C was assumed and the corresponding conductivity variation at each experimentally determined value in the isotherm was calculated and added to the total error.

Figure 6.1 shows the total error as calculated for select compositions at 750°C. The 0.5% and 10% samples were deleted from the plot for the sake of clarity. For samples with low overall conductivity (pure ceria), the errors in measurement show up on a larger scale in the log($\sigma$) plot. For samples with higher overall conductivity, errors become less significant (since the log of the error is small relative to the log of the total conductivity). The estimate of the effect of cracking, however, introduces considerable uncertainty into the magnitude of the conductivity of the materials (10, 20% samples). Fortunately, the qualitative character of the curve is not affected. In effect, the conductivity is simply scaled down. While the magnitude of the thermodynamic parameters derived from fitting of the conductivity data will include some uncertainty, the temperature and $pO_2$ dependence of the parameters should remain valid.

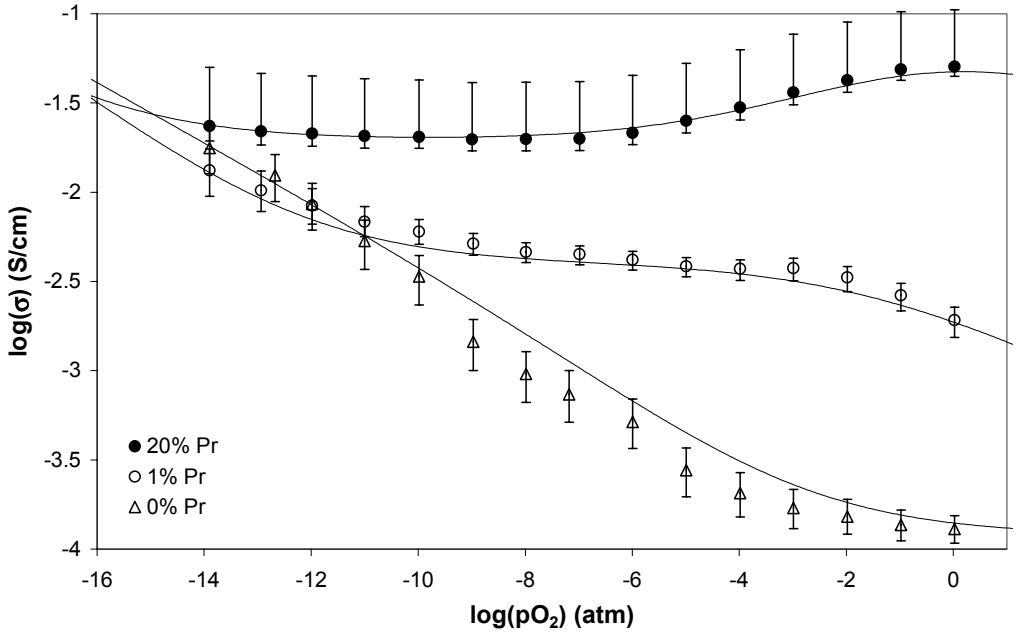


**Figure 6.1. Electrical conductivity isotherms for selected $Pr_xCe_{1-x}O_{2-\delta}$ samples at 750°C including estimated errors in the measurements. See text for details as to how the error bars were calculated.**

### 6.2.2. AC Impedance Measurements

AC impedance scans were collected at selected $pO_2$ values and temperatures in order to verify that the DC measurements used during collection of the isotherms were representative of the bulk conductivity of the PCO samples. Figure 5.26 shows an impedance spectrum for 1% PCO at 700°C and $10^{-1}$ atm $pO_2$. The scan is qualitatively representative of data collected at 600° and 700°C at $10^{-1}$ and $10^{-15}$ atm $pO_2$. Note that the apparent discontinuity in the large semicircle is an instrument error. The impedance analyzer used to collect the spectrum switches ranges at 1MHz, and the discontinuity in the pattern has been observed at this frequency numerous times on a wide range of samples. There are two components evident in the scan, a large semicircle at high frequencies (low Z') and a smaller response at low frequencies (high Z'). Note that neither response is dependent on the applied DC bias. It is probable that the large semicircle is representative of bulk conductivity in the system. The smaller semicircle is likely a grain boundary component. The majority of the resistance is accounted for by the large semicircle.

The samples used for AC impedance measurements were far from ideal. In the ideal case, a thin, flat disc with large electrodes (a simple capacitor of the material) is used. The bar samples were designed for four point measurements. As shown in Figure 3.2, the configuration measured during AC impedance analysis was a long bar sample with leads applied at approximately even intervals along the length of the specimen. AC measurements were made using the outer electrodes. The presence of the inner electrodes provided a low resistance path during AC measurements, therefore introducing error. Despite all the potential sources of error, in all but one of the cases examined, the difference between the conductivities calculated from AC vs. DC resistance measurements of lightly-doped PCO and pure $CeO_2$ was less than a factor of two. AC resistances yielded higher conductivity measurements in all cases. While a factor of two is certainly not trivial, given the crude nature of the AC impedance measurement, the agreement is acceptable.

Samples containing 10% or 20% Pr did not generally yield good AC impedance data. One of the 10% samples yielded no meaningful data whatsoever. The other 10% sample and the 20% sample did produce semicircular arcs, but all spectra exhibited strong DC bias dependence. The 4 point measurements, on the other hand, never exhibited any bias dependence. The resistances measured were also significantly lower than those measured using AC impedance as well. For instance, Figure 5.27 shows the AC impedance spectrum for 20% PCO at 700°C and $10^{-1}$ atm $pO_2$. The smallest resistance recorded was approximately 5000 ohms. Yet the equivalent 4 point DC resistance value for this sample was approximately 500 ohms, a full order of magnitude from the value suggested by AC impedance. The correlation coefficient ($R^2$) of the I/V curve collected using 4 point DC measurements was equal to 1. The AC impedance spectrum exhibited a strong bias effect. Clearly the AC measurement and the DC measurement do no correlate. Impedance spectroscopy is best suited to highly resistive samples as the material response is masked by interference from measurement leads, stray electromagnetic fields, etc, when the resistance is too low. Since the AC measurement was a 2 point measurement, if the quality of the contact between the Pt paint and ceramic sample was poor, this could also affect the AC response. Additionally, it is likely that the sample cracking present in

high Pr content samples interfered with collection of useful impedance data. As a result, the importance of grain boundary conductivity in the high Pr content samples could not be examined. It was assumed to be within acceptable limits, as in the case of samples containing less Pr.

### 6.2.3. Conductivity Fitting Routine

The defect model presented has many parameters which must be determined in order to quantitatively fit experimental electrical conductivity data. The oxygen vacancy mobility ($\mu_v$), cerium reduction constant ($K_R$), electron mobility ($\mu_e$), praseodymium ionization constant ($K_{Pr}$), and impurity band mobility ($\mu_{imp}$, only active in high Pr content samples) must all be examined in order to yield a consistent set of thermodynamic parameters. The order in which parameters were refined did affect the results of the fitting. Caution was taken to attempt to identify the parameters as independently as possible as oftentimes parameters displayed a co-dependence such that multiple combinations of two different parameters yielded equally good fitting results. For instance, both the cerium reduction constant and the electron mobility could be varied in order to fit increasing electronic conductivity at low $pO_2$ and high temperature. Likewise, fitting of the onset of the decrease in ionic conductivity at high $pO_2$ as Pr oxidizes from $Pr^{3+}$ to $Pr^{4+}$ was sensitive to both the value of $K_R$ and that of $K_{Pr}$. Whenever possible, portions of the conductivity isotherms in which only one mechanism dominates conductivity were fit independently of the rest of the isotherm in order to accurately determine one nearly independent parameter. That value was then fixed and subsequent parameters were refined. Values of fitting parameters taken from literature for similar systems (primarily pure ceria) were also used, either as starting points for further refinement or directly transferred into the PCO model if fitting of the parameters proved unproductive.

All fitting was performed on the base 10 log of both the conductivity and $pO_2$ values (as plotted). This served to weight the data so that all points in the isotherm were equally counted in minimization of the total error in the fit. In fitting each parameter in the model, the differences in conductivity between each experimental point and the corresponding point in the model were calculated, squared, and totaled. The parameter

being refined was then systematically increased or decreased in order to minimize the total error in the fit.

After all parameters had been individually refined, the best fit Arrhenius temperature dependence for the parameters was found. The best linear fits of log(parameter) vs. 1/T were taken as the final set of thermodynamic parameters describing conductivity in PCO. These best fit Arrhenius parameters are those used to generate the conductivity isotherms presented.

*6.2.3.1. Vacancy Mobility*

The first parameter examined in fitting a given isotherm was the ionic mobility. In each of the conductivity isotherms, there is a conductivity plateau corresponding to ionic conductivity fixed by dopant cations. Dopants include both background impurities and $Pr^{3+}$ ions. The plateau and the upturn at very low $pO_2$ was fit using a simple constant ionic conductivity and linear electronic conductivity with either a $pO_2^{-1/4}$ or $pO_2^{-1/5}$ dependence (the $pO_2^{-1/5}$ dependence accounts for a transition between $pO_2^{-1/4}$ and $pO_2^{-1/6}$). At the conductivity plateau, mobility of oxygen vacancies was calculated assuming that the vacancy concentration was set by the acceptor concentration ($2[V_O^{\bullet\bullet}] = [A^{/}]$, $\mu_v = \sigma_v/2e[V_O^{\bullet\bullet}]$ where e is elementary charge). The vacancy mobility was then assumed to be constant across the entire range of $pO_2$. It should be noted that at high vacancy concentrations, association may occur. Such association would effectively reduce the vacancy mobility, however, the value was assumed constant during this analysis. Effects of association will be examined below.

The vacancy mobilities obtained were plotted on a $\log(\sigma_v T)$ vs. 1/T plot so that the total activation energy for ionic conduction could be examined. See Figure 6.2 for these results. The total activation energy for conduction is given in the legend. Errors presented are the standard errors of regression for each fit. In other $CeO_2$-based oxygen ion conductor systems, the migration enthalpy for oxygen ions is approximately 0.6 eV.[31] The total activation energy for ionic conductivity is composed of both the migration enthalpy and an association energy between the oxygen vacancies and the ionized dopants in the system. This association term can be quite high, especially at high

concentrations of dopant ions, resulting in activation energies for ionic conductivity as high as 1.4eV in $Y_{0.20}Ce0_{.80}O_{1.9-\delta}$.[31] All samples containing Pr exhibit activation energies comparable to that found by other authors.[31,32,35] The activation energy for ion conductivity in pure $CeO_2$ is considerably higher than that in samples containing Pr, in agreement with previous work.[32,35] The results were also plotted as $\log(\sigma_v)$ vs. 1/T so that the magnitude of the ionic conductivity plateau could easily be observed (Figure 6.3).

Figure 6.4 shows the ionic conductivity of PCO compared to that of several other doped ceria systems and that of YSZ. The 10% and 20% PCO samples exhibited extensive cracking, as previously described. Nonetheless, the magnitude of the total ionic conductivity demonstrated by the samples is comparable to that of other doped ceria systems. The maximum observed ionic conductivity in PCO at 800°C is approximately half that observed in Gd or Sm doped ceria, two of the best ion conductors based on ceria. If the cracking problems experienced were eliminated, it is likely that the observed ionic conductivity of PCO would be higher still. The material appears to be a very good ionic conductor when all the Pr exists as $Pr^{3+}$, under reducing conditions.

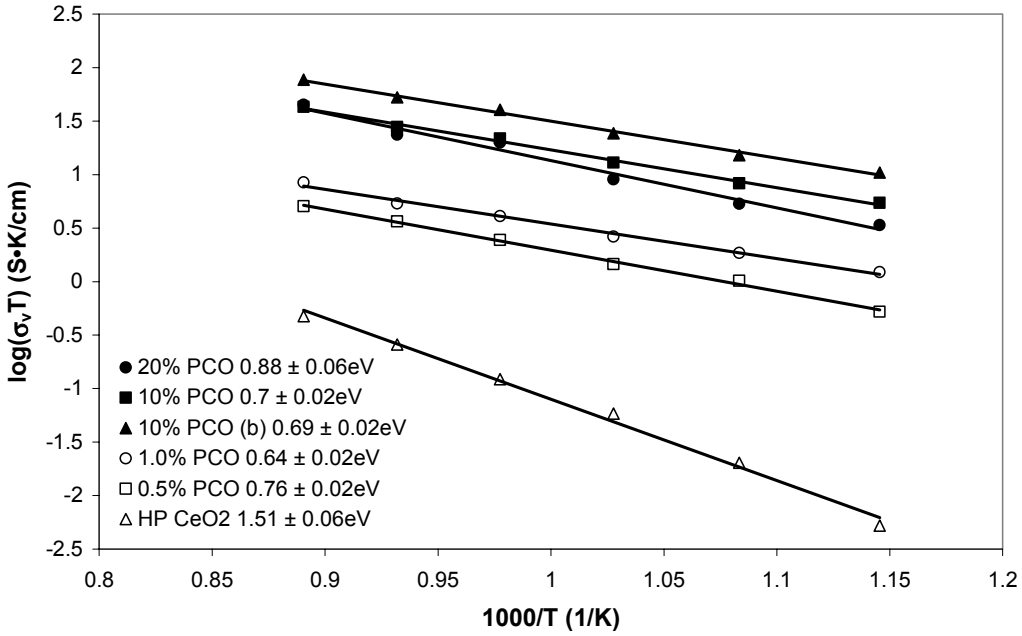


**Figure 6.2. Ionic conductivity plotted as $\log(\sigma_v T)$ vs. 1000/T. Activation energies are displayed in the legend. Errors presented are the standard errors of each linear regression.**

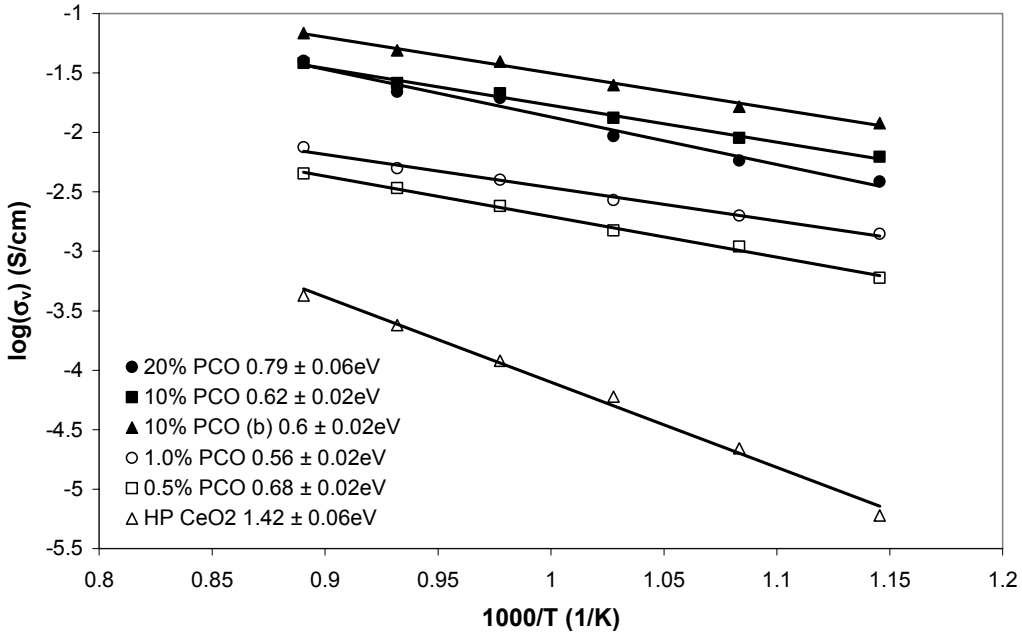


**Figure 6.3. Ionic conductivity plotted as $\log(\sigma_v)$ vs. 1000/T.**

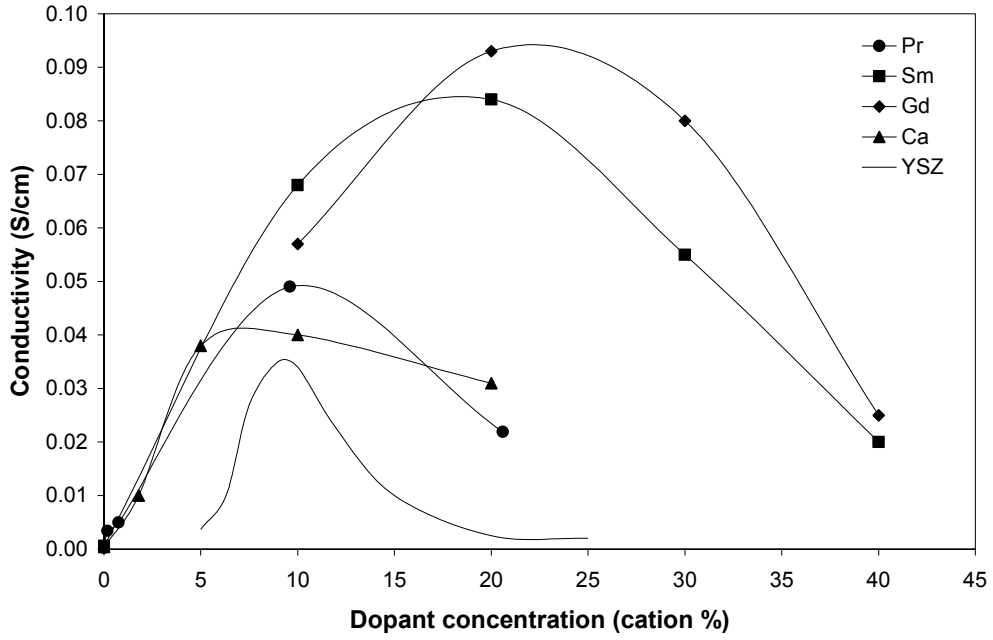


**Figure 6.4. Ionic conductivity at 800°C in Pr-doped ceria (this study), Sm[34], Gd[20], and Ca[35] doped ceria and YSZ[96].**

*6.2.3.2. Cerium Reduction Constant ($K_R$) and Electron Mobility ($\mu_e$)*

The degree of reduction achieved during collection of the conductivity isotherms was insufficient to meaningfully fit the $K_R$ and $\mu_e$ values successfully. These parameters determine the location and magnitude of the onset of electronically dominated conductivity at low $pO_2$, but in most isotherms, this region is not reached. Only at temperatures of 800°C or greater is increased electronic conductivity observed. Further data was required in order to identify the cerium reduction constant.

Partial isotherms from 800-1000°C were collected at highly reducing conditions in order to observe the necessary elevated electronic conductivity. These results were shown in Figure 5.20 through Figure 5.25. As both the $K_R$ and $\mu_e$ values determine the magnitude of the electronic conductivity, this data alone is insufficient to establish the values of both constants. It is known that the reduction constant for cerium generally decreases with additions of dopant ions.[20,28,29,90,97-99] The electron mobility is not expected to be a strong function of dopant concentration in a solid solution system such as PCO. In the absence of additional data to quantify the electron mobility (such as Hall measurements or high

quality thermoelectric power data), the electron mobility was assumed to be independent of Pr concentration and equal to that of pure $CeO_2$, a better assumption at low than at high Pr concentrations. The electron mobility in $CeO_2$ is available as a function of temperature in the literature[89]. The electron mobility used is given by:

$$\mu_e = \frac{390}{T} exp\left(\frac{-0.4\,eV}{kT}\right) \tag{6.1}$$

With the electron mobility defined, the values of $K_R$ could be fit to the high temperature, high reduction isotherms. These data are nearly independent of other fitting parameters ($\mu_v$, $K_{Pr}$, or $\mu_{imp}$) and were therefore the most reliable for determination of $K_R$. As seen in Figure 5.20 through Figure 5.25, the fits to the data are generally quite good. The temperature dependence of $K_R$ will be discussed below.

*6.2.3.3. Praseodymium Ionization Constant and Impurity Mobility*

With previously determined values of $\mu_v$, $\mu_e$, and $K_R$, the praseodymium ionization constant ($K_{Pr}$) was next fit to the data. The primary effect of varying $K_{Pr}$ is to shift the onset of the drop in ionic conductivity associated with the oxidation of $Pr^{3+}$ to $Pr^{4+}$, as well as the maximum in the impurity band conductivity (if impurity band conductivity is significant). Impurity conductivity was ignored at low Pr contents (0.5% and 1% Pr). There is insignificant overlap between Pr states at such low concentrations and the impurity band contribution is not observed. At higher Pr concentrations, $K_{Pr}$ determined the $Pr^{3+}/Pr^{4+}$ ratio (and the location of the maximum in impurity band conductivity on the $pO_2$ axis) while the $\mu_{imp}$ value determined the magnitude of the rise in conductivity. After automated fitting, the impurity mobility was manually varied in order to yield impurity band conductivities that corresponded to the maximum in impurity band conductivity for a given data set (without regard to misfit at points on either side of the impurity band conductivity maximum). The temperature dependence of the parameters will be discussed below.

### 6.2.4. Quality of Conductivity Fitting and Discrepancies

As seen in the conductivity isotherms (Figure 5.8 through Figure 5.19), the overall quality of the fitting is quite good. Qualitatively, the entire range of observed $pO_2$

dependence is accounted for. At low $pO_2$ values, electronic conductivity dominates, followed by an ionic conductivity plateau. In compositions containing low amounts of Pr, this ionic conductivity falls off at high $pO_2$ values as $Pr^{3+}$ oxidizes to $Pr^{4+}$. In compositions containing higher amounts of Pr, the drop in ionic conductivity is masked by electronic hopping conductivity in an impurity band. There are some notable deviations from expected behavior, however, both in the experimental data and in the correspondence between the data and the model.

In the isotherms for pure, nominally undoped $CeO_2$ (Figure 5.8), there are noticeable deviations in the experimentally determined conductivity values from the smooth, linear variations predicted by the defect model. There are a number of possible explanations. First, this could be a result of simple experimental error. It is possible that the $pO_2$ near the $CeO_2$ sample was locally different from that at the sample oxygen sensor. The sensor was located very close to the $CeO_2$ sample, however (as shown in Figure 3.3). It appears that an error in $pO_2$ of two to three orders of magnitude would be required to produce the deviation observed at 600°C and $10^{-7}$ atm $pO_2$. The likelihood of such drastic local gradients in $pO_2$ seems low. At such low temperatures, achieving equilibrium conditions took a very long time (several days). As previously mentioned, the oxygen pump is not particularly well suited to these types of measurements, due to the instabilities experienced at intermediate $pO_2$ values. It is highly likely that true equilibrium conditions were not achieved at the lowest temperatures in regions of particularly slow equilibration. In addition, both $CeO_2$ and $PrO_2$ are known to undergo a series of transitions to ordered phases at low temperatures (see the phase diagram in Figure 1.2). Some combination of difficulty in maintaining steady state at intermediate $pO_2$ values and slow ordering transformations likely resulted in non-equilibrium measurements. Such deviations have been reported in the literature, though no explanation as to the source of these deviations was presented.[100]

The 0.5% and 1% samples (Figure 5.9 and Figure 5.10) exhibit a weaker than expected conductivity increase at low $pO_2$ values and low temperatures. The $K_R$ value that determines the model fit was fit at higher temperature (where the data is more reliable). The elevated electronic conductivity observed at 600-700°C in the 0.5 and 1% samples at

low $pO_2$ is, once again, likely due to insufficient equilibration and possibly due to the formation of ordered phases. The isotherms were generally collected starting at low $pO_2$ values and working upward. The high conductivity, which began to equilibrate under reducing conditions, persisted as $pO_2$ was increased. Further patience and stable oxygen partial pressure control would likely have resulted in data closer to the model fit presented (since the model was fit to data at higher temperatures where equilibration is faster, then extrapolated to low temperature).

The deviations from the model observed at high $pO_2$ values in 10 and 20% Pr doped samples cannot be due to slow equilibration. Take, for instance, the 600° isotherm for the 20% Pr sample (Figure 5.13). The isotherm was collected from low to high $pO_2$, yet on both sides of the conductivity maximum (near $pO_2 = 10^{-2}$ atm), the measured conductivity is significantly lower than that predicted by the model. If this were an equilibration artifact, the conductivity would fall below the prediction as the impurity band contribution increased, but above it as it decreased again at $pO_2 > 10^{-2}$ atm.

The impurity band hopping conductivity formula is given in equation (4.23). If we consider this formula in its most basic sense and ignore the effects of temperature (reasonable for an isotherm), then it reduces to:

$$\sigma_{imp} = \sigma^{o} Nc(1-c) \tag{6.2}$$

Here, conductivity is a function of the concentration dependence of the carrier (Nc) multiplied by the concentration dependence of the mobility (1-c). The c(1-c) behavior accounts for two conditions required for an electron to hop. The c term determines whether or not there is an electron at a given site. The 1-c term is the probability that there is an empty site adjacent to the filled one so that the electron has a place to move to.

It has been proposed[101] that not only must there be an empty site available to jump to, but that the nearest neighbors of that empty site must also be surrounded by empty sites so that occupation by a jump does not bring two carriers too close together and create a local charge imbalance. The result is to increase the power of the 1-c dependence. The term 1-c is the probability of finding an empty site adjacent to a given occupied site, and

$(1-c)^{n-1}$ is the probability that the other neighbors of the empty site are not occupied where n is the coordination of the sites on which hopping occurs.

However, the restriction that no two adjacent sites be occupied by an electron is unreasonable in the case at hand. Polaron hopping theory, like most of defect chemistry, was derived for a dilute solution model. An underlying assumption is that the effects of one dopant cation do not interfere with the effects of another. Dopants are assumed to be isolated within a host matrix. This is certainly not the case in many of the PCO compositions examined during this study. At 20% Pr, one in every 5 cations has been replaced in the $CeO_2$ host material. In the fluorite structure, the cation position has 12 nearest cation neighbors (an FCC arrangement of cations). The probability of finding a Pr ion without one or even two more Pr ions adjacent to it is extremely low. At the maximum in impurity band conductivity, the concentrations of $Pr^{3+}$ and $Pr^{4+}$ are equal. The probability of all $Pr^{3+}$ being separated from all the $Pr^{4+}$ ions is very low. Applying the restriction that a hop can only occur if such separation is maintained would not be realistic.

If instead occupation of adjacent sites is allowed to some degree, the occupancy restriction presented for the dilute solution case begins to relax. If instead of requiring that all nearest neighbors of an empty site are empty as well, only some fraction of the nearest neighbors must be unoccupied, the power dependence of the 1-c term begins to decrease. Local charge neutrality is still maintained, but on a larger scale than individual ions (two charged species may exist adjacent to one another, but three charges in close proximity is not allowed, for instance). The net effect is to increase the power law dependence of the c(1-c) behavior to $c^n(1-c)^n$ where $n > 1$. Note that the symmetry of the situation results in an increase in both the power of c and 1-c (since a hop is symmetrical, moving an electron in one direction and a hole in the other).

Another factor worthy of note is that polaron hopping theory is derived for the case in which the only charged species in the system are the electronic carriers and the dopant ions that produce them. In PCO, the addition of two $Pr^{3+}$ ions also results in the formation of a doubly-charged oxygen vacancy. The effects of these additional charge

centers is not accounted for. As the concentration of vacancies increases, interaction with the hopping polarons becomes more and more likely. A positively charged polaron would be repelled from positively charged oxygen vacancies. Negatively charged polarons would be attracted to vacancies. The result would be an increased activation energy for migration ($E_H$ in equation (4.23)). Since the vacancy concentration is proportional to the concentration of $Pr^{3+}$, the increase in migration enthalpy would likely be a function of concentration as well. This, too, could increase the power of the concentration dependence in the polaron hopping formula. This is essentially an argument for vacancy-polaron defect association. This notion is further supported by the fact that the deviations observed in the conductivity isotherms are most extreme at low temperatures. Defect complexes form when the temperature is low enough for them to be thermodynamically favorable. At higher temperatures, defect association is less likely.

Either of the mechanisms described would result in a steeper rise and fall of the impurity band conductivity as a function of $pO_2$, which would bring the proposed model into closer agreement with the experimental data. The fits for the 20% Pr sample were modified to use a $c^2(1-c)^2$ dependence, rather than the c(1-c) model previously presented. The $K_{Pr}$ and $\mu_e$ values were re-fitted, and the results are shown in Figure 6.5 and Figure 6.6. At 600°C, where the effects of defect association are most prevalent, the increase to $c^2(1-c)^2$ dependence is still not strong enough to fit the experimental data. The fit is quite good at 650° and 700°C. At temperatures higher than 700°C, the effects of defect association are nearly eliminated and the c(1-c) model fits the data well.

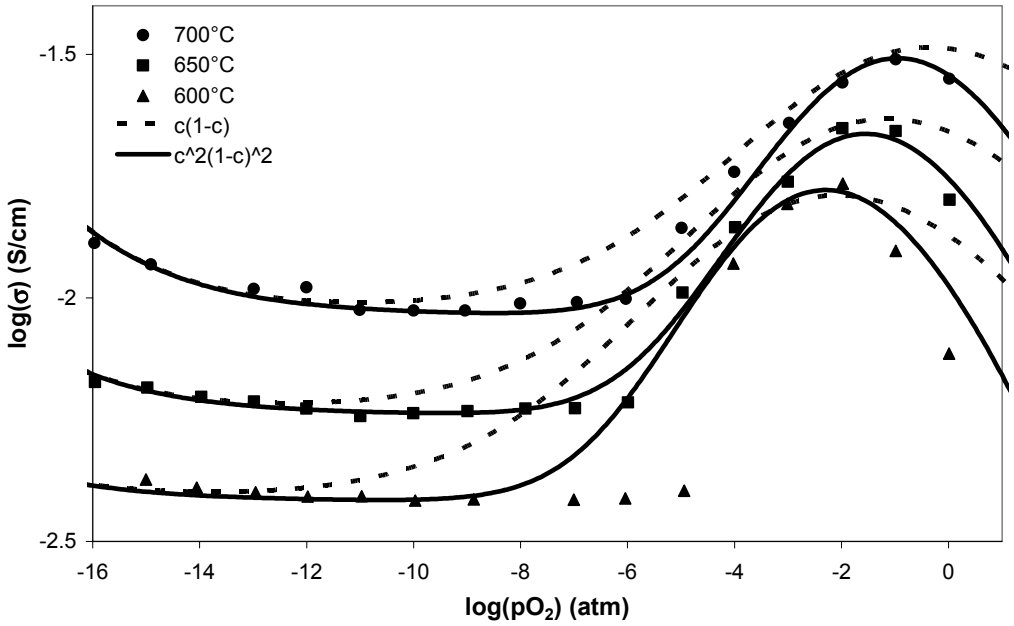


**Figure 6.5. Conductivity isotherms in $Pr_{0.20}Ce_{0.80}O_{2-\delta}$ from 600-700°C. The impurity band conductivity was fit using both a c(1-c) and $c^2(1-c)^2$ model.**

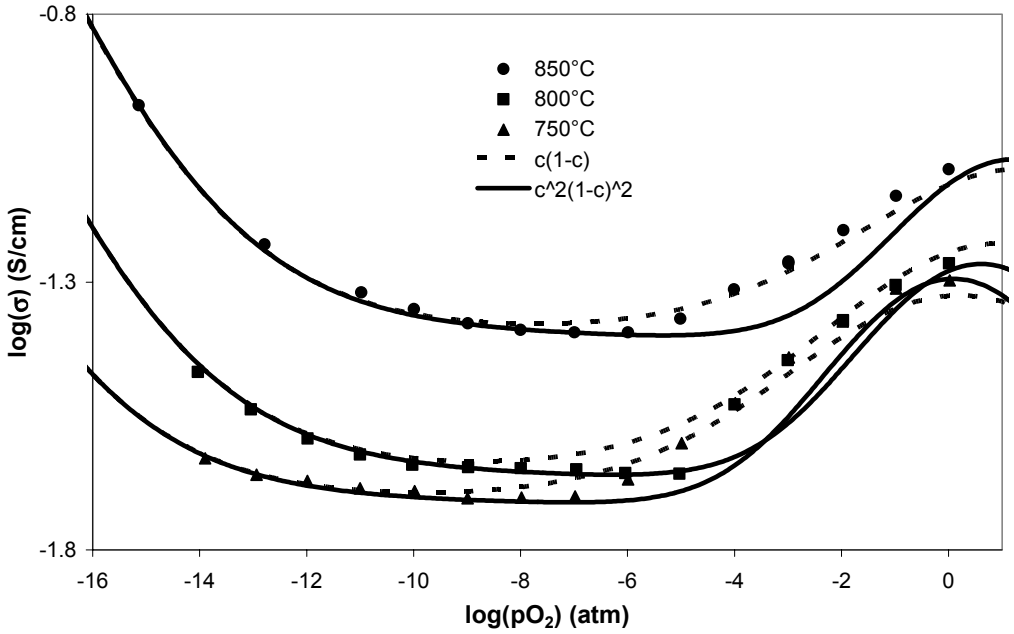


**Figure 6.6. Conductivity isotherms in $Pr_{0.20}Ce_{0.80}O_{2-\delta}$ from 750-850°C. The impurity band conductivity was fit using both a c(1-c) and $c^2(1-c)^2$ model.**

### 6.2.5. Thermodynamic Fitting Parameters

Despite the discrepancies in the data fits discussed above, the overall quality of the fitting is still quite good. It is useful to examine the fitting parameters found as a function of temperature.

#### *6.2.5.1. Cerium Reduction Constant*

The cerium reduction constant was fitted using data collected at high temperature and low $pO_2$. Figure 6.7 shows the temperature dependence of the $K_R$ values for each composition studied. Errors on the activation energies presented in the legend are the standard errors of regression calculated from high temperature fits (800-1000°C). The errors of each point in the Arrhenius plot were not analyzed. As the values presented were extrapolated from high temperature assuming Arrhenius behavior, no deviations from linear Arrhenius behavior are shown in the plot.

It has been shown that the activation energy of the cerium reduction constant (the cerium reduction enthalpy) tends to decrease with additions of dopant cations[20,28,29,90,97-99]. The highest Pr content samples do demonstrate considerably lower reduction enthalpies than compositions containing small amounts of Pr. There is an increase in reduction enthalpy from pure ceria to 0.5% and 1% PCO, however. The reduction enthalpy for pure $CeO_2$ is approximately 4.7eV, in agreement with literature values. The values for 0.5% and 1% Pr-containing samples are approximately 5.3 and 5.0, respectively. The source of this increase is unknown. Examination of Figure 5.21 through Figure 5.25 shows that the fits for samples containing low amounts of Pr were quite good, with the bulk of the discrepancies apparent near the plateau region extrapolated from lower temperatures. If the plateau value used was incorrect, then the fit of $K_R$ will incorporate that error. At high temperatures and low $pO_2$ values, conductivity is dominated by intrinsic reduction. The reduction constant is proportional to $\sigma_e^3$, so small errors in conductivity will propagate to large errors in $K_R$. If the ionic conductivity used in fitting the data were significantly off, the fits of $K_R$ would magnify that error. Figure 6.8 shows the variation of the cerium reduction constant with Pr content. Within the estimated error at each point, the data exhibit a nearly linear decrease with increasing Pr content, the 0.5% sample being the only exception. As the total Pr content is increased, the total amount of 3+

charge cations in the system increases (for a fixed $pO_2$ and temperature). This means that the average valence of cations in the system decreases. In addition, it has been observed that increases in Pr content resulted in an increased lattice parameter (see Figure 5.6). The decrease in the average valence of cations neighboring oxygen anions in the material may result in a decrease in the binding energy holding a given oxygen ion in place. In addition, the expansion of the lattice resulting from the addition of Pr to the system would strain the bonds holding oxygen ions in the structure. Both these contributions could result in a lower overall reduction enthalpy of cerium in the system.[97]

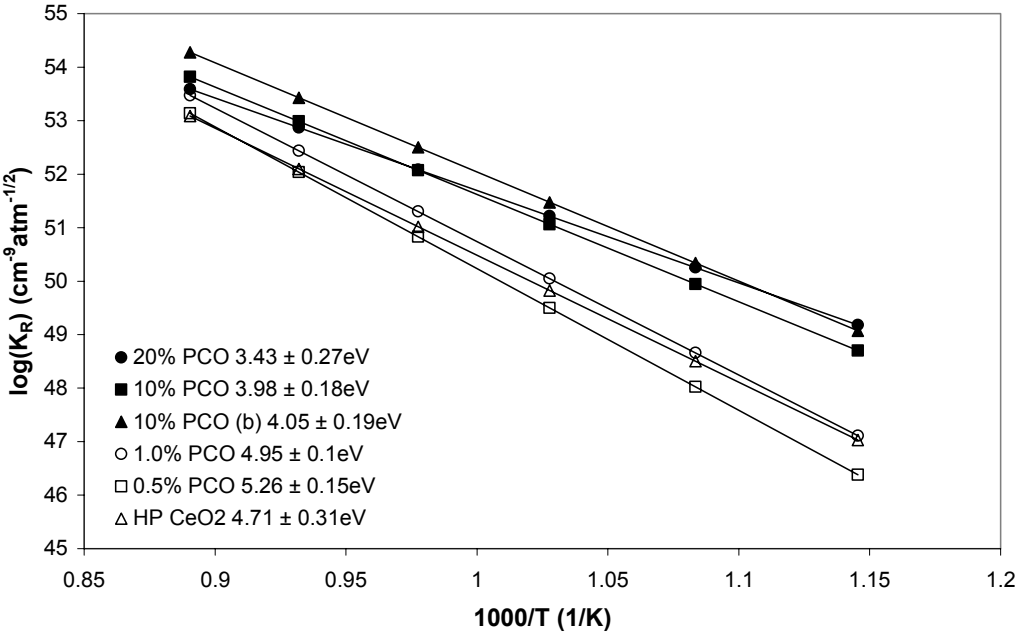


**Figure 6.7. Arrhenius temperature dependence of the cerium reduction constant ($K_R$) in PCO. Reduction enthalpies for each composition are given in the legend.**

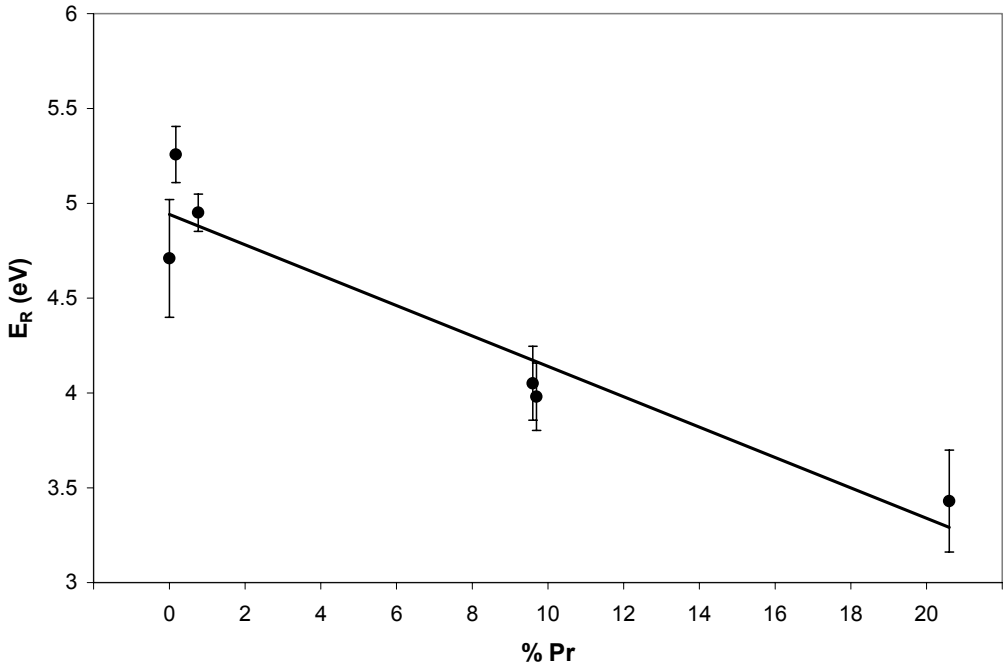


**Figure 6.8. Reduction enthalpy of cerium ($E_R$) as a function of Pr content in PCO.**

*6.2.5.2. Praseodymium Ionization Constant*

The Arrhenius plot of the Pr ionization constant is shown in Figure 6.9. Errors on the activation energies presented in the legend are standard errors of regression; again, no analysis of the errors in each point in the Arrhenius plot was performed. As defined in equation (4.13), $K_{Pr}$ is the reaction constant for the ionization of $Pr^{3+}$ to $Pr^{4+}$ in PCO, accompanied by the liberation of a conducting electron. The enthalpy associated with this reaction is the amount of energy required to move an electron from the $Pr^{3+}$ state within the band gap to the conduction band, or the trap depth as measured from the conduction band edge. There are two distinct behaviors observed in Figure 6.9. For high concentrations of Pr, the apparent trap depth is approximately 1eV. The 0.5 and 1% PCO, the trap depth is closer to 1.6eV. However, it should be noted that the value of $K_{Pr}$ derived from fitting of the conductivity isotherm is quite dependent of the value of $K_R$ used. Since the $K_R$ values for 0.5% and 1% PCO have already been drawn into question, the values of the activation energy for $K_{Pr}$ at those compositions is also subject to error. The ionization enthalpy for Pr in PCO is shown as a function of total Pr content in Figure 6.10. The lower ionization energy observed at high Pr contents may be the result of

impurity band formation. At low percentages of Pr, individual Pr ions form discrete traps in the $CeO_2$ band gap. As more Pr is added, these levels begin to overlap and broaden to form a band. This band has a finite width. If the width of the band expands symmetrically about the original, isolated Pr trap energy, then the observed energy difference between the conduction band and impurity band will decrease relative to the distance between isolated trap levels and the conduction band edge. See the inset in Figure 6.10 for a graphical representation.

The only other study addressing the electronic conductivity of Pr doped cerium oxide was that of Lubke[22] and coworkers. They used a Hebb-Wagner polarization cell with a platinum electrode in order to examine electronic conductivity as a function of $pO_2$ and temperature in $Ce_{0.8}Gd_{0.17}Pr_{0.03}O_{1.9-\delta}$. The platinum electrode served to block ionic conductivity, thereby passing only the electronic contribution. They found no evidence of impurity band formation at 3% Pr doping, which is not surprising at this relatively low concentration. They did observed increased p-type conductivity over that of pure $Ce_{0.8}Gd_{0.20}O_{1.9-\delta}$. Their results were modeled with a Pr trap depth for hole conduction of 0.15eV as measured from the ceria valence band. This is an extremely shallow trap compared to the values measured in this study. They used an optical band gap of 5.5 eV for $CeO_2$.[102] The trap depth in 1% PCO measured in this study was approximately 1.6 eV, measured from the conduction band edge, implying approximately 3.9 eV between the valence band and the Pr trap (using 5.5 eV as the ceria band gap). Clearly there is a discrepancy between these studies. If the energy difference between the valence band and Pr level were as low as 0.1-0.2 eV, absorption of light would occur for all visible wavelengths, resulting in a grey or black material. The 1% PCO produced in this study was deep pink/red, indicating absorption in the visible spectrum, which is inconsistent with an ionization energy of 0.15 eV. However, the model presented by Lubke was devised in order to obtain qualitative conductivity behavior only. It is possible that the enthalpies used in calculating their model require significant adjustment. The authors note that while their model qualitatively describes the trends observed, “a more detailed description has to be postponed until definite data with respect to the thermal band gap

and the standard enthalpies are available." Further study is warranted in order to clarify this discrepancy.

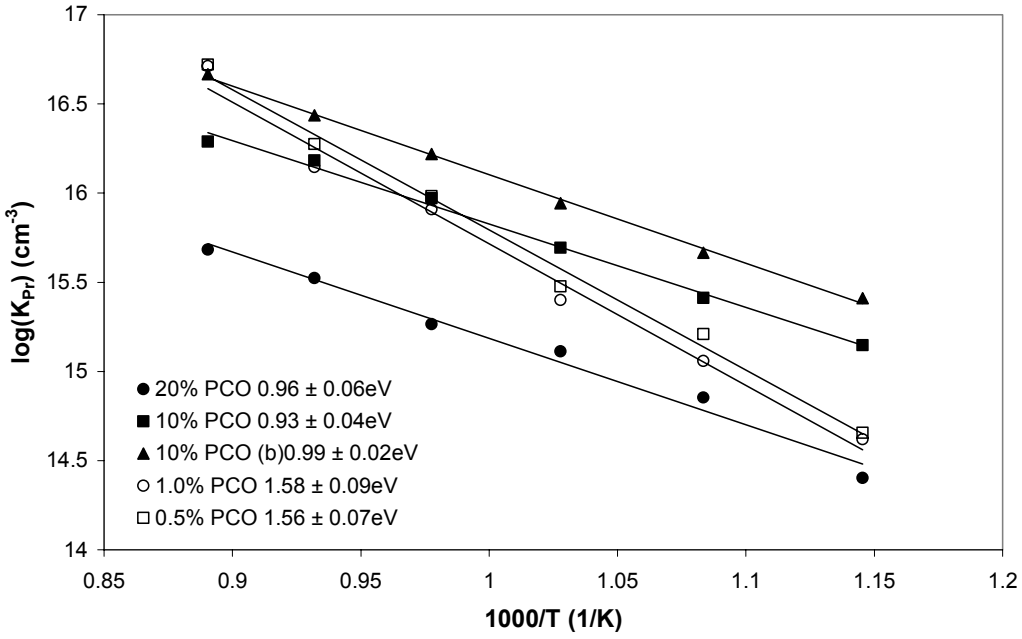


**Figure 6.9. Arrhenius temperature dependence of the praseodymium ionization constant ($K_{Pr}$) in PCO. Enthalpies for each composition are given in the legend.**

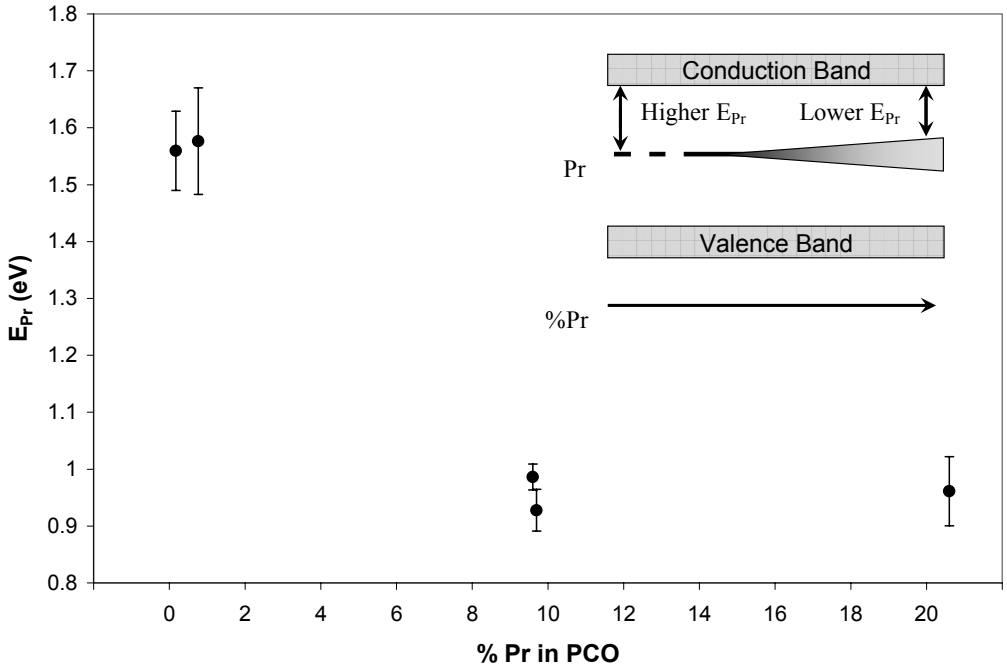


**Figure 6.10. Praseodymium ionization enthalpy ($E_{Pr}$) as a function of Pr content in PCO.**

*6.2.5.3. Impurity Band Mobility*

The impurity band mobility was only fit for compositions containing high amounts of Pr (10% and 20% PCO). Figure 6.11 shows the Arrhenius behavior of the impurity mobility (on a μT vs. 1/T scale such that accurate activation energies may be obtained). The errors in activation energy presented represent the standard error of regression; again, no analysis of the error at each point in the Arrhenius plots was performed. The total magnitude of the impurity band mobility was on the order of $10^{-5}$ to $10^{-4}$ $cm^2/Vs$, approximately one to two orders of magnitude lower than the electron hopping mobility in pure $CeO_2$. The migration enthalpy is approximately 0.55-0.6 eV, about 50% higher than the migration enthalpy in pure $CeO_2$ (0.4 eV). Neither of these results is unexpected. Both the magnitude and activation energy of impurity band conductivity are consistent with a diluted Pr sub-lattice in the $CeO_2$ host material. Relative isolation of Pr states compared to pure ceria results in the higher migration enthalpy and lower overall hopping mobility.

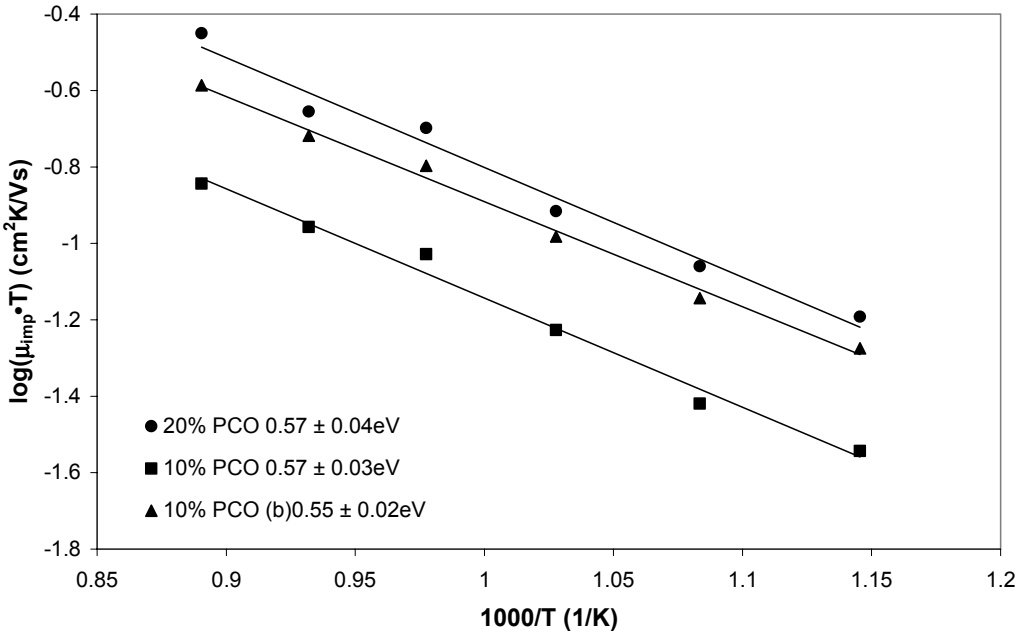


**Figure 6.11. Modified Arrhenius plot of impurity mobility ($\mu_{imp}$) in PCO. The legend shows calculated migration enthalpies for each composition.**

### 6.2.6. Electrolytic Domain Boundary

Based on the defect model described, it is possible to calculate the electrolytic domain boundary for PCO. The electrolytic domain is defined as the range of $pO_2$ and temperature over which the material behaves primarily as an oxygen ion conductor (where the transference number for ionic conduction is greater than 0.5). Figure 6.12 shows the transference numbers for oxygen ions, electrons created by reduction of cerium, and impurity band hopping conduction in 20% PCO at 800°C. The electrolytic domain boundaries are marked. Figure 6.13 shows the electrolytic domain for 20% PCO as a function of temperature. At high $pO_2$ values, the impurity band hopping conductivity overwhelms the ionic conductivity and the material behaves primarily as an electronic conductor. Under highly reducing conditions, reduction of the cerium host material results in the generation of free electrons which dominate the total conductivity. Between the two lines plotted, the material behaves primarily as an oxygen ion conductor. Note that the domain boundaries were calculated using the defect model derived and that the fitting errors present in the model are represented here as well. The high $pO_2$ electrolytic

domain boundary (for Pr hopping conductivity) actually falls at higher $pO_2$ values than those shown in Figure 6.13, particularly at the lowest temperatures. As shown in Figure 5.25, the model fits of impurity band conductivity estimate a higher impurity band conductivity than that actually observed in 20% PCO. Ionic conductivity is dominant to higher $pO_2$ values than those predicted by the model. An estimate of the actual domain boundary is shown in Figure 6.13 for comparison.

It is possible to plot the electrolytic domain boundary for all PCO compositions, but the plot shown demonstrates the general character observed. At 0.5% and 1% Pr, there is no impurity band hopping contribution to the total conductivity, so the material remains an ion conductor to high $pO_2$ values.

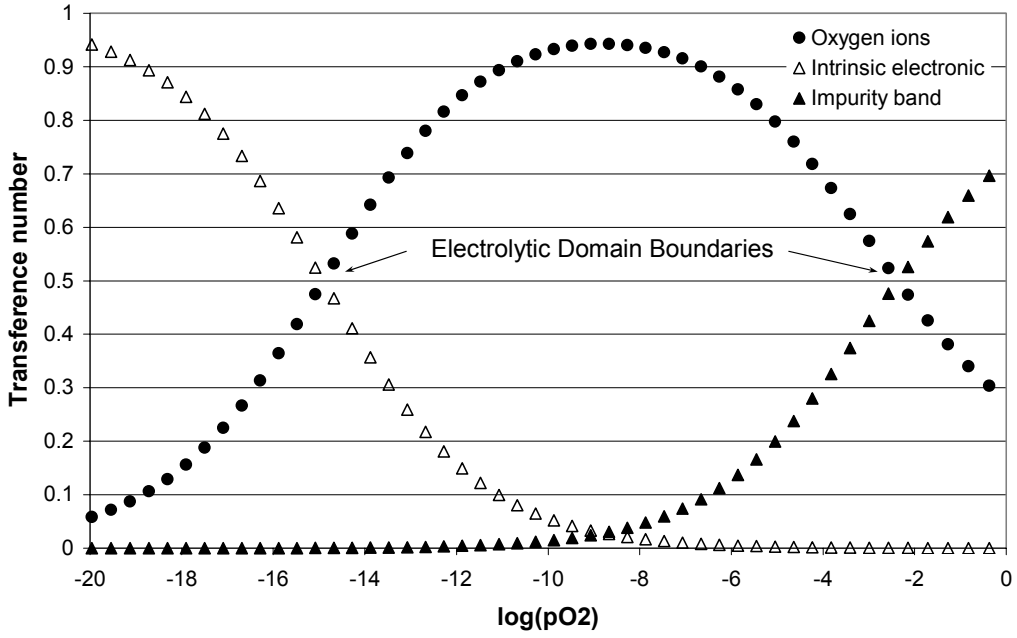


**Figure 6.12. Transference numbers for 20% PCO at 800°C.**

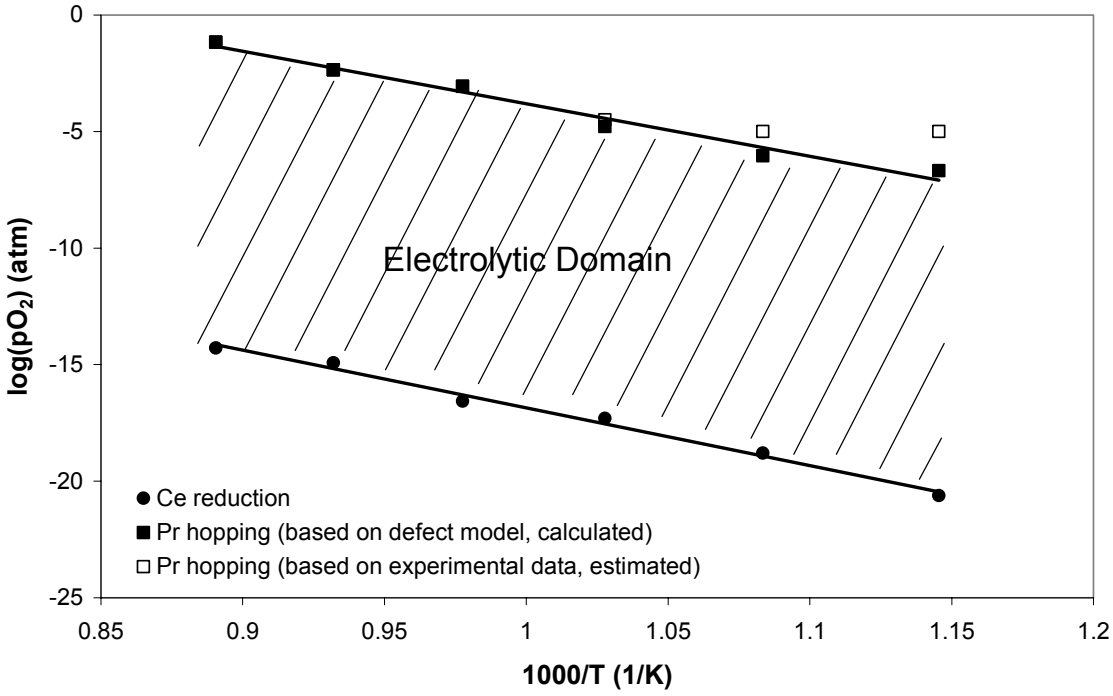


**Figure 6.13. The electrolytic domain boundary for 20% PCO, as calculated using the defect model derived.**

The temperature dependence of the ionic transference number in air is shown in Figure 6.13. The transference numbers were derived from the defect model derived, not from the actual conductivity data. For nominally undoped $CeO_2$, 0.5% and 1% PCO, there is no significant impurity band conductivity present. As indicated in equations (4.27) and (4.22), the electron conductivity increases exponentially with $E=E_R/2+E_H \approx 2.8$ eV, whereas oxygen ion concentration is fixed such that the activation energy is only the migration enthalpy (≈0.7 eV for 0.5% and 1% PCO, ≈1.5 eV for undoped $CeO_2$). Increasing temperature increases electronic conductivity more than ionic conductivity, so the ionic transference number decreases. For heavily doped samples, an unusual increase in the ionic transference number is observed with increasing temperature. Electronic conductivity occurs at high $pO_2$ by impurity band conduction. As temperature is increased, the maximum in the impurity band conductivity shifts to $pO_2$ values greater than 0.21 atm with increasing temperature, resulting in a net increase in the ionic transference number. The overall ionic transference number is lower for 20% PCO

relative to 10% PCO due to the increased impurity band conductivity in the 20% sample. The temperature dependence of ionic transference number in heavily doped PCO is consistent with that observed experimentally by Takasu[44] and Shuk[27] (see Figure 1.10 and Figure 1.13).

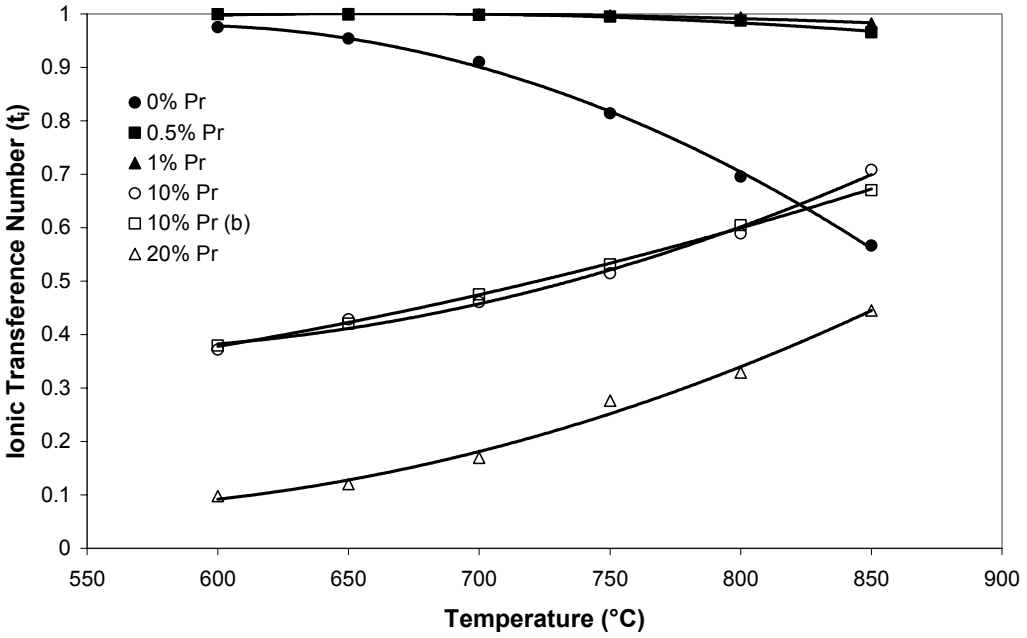


**Figure 6.14. Ionic transference number in PCO in air as a function of temperature. Transference numbers are calculated from the defect model presented.**

## *6.3. Coulometric Titration*

### 6.3.1. Errors in the Measurement

Titration results were shown in Figure 5.28 through Figure 5.31. Again, note that the total change in stoichiometry is plotted, not the total stoichiometry for the system. The reference state for the experiments was air (0.21 atm $pO_2$), and there is a significant amount of nonstoichiometry present at high temperature in air in most PCO compositions.

The general trends observed in the titration plots follow anticipated behavior. There are some noticeable deviations worth mentioning, however. First, in Figure 5.28, notice that the total change in nonstoichiometry exceeds the maximum nonstoichiometry predicted in the system. The dotted line represents the maximum amount of nonstoichiometry

anticipated based on the total Pr level. Each pair of $Pr^{3+}$ ions introduced generate one oxygen vacancy according to equation (4.10). Given that the data only extends to $10^{-7}$ atm $pO_2$, it is not expected that the cerium host material will reduce appreciably. The maximum concentration of vacancies expected is therefore one half the concentration of Pr in the material. In the 1% sample, however, this upper limit is exceeded. In addition, upon reduction from atmospheric pressure, it appears that the total nonstoichiometry approaches the maximum predicted value asymptotically until approximately $10^{-3}$ atm $pO_2$, at which point there is a transition to a linear increase in nonstoichiometry. It is likely that there was a small leak in the titration cell. At pressures greater than $10^{-3}$ atm $pO_2$, the leak was insignificant relative to the changes in nonstoichiometry of the 1% PCO. Below $10^{-3}$, however, contributions from the leak appear to be comparable to that of the sample response.

It is also possible that polarization of the titration cell at low $pO_2$ values contributes to the error. As the pressure difference between the sample and the outside environment increased, a Nernst voltage developed on the zirconia pump. The larger the difference in $pO_2$, the larger this voltage became. The total voltage on the cell was limited to 0.9V in order to prevent reduction of the zirconia pump. As a result, smaller pumping currents were required and pumping was slowed significantly at pressures significantly below atmospheric pressure. Applications of very small currents (microamps) for very long times (hours to days) were required to remove oxygen from the cell. It is possible that during these long applications of small current, some of the current leaked to the surrounding kiln furniture, through the high impedance of attached instrumentation, etc. This, too, could result in an apparent increase in nonstoichiometry beyond that resulting from reduction of the PCO sample.

The results for the 5% sample shown in Figure 5.29 exhibit the same apparent upturn in nonstoichiometry near $10^{-3}$ atm $pO_2$ as described in the 1% PCO results. The deviation from the smooth, asymptotic approach is visible in both the 500° and 550°C data. The same reasons presented for the 1% PCO sample apply to this case as well.

The lowest temperature data for the 20% sample (in Figure 5.30) exhibit a different behavior than that observed in the 1% and 5% PCO samples. There are significant deviations from the smooth asymptotic increase in nonstoichiometry with decreasing $pO_2$ observed in the higher temperature data. At relatively high $pO_2$ values, the nonstoichiometry begins to deviate from the expected path and takes on a linear dependence on the log(nonstoichiometry) vs. log($pO_2$) plot. This is most likely a region of inequilibrium. At the lowest temperatures, it is likely that the material cannot liberate oxygen quickly enough to keep up as it is electrochemically pumped from the cell. The observed change in nonstoichiometry is therefore less than the true nonstoichiometry in the system. This will make any conclusions based on the lowest temperature data questionable.

### 6.3.2. Total Nonstoichiometry vs. Change in Nonstoichiometry

In order to see trends in the nonstoichiometry of a given PCO composition as a function of temperature, the initial nonstoichiometry of the reference state must be added to the raw data, which only includes changes in nonstoichiometry from the reference. In order to illustrate the importance of accounting for the initial nonstoichiometry, plots of nonstoichiometry based on the results of conductivity fitting were constructed. The oxygen vacancy concentration is one of the parameters calculated during fitting of the electronic conductivity. This vacancy concentration was converted to a total nonstoichiometry. The initial nonstoichiometry was calculated based on the defect model, both the "raw data" changes in nonstoichiometry and the total nonstoichiometry were plotted as functions of oxygen pressure at several temperatures. Figure 6.15 shows the calculated plots of raw data. Figure 6.16 shows the calculated total nonstoichiometries. The raw data seems to indicate the counterintuitive result that nonstoichiometry is lower for a given $pO_2$ at higher temperatures. Only once the initial nonstoichiometry has been accounted for does the expected trend in nonstoichiometry become evident.

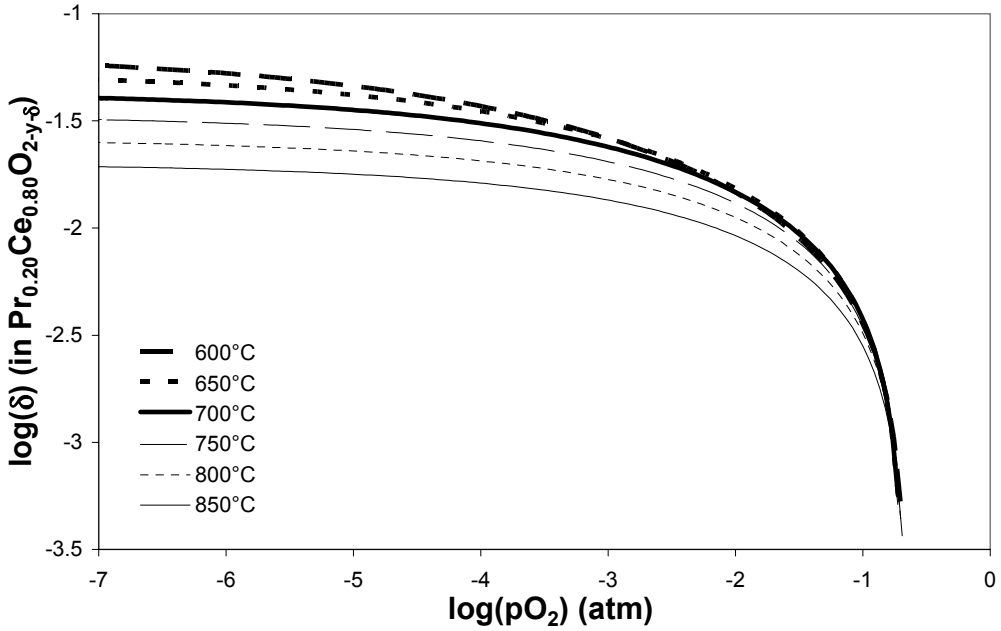


**Figure 6.15. Calculated coulometric titration "raw data" for 20% PCO.**

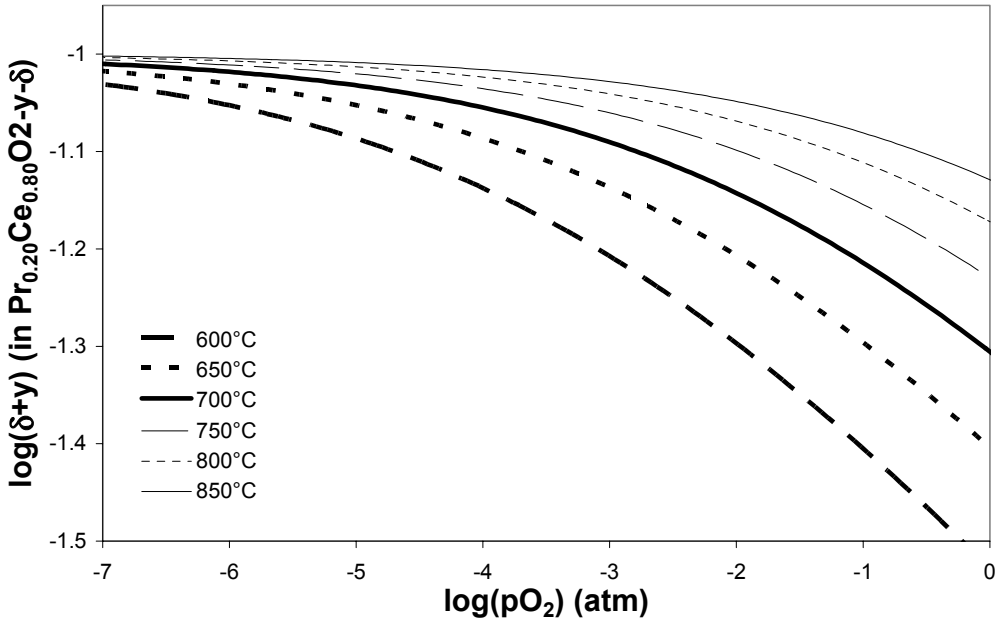


**Figure 6.16. Calculated total nonstoichiometry for 20% PCO.**

### 6.3.3. Titration Fitting Routine

Only select values of the titration data were fit. The data was edited such that there was one experimental point per half-decade of $pO_2$, except at high $pO_2$ values where tighter spacing was allowed. An approximately even distribution of points along a given coulometric titration data set was established such that no one section of the scan was given more weight than another in a least squares fitting routine.

The values of $K_R$ were once again extrapolated from the high temperature conductivity data. Much lower $pO_2$ values than those achieved during coulometric titration would have been required in order to experimentally fit the $K_R$ values. Mobility values have no effect on the titration fitting. The only parameters to be fit were the praseodymium ionization constant ($K_{Pr}$) and the initial nonstoichiometry (y). Initial values of $K_{Pr}$ were taken from the electrical conductivity fitting. Initial values of y were calculated for the defect model. Both parameters were then refined in succession, using a sum of squares minimization of the total error between the experimental data and model fit, as was performed during electrical conductivity fitting.

### 6.3.4. Fitting Results

The results of coulometric titration fitting in 20% PCO are shown in Figure 6.17. It was not possible to fit the 1% data. The model being fitted has an inherent upper limit on the total nonstoichiometry for the system, since the reduction mechanism assumed in the defect model is reduction of $Pr^{4+}$ to $Pr^{3+}$ accompanied by the formation of doubly-charged oxygen vacancies and the liberation of oxygen gas. Since all the data for the 1% sample exceeded this upper limit due to measurement errors, the model could not be fit to the data. While the 5% sample could physically be fit, the results of fitting were less than satisfactory. There was no 5% PCO sample analyzed by electrical conductivity measurements to extract suitable vales of $K_R$ or initial values of $K_{Pr}$ and y from. In the absence of better alternatives, the parameters required were taken from the electrical conductivity fitting results of one of the 10% samples, but the results were unacceptable.

The fits for 20% PCO, on the other hand, were quite good, as seen in Figure 6.17. There are deviations at the lowest temperatures, as expected. Points very close to atmospheric

pressure typically yielded the highest error for a given temperature. These initial values are the first collected in a titration experiment, and the rapid changes in measured nonstoichiometry per unit change in $pO_2$ make the data quite sensitive. Data collected below $10^{-2}$ atm $pO_2$ were more reliable. The variation of the fitted initial nonstoichiometry (y) values followed Arrhenius behavior quite well.

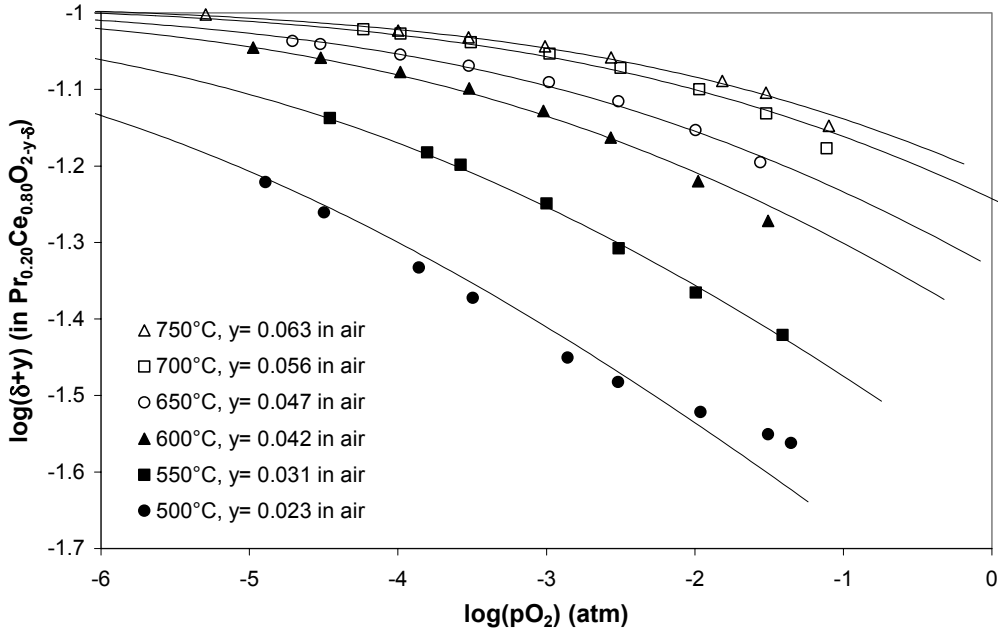


**Figure 6.17. Fitted results of total nonstoichiometry in 20% PCO. Initial nonstoichiometries at each temperature are given in the legend.**

The $K_{Pr}$ values, as determined via coulometric titration, are shown in Figure 6.18 along with those determined via electrical conductivity measurements in 20% PCO. The general agreement between the two sets of experiments is reassuring. The $K_{Pr}$ values determined via coulometric titration are slightly lower than those calculated based on electrical conductivity data. According to the equation given in Table 4.1 describing vacancy concentration under high $pO_2$ conditions, the vacancy concentration is proportional to $K_{Pr}^{-2/3}$. Higher $K_{Pr}$ values indicate a lower vacancy concentration. Therefore, the lower $K_{Pr}$ values determined via coulometric titration may indicate a higher degree of reduction during coulometric titration experiments. This would be possible if uncharged oxygen species form. Electrical conductivity would not detect the

presence of neutral oxygen vacancies, whereas coulometric titration would. It should be noted that the magnitude of the reaction constants determined for 20% PCO are questionable since the samples were cracked and the magnitude of the conductivity was certainly higher than that measured. However, the same set of $K_R$ values were used to fit both sets of data, so the error introduced is consistent across both experiments. The $K_{Pr}$ values were essentially independent of one another in the two sets of data fitting, so comparison of the two values is not unwarranted.

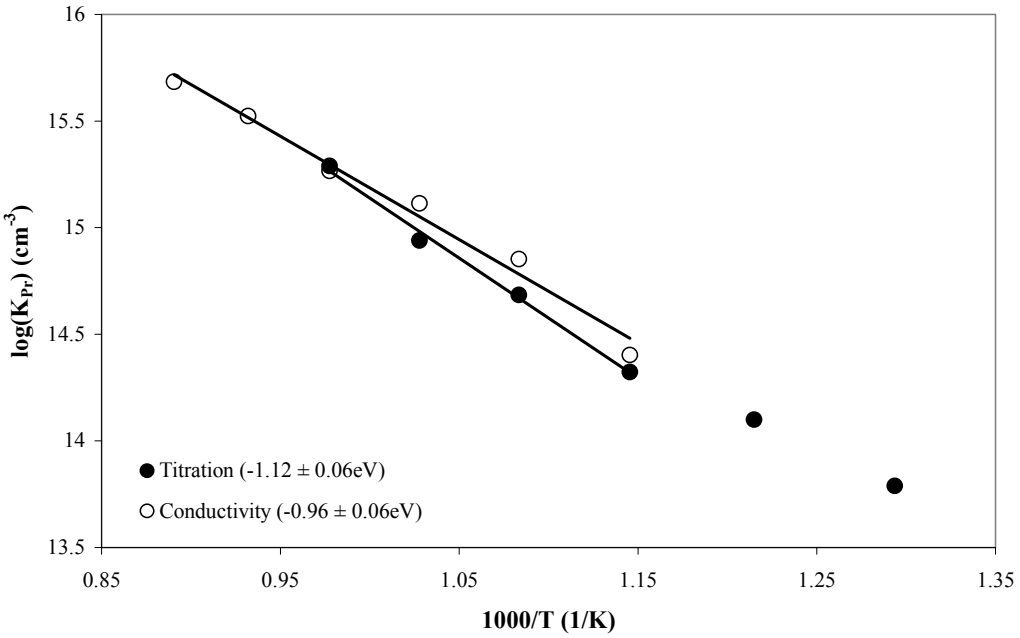


**Figure 6.18. Arrhenius plot of the praseodymium ionization constant determined both by electrical conductivity measurements and by coulometric titration.**

# Chapter 7. Conclusions

## *7.1. Summary*

Electrical conductivity data for $Pr_xCe_{1-x}O_{2-\delta}$, where $0 \leq x \leq 0.20$, were collected from 600-1000°C and $pO_2$ values from 1 atm to $10^{-18}$ atm. A defect model capable of describing the observed $pO_2$ and temperature dependence was devised. A $pO_2$-dependent ionic conductivity was observed at high $pO_2$ in lightly doped PCO resulting from oxidation of $Pr^{3+}$ to $Pr^{4+}$. At high Pr concentrations, an impurity band formed within the $CeO_2$ band gap, resulting in significant electron hopping conductivity at high $pO_2$ values. The effect was most pronounced at low temperatures. Defect association at low temperatures significantly altered the $pO_2$ dependence of the impurity band conductivity.

Coulometric titration measurements were performed in order to confirm the total nonstoichiometry in PCO. The ionization energy for $Pr^{3+} \rightarrow Pr^{4+}$ ($E_{Pr}$) in 20% PCO as calculated from coulometric titration measurements was approximately 1.1 eV, in relatively good agreement with the value determined from electrical conductivity data (approximately 0.95eV). Values of the praseodymium ionization constant ($K_{Pr}$)derived from coulometric titration data were lower than those derived from electrical conductivity measurements. This corresponds to a higher total nonstoichiometry measured via coulometric titration indicating the possible existence of uncharged oxygen vacancies, particularly at low temperatures.

The thermodynamic parameters governing defect formation and transport in PCO were determined. The reduction enthalpy of cerium was significantly decreased from approximately 4.7 eV (the value in pure $CeO_2$) to 3.4 eV in 20% PCO. The energy between the Pr impurity band and the $CeO_2$ conduction band was approximately 0.95 eV for 10% and 20% PCO samples. The measured trap depth was significantly higher (approximately 1.6 eV) in 0.5% and 1% PCO. The impurity band mobility was approximately $10^{-5}$-$10^{-4}$ $cm^2/Vs$, one to two orders of magnitude lower than the mobility of electrons liberated by the reduction of Ce (approximately $10^{-3}$ $cm^2/Vs$). The migration enthalpy for impurity band hopping was approximately 0.55 eV, higher than the hopping enthalpy for intrinsic carriers in $CeO_2$ (0.4 eV). The oxygen ion conductivity in PCO was

comparable to that of other doped ceria electrolyte systems. The oxygen ion migration enthalpy measured for most samples was approximately 0.6-0.9 eV, in agreement with values determined for other rare-earth doped systems. The activation energy observed in pure $CeO_2$ was significantly higher (approximately 1.5eV), also in agreement with previous work.

During the course of these experiments, it became obvious that the mechanical stability of PCO containing high percentages of Pr is a significant problem. It is believed that reduction/oxidation cycling results in lattice dilation/contraction and cracking due to stress. If PCO is to be used in real applications, measures to prevent such cracking must be sought. Highly porous structures may be able to alleviate stresses in the material. Applications in which the material could be used in powder form (such as sorption compressors) would not suffer the effects of cracks. Regardless, the issue must be addressed if successful use of PCO based materials is to be achieved.

## *7.2. Recommendations for Future Work*

Below are several suggestions for future work, both as extensions of the work carried out here in the PCO system and as general recommendations for future studies in defect chemistry:

- The range of compositions examined should be extended to include higher Pr contents. Pure $CeO_2$ is an n-type semiconductor. Pure $Pr_6O_{11}$ is a p-type semiconductor. At a sufficiently high level of solid solution, a transition from n to p-type conductivity should be observed.

- Other experiments should be undertaken to independently verify the parameters derived from the defect model. For instance, magnetic measurements[103] can be used to measure the reduction state of Pr in the material. Thermoelectric power or Hall measurements could be used to experimentally determine carrier concentrations and mobilities. Independent measurements of the fitting parameters used in the defect model would strengthen confidence in the results.

- More suitable samples for AC impedance measurements should be fabricated and the grain boundary vs. bulk contributions to the total conductivity in heavily doped PCO should be determined.

- Diffraction experiments examining ordering in PCO at low temperatures (less than 600°C) is warranted. Some evidence of ordering was observed in these studies, and the phase diagrams of both $CeO_2$ and $PrO_2$ suggest that ordering should be expected at temperatures less than 600°C.

- Attempts to control $pO_2$ using a commercial PID controller should be undertaken. The control algorithm built into such controllers has the potential to better control $pO_2$ over long periods of time.

- A glass with a higher softening temperature should be sought for use in coulometric titration experiments. This would lessen the probability of leaks and allow collection of nonstoichiometry data at higher temperatures.

- Coulometric titration cells should be placed in a $pO_2$ controlled furnace. Many of the problems that arose during titration experiments had to do with the excessive Nernst voltages that develop as a result of the oxygen pressure difference between the inside and outside of the titration cell. If the ambient $pO_2$ around the cell could be lowered (using Ar or a $CO/CO_2$ gas mixture), these voltages would be decreased. It may even be possible to titrate without applying a current. If the $pO_2$ outside the cell is set very low relative to the inside of the cell, then shorting the cell through an ammeter and integrating the current that flows may be sufficient.

- PCO should be examined as an alternate fuel cell cathode material. The mixed conductivity demonstrated in the system at high $pO_2$, combined with high catalytic activity toward redox reactions makes it an attractive candidate. Additionally, the difficulties experienced with chemical reactions at the electrolyte/electrode interface using the typical $LaSr(Co/Fe/Mn)O_3$ electrodes currently employed in solid oxide fuel cell technology could be eliminated by

using a PCO cathode in concert with a compatible ceria based electrolyte instead. Based on the results of this study, a fixed dopant, such as gadolinium, should be added to PCO in order to maintain a high concentration of oxygen vacancies at high $pO_2$. A composition of $Ce_{0.75}Pr_{0.20}Gd_{0.05}O_{2-\delta}$, for instance, might exhibit the high electronic conductivity associated with impurity band formation at high $pO_2$ values, while the Gd concentration would ensure that the vacancy concentration (and conductivity) did not decrease significantly as $Pr^{3+}$ oxidized to $Pr^{4+}$.

- The high catalytic activity of praseodymium makes it an attractive candidate for low temperature gas sensing applications. The flexibility possible in controlling both the magnitude and degree of mixed conductivity with Pr concentration demonstrated during this study makes it an attractive alternative over the standard gas sensing materials used today. Initial studies of PCO as a surface effect gas sensor indicated selectivity toward CO over $H_2$ in compositions of 10% and 20% PCO at temperatures of 300-350°C. These studies should be continued in order to fully explore the potential of PCO in gas sensing applications.

- The high levels of nonstoichiometry achievable at high $pO_2$ makes PCO an attractive candidate material for use as the active material in a mass-sensitive high temperature oxygen sensor. These large deviations result in large changes in mass per unit change in $pO_2$ and increase the expected sensitivity of the resulting sensor.

# References


1. D. J. M. Bevan and E. Summerville, "Mixed Rare Earth Oxides" in *Handbook on the Physics and Chemistry of Rare Earths*, edited by K. A. Gschneider and L. Eyring (North Holland, Amsterdam, 1979), Vol. 3, p. 401.
2. T. H. Etsel and S. N. Flengas, "The Electrical Properties of Solid Electrolytes," *Chem Rev* **70**, 339-376 (1970).
3. H. Inaba and H. Tagawa, "Ceria-Based Solid Electrolytes," *Solid State Ionics* **83** (1-2), 1-16 (1996).
4. H. Arai, T. Kunisaki, Y. Shimizu, and T. Seiyama, "Electrical-Properties of Calcia-Doped Ceria with Oxygen Ion Conduction," *Solid State Ionics* **20** (4), 241-248 (1986).
5. G. Balducci, M. S. Islam, J. Kapar, P. Fornasiero, and M. Graziani, "Bulk Reduction and Oxygen Migration in the Ceria-Based Oxides," *Chem Mater* **12** (3), 677-681 (2000).
6. G. B. Balazs and R. S. Glass, "AC-Impedance Studies of Rare-Earth-Oxide Doped Ceria," *Solid State Ionics* **76** (1-2), 155-162 (1995).
7. A. K. Bhattacharya, A. Hartridge, K. K. Mallick, and J. L. Woodhead, "Low-Temperature Synthesis and Characterization of Ceria-Based Oxide Ion Conductors," *J Mater Sci* **31** (19), 5005-5007 (1996).
8. R. N. Blumenthal, F. S. Brugner, and J. E. Garnier, "Electrical Conductivity of CaO-Doped Nonstoichiometric Cerium Dioxide from 700° to 1500°C," *J Electrochem Soc* **120** (9), 1230-1237 (1973).
9. R. N. Blumenthal and J. E. Garnier, "Electrical-Conductivity and Thermodynamic Behavior of SrO-Doped Nonstoichiometric Cerium Dioxide," *J Solid State Chem* **16** (1-2), 21-34 (1976).
10. G. M. Christie and F. P. F. vanBerkel, "Microstructure - Ionic Conductivity Relationships in Ceria-Gadolinia Electrolytes," *Solid State Ionics* **83** (1-2), 17-27 (1996).
11. K. Eguchi, T. Setoguchi, T. Inoue, and H. Arai, "Electrical-Properties of Ceria-Based Oxides and Their Application to Solid Oxide Fuel-Cells," *Solid State Ionics* **52** (1-3), 165-172 (1992).
12. C. Ftikos, M. Nauer, and B. C. H. Steele, "Electrical-Conductivity and Thermal-Expansion of Ceria Doped with Pr, Nb and Sn," *J Eur Ceram Soc* **12** (4), 267-270 (1993).
13. R. Gerhardt-Anderson and A. S. Nowick, "Ionic-Conductivity of $CeO_2$ with Trivalent Dopants of Different Ionic-Radii," *Solid State Ionics* **5** (10), 547-550 (1981).
14. W. S. Huang, P. Shuk, and M. Greenblatt, "Hydrothermal synthesis and electrical characterization of $(Ce_{0.83}Sm_{0.17})_{1-x}Ln_xO_{2-\delta}$ (Ln = Pr, Tb) as potential electrolyte materials for solid oxide fuel cells," *J Electrochem Soc* **147** (2), 439-443 (2000).
15. V. V. Kharton, F. M. Figueiredo, L. Navarro, E. N. Naumovich, A. V. Kovalevsky, A. A. Yaremchenko, A. P. Viskup, A. Carneiro, F. M. B. Marques,

and J. R. Frade, "Ceria-Based Materials for Solid Oxide Fuel Cells," *J Mater Sci* **36** (5), 1105-1117 (2001).
16. V. V. Kharton, A. P. Viskup, F. M. Figueiredo, E. N. Naumovich, A. L. Shaulo, and F. M. B. Marques, "Electrochemical properties of Pr-doped Ce(Gd)$O_{2-\delta}$," *Mater Lett* **53** (3), 160-164 (2002).
17. C. Kleinlogel and L. J. Gauckler, "Sintering and properties of nanosized ceria solid solutions," *Solid State Ionics* **135** (1-4), 567-573 (2000).
18. C. M. Kleinlogel and L. J. Gauckler, "Mixed Electronic-Ionic Conductivity of Cobalt Doped Cerium Gadolinium Oxide," *J Electroceram* **5** (3), 231-243 (2000).
19. T. Kudo and H. Obayashi, "Oxygen Ion Conduction of Fluorite-Type $Ce_{1-x}Ln_xO_{2-x/2}$ (Ln= Lanthanoid Element)," *J Electrochem Soc* **122** (1), 142-147 (1975).
20. T. Kudo and H. Obayashi, "Mixed electrical conduction in the fluorite-type $Ce_{1-x}Gd_xO_{2-x/2}$," *J Electrochem Soc* **123** (3), 415-419 (1975).
21. S. Lübke and H.-D. Wiemhöfer, "Electronic Conductivity of Gadolinia Doped Ceria," *Ber Bunsen-Ges Phys Chem* **102** (4), 642-649 (1998).
22. S. Lübke and H.-D. Wiemhöfer, "Electronic Conductivity of Gd-Doped Ceria with Additional Pr-Doping," *Solid State Ionics* **117** (3-4), 229-243 (1999).
23. N. Maffei and A. K. Kuriakose, "Solid Oxide Fuel Cells of Ceria Doped with Gadolinium and Praseodymium," *Solid State Ionics* **107** (1-2), 67-71 (1998).
24. D. L. Maricle, T. E. Swarr, and S. Karavolis, "Enhanced Ceria - a Low-Temperature SOFC Electrolyte," *Solid State Ionics* **52** (1-3), 173-182 (1992).
25. I. K. Naik and T. Y. Tien, "Electrical Conduction in $Nb_2O_5$-Doped Cerium Dioxide," *J Electrochem Soc* **126** (4), 562-566 (1979).
26. I. Riess, D. Braunshtein, and D. S. Tannhauser, "Density and Ionic-Conductivity of Sintered $(CeO_2)_{0.82}(GdO_{1.5})_{0.18}$," *J Am Ceram Soc* **64** (8), 479-485 (1981).
27. P. Shuk and M. Greenblatt, "Hydrothermal Synthesis and Properties of Mixed Conductors Based on $Ce_{1-x}Pr_xO_{2-\delta}$ Solid Solutions," *Solid State Ionics* **116** (3-4), 217-223 (1999).
28. B. C. H. Steele, "Appraisal of $Ce_{1-y}Gd_yO_{2-y/2}$ Electrolytes for IT-SOFC Operation at 500°C," *Solid State Ionics* **129** (1-4), 95-110 (2000).
29. H. L. Tuller and A. S. Nowick, "Doped Ceria as a Solid Oxide Electrolyte," *J Electrochem Soc* **122** (2), 255-259 (1975).
30. J. Van herle, T. Horita, T. Kawada, N. Sakai, H. Yokokawa, and M. Dokiya, "Low Temperature Fabrication of (Y,Gd,Sm)-Doped Ceria Electrolyte," *Solid State Ionics* **86-8**, 1255-1258 (1996).
31. D. Y. Wang, D. S. Park, J. Griffith, and A. S. Nowick, "Oxygen-Ion Conductivity and Defect Interactions in Yttria-Doped Ceria," *Solid State Ionics* **2** (2), 95-105 (1981).
32. H. Yahiro, K. Eguchi, and H. Arai, "Ionic-Conduction and Microstructure of the Ceria-Strontia System," *Solid State Ionics* **21** (1), 37-47 (1986).
33. H. Yahiro, K. Eguchi, and H. Arai, "Electrical-Properties and Reducibilities of Ceria Rare Earth Oxide Systems and Their Application to Solid Oxide Fuel-Cell," *Solid State Ionics* **36** (1-2), 71-75 (1989).

34. H. Yahiro, Y. Eguchi, K. Eguchi, and H. Arai, "Oxygen Ion Conductivity of the Ceria Samarium Oxide System with Fluorite Structure," *J Appl Electrochem* **18** (4), 527-531 (1988).
35. H. Yahiro, T. Ohuchi, K. Eguchi, and H. Arai, "Electrical-Properties and Microstructure in the System Ceria Alkaline-Earth Oxide," *J Mater Sci* **23** (3), 1036-1041 (1988).
36. O. Porat, H. L. Tuller, M. Shelef, and E. M. Logothetis, in *Materials Research Society Symposium Proceedings*, edited by P.K. Davies, A.J. Jacobsen, C.C. Torardi et al. (Materials Research Society, Pittsburg, PA, 1997), Vol. 453, pp. 531-535.
37. Y. L. Yang, C. L. Chen, S. Y. Chen, C. W. Chu, and A. J. Jacobson, "Impedance studies of oxygen exchange on dense thin film electrodes of $La_{0.5}Sr_{0.5}CoO_{3-\delta}$," *J Electrochem Soc* **147** (11), 4001-4007 (2000).
38. F. Lecarpentier, H. L. Tuller, and N. Long, "Performance of $La_{0.9}Sr_{0.1}Ga_{0.5}Ni_{0.5}O_3$ as a cathode for a lanthanum gallate fuel cell," *J Electroceram* **5** (3), 225-229 (2000).
39. B. C. H. Steele, K. M. Hori, and S. Uchino, "Kinetic parameters influencing the performance of IT-SOFC composite electrodes," *Solid State Ionics* **135** (1-4), 445-450 (2000).
40. H. Uchida, N. Mochizuki, and M. Watanabe, "High-performance electrode for medium-temperature operating solid oxide fuel cells - Polarization property of ceria-based anode with highly dispersed ruthenium catalysts in ($H_2$+$CO_2$+$H_2O$) gas," *J Electrochem Soc* **143** (5), 1700-1704 (1996).
41. H. J. M. Bouwmeester and A. J. Burggraaf, "Dense Ceramic Membranes for Oxygen Separation" in *The CRC Handbook of Solid State Electrochemistry* (CRC Press, Inc., 1997), pp. 481-534.
42. X. W. Qi, Y. S. Lin, C. T. Holt, and S. L. Swartz, "Electric conductivity and oxygen permeability of modified cerium oxides," *J Mater Sci* **38** (5), 1073-1079 (2003).
43. M. Nauer, C. Ftikos, and B. C. H. Steele, "An Evaluation of Ce-Pr Oxides and Ce-Pr-Nb Oxides Mixed Conductors for Cathodes of Solid Oxide Fuel-Cells - Structure, Thermal-Expansion and Electrical-Conductivity," *J Eur Ceram Soc* **14** (6), 493-499 (1994).
44. Y. Takasu, T. Sugino, and Y. Matsuda, "Electrical-Conductivity of Praseodymia Doped Ceria," *J Appl Electrochem* **14** (1), 79-81 (1984).
45. P. Knauth and H. L. Tuller, "Nonstoichiometry and Relaxation Kinetics of Nanocrystalline Mixed Praseodymium Cerium Oxide $Pr_{0.7}Ce_{0.3}O_{2-x}$," *J Eur Ceram Soc* **19** (6-7), 831-836 (1999).
46. T. S. Stefanik and H. L. Tuller, "Praseodymium-Cerium Oxide as a Surface-Effect Gas Sensor," *submitted to the Journal of Electroceramics* (2003).
47. R. Lorenzelli and B. Touzelin, "System $Ce_2O_3$-$CeO_2$" in *Phase Diagrams for Ceramists*, edited by A. E. McHale (The American Ceramic Society, Westerville, OH, 1991), Vol. Annual 91, p. 197.
48. R. Lorenzelli and B. Touzelin, "Sur le Système $UO_2$-$CeO_2$: Ètude Cristallographique à Haute Tempèrature," *J Nucl Mater* **95** (3), 290-302 (1980).

49. L. Eyring, "Phase Relationships, Reaction Mechanisms and Defect Structures in Rare Earth-Oxygen Systems" in *Science and Technology of Rare Earth Materials-Proceedings of the Indo-U.S. Conference on Science and Technology*, edited by E. C. Subbarao and W. E. Wallace (Academic Press, New York, NY, 1980), pp. 99-118.
50. J. Campserveux and P. Gerdanian, "Etude Thermodynamique de l'Oxyde $CeO_{2-x}$ pour 1.5 < O/Ce < 2," *J Solid State Chem* **23** (1-2), 73-92 (1978).
51. D. J. M. Bevan and J Kordis, "Mixed Oxides of the Type $MO_2$ (Fluorite)-$M_2O_3$ - I: Oxygen Dissociation Pressures and Phase Relationships in the System $CeO_2$-$Ce_2O_3$ at High Temperatures," *J Inorg Nuc Chem* **26** (9), 1509-1523 (1964).
52. D. J. M. Bevan, "Ordered Intermediate Phases in the System $CeO_2$-$Ce_2O_3$," *J Inorg Nuc Chem* **1** (1-2), 49-59 (1955).
53. L. Eyring, "System $PrO_{1.5}$•$PrO_2$" in *Phase Diagrams for Ceramists*, edited by R. S. Roth, J. R. Dennis, and H. F. McMurdle (The American Ceramic Society, Westerville, OH, 1987), Vol. VI, p. 8.
54. M. Mogensen, T. Lindegaard, U. R. Hansen, and G. Mogensen, "Physical-Properties of Mixed Conductor Solid Oxide Fuel-Cell Anodes of Doped $CeO_2$," *J Electrochem Soc* **141** (8), 2122-2128 (1994).
55. H. L. Tuller and A. S. Nowick, "Defect Structure and Electrical-Properties of Nonstoichiometric $CeO_2$ Single-Crystals," *J Electrochem Soc* **126** (2), 209-217 (1979).
56. R. N. Blumenthal, P. W. Lee, and R. J. Panlener, "Studies of the Defect Structure of Nonstoichiometric Cerium Dioxide," *J Electrochem Soc* **118** (1), 123-129 (1971).
57. B. C. H. Steele, "Oxygen Ion Conductors" in *High Conductivity Solid Ionic Conductors*, edited by T Takahashi (World Scientific, Singapore, 1989), pp. 402-446.
58. A. D. Logan and M. Shelef, "Oxygen Availability in Mixed Cerium/Praseodymium Oxides and the Effect of Noble-Metals," *J Mater Res* **9** (2), 468-475 (1994).
59. J. A. Jones and G. D. Blue, "Oxygen-Chemisorption Compressor Study for Cryogenic Joule-Thomson Refrigeration," *J Spacecr Rockets* **25** (3), 202-208 (1988).
60. D. L. Maricle, T. E. Swarr, and H. L. Tuller, "Ceria Electrolyte Composition", US Patent No. 5001021 (1991).
61. Y. Altas, M. Eral, and H. Tel, "Preparation of Homogeneous $(Th_{0.8}U_{0.2})O_2$ Pellets via Coprecipitation of $(Th,U)(C_2O_4)_2$•$nH_2O$ powders," *J Nucl Mater* **249** (1), 46-51 (1997).
62. Alfa-Aesar, a Johnson Matthey Company, 26 Parkridge Road, Ward Hill, MA 01835.
63. S. P. Sangal, B. V. Agarwala, and A. K. Dey, "Complexometric Determination of Rare Earths in Aqueous Solution," *Mikrochim Acta* (3), 660-663 (1969).
64. Carver, Inc, 1569 Morris Street, PO Box 544, Wabash, IN 46922.
65. Consolidated Plastics Company, Inc, 8181 Darrow Road, Twinsburg, OH, 44087.
66. Lindberg/Blue M, 275 Aiken Road, Asheville, NC 28804.
67. Buehler, Ltd, 41 Waukegan Road, Lake Bluff, IL 60044.

68. Engelhard Corporation, 101 Wood Avenue, Iselin, NJ 08830.
69. Swagelok Company, 29500 Solon Road, Solon, OH 44139.
70. Hitachi High Technology America, Electron Microscope Division Headquarters, 5100 Franklin Drive, Pleasanton, CA 94588.
71. Olympus America, Inc, Two Corporate Center Drive, Melville, NY 11747.
72. Rigaku MSC, 9009 New Trails Drive, The Woodlands, TX 77381.
73. Materials Data Incorporated, 1224 Concannon Boulevard, Livermore, CA 94550.
74. International Centre for Diffraction Data, 12 Campus Boulevard, Newtown Square, PA 19073.
75. JEOL USA, Inc, 11 Dearborn Road, Peabody, MA 01960.
76. C. A. Palanduz and D. M. Smyth, "The Effect of Cation Place Exchange on the Electrical Conductivity of $SrBi_2M_2O_9$ (M = Ta, Nb)," *J Eur Ceram Soc* **19** (6-7), 731-735 (1999).
77. National Instruments Corporation, 11500 North Mopac Expressway, Autin, TX 78759.
78. Krohn-Hite Corporation, 15 Jonathan Drive, Unit 4, Brockton, MA 02301.
79. Agilent Headquarters, 395 PageMill Road, PO Box 10395, Palo Alto, CA 94303.
80. Omega Engineering, Inc, One Omega Drive, PO Box 4047, Stamford, CT 06907.
81. Solartron, Inc, 19408 Park Row, Suite 320, Houston, TX 77084.
82. E. O. Ahlgren and F. W. Poulsen, "Thermoelectric Power of Doped Cerium Oxide," *J Phys Chem Solids* **57** (5), 589-599 (1996).
83. A. Honders and J. H. W. Dewit, "The Thermoelectric-Power in $Bi_2O_3$," *J Appl Electrochem* **10** (3), 409-414 (1980).
84. A. Tschöpe, S. Kilassonia, B. Zapp, and R. Birringer, "Grain-size-dependent thermopower of polycrystalline cerium oxide," *Solid State Ionics* **149** (3-4), 261-273 (2002).
85. S. Yamaguchi, K. Kobayashi, K. Abe, S. Yamazaki, and Y. Iguchi, "Electrical conductivity and thermoelectric power measurements of $Y_2Ti_2O_7$," *Solid State Ionics* **115**, 393-402 (1998).
86. H. I. Yoo, C. R. Song, and D. K. Lee, "$BaTiO_{3-\delta}$: Defect structure, electrical conductivity, chemical diffusivity, thermoelectric power, and oxygen nonstoichiometry," *J Electroceram* **8** (1), 5-36 (2002).
87. G. M. Choi, H. L. Tuller, and D. Goldschmidt, "Electronic-Transport Behavior in Single-Crystalline $Ba_{0.03}Sr_{0.97}TiO_3$," *Phys Rev B: Condens Matter* **34** (10), 6972-6979 (1986).
88. A. Trestman-Matts, S. E. Dorris, and T. O. Mason, "Measurement and Interpretation of Thermopower in Oxides," *J Am Ceram Soc* **66** (8), 589-592 (1983).
89. H. L. Tuller and A. S. Nowick, "Small Polaron Electron-Transport in Reduced $CeO_2$ Single-Crystals," *J Phys Chem Solids* **38** (8), 859-867 (1976).
90. D. Schneider, M. Godickemeier, and L. J. Gauckler, "Nonstoichiometry and Defect Chemistry of Ceria Solid Solutions," *J Electroceram* **1** (2), 165-172 (1997).
91. Vesuvius McDanel, A Cookson Company, Beaver Falls, PA 15010.
92. Elan Technology, PO Box 779, 169 Elan Court, Midway, GA 31320.
93. MapleSoft, 615 Kumpf Drive, Waterloo, Ontario, Canada, N2V 1K8.

94. O. Porat and H. L. Tuller, "Simplified Analytical Treatment of Defect Equilibria: Applications to Oxides with Multivalent Dopants," *J Electroceram* **1** (1), 41-49 (1997).
95. G. Mogensen and M. Mogensen, "Reduction Reactions in Doped Ceria Ceramics Studied by Dilatometry," *Thermochim Acta* **214** (1), 47-50 (1993).
96. H. Yahiro, Y. Eguchi, K. Eguchi, and H. Arai, Cited in: "Oxygen Ion Conductivity of the Ceria Samarium Oxide System with Fluorite Structure," *J Appl Electrochem* **18** (4), 527-531 (1988).
97. S. Wang, H. Inaba, H. Tagawa, and T. Hashimoto, "Nonstoichiometry of $Ce_{0.8}Gd_{0.2}O_{1.9-x}$," *J Electrochem Soc* **144** (11), 4076-4080 (1997).
98. S. R. Wang, H. Inaba, H. Tagawa, M. Dokiya, and T. Hashimoto, "Nonstoichiometry of $Ce_{0.9}Gd_{0.1}O_{1.95-x}$," *Solid State Ionics* **107** (1-2), 73-79 (1998).
99. H.L. Tuller, "Mixed Conduction in Nonstoichiometric Oxides" in *Nonstoichiometric Oxides*, edited by O. T. Sørensen (Academic Press, New York, NY, 1981), pp. 271-335.
100. M. A. Panhans and R. N. Blumenthal, "A Thermodynamic and Electrical Conductivity Study of Nonstoichiometric Cerium Dioxide," *Solid State Ionics* **60** (4), 279-298 (1993).
101. M. Sayer and A. Mansingh, "Transport Properties of Semiconducting Phosphate Glasses," *Phys Rev B: Condens Matter* **6** (12), 4629-4643 (1972).
102. W. H. Strehlow and E. L. Cook, "Compilation of Energy Band Gaps in Elemental and Binary Compound Semiconductors and Insulators," *J Phys Chem Ref Data* **2** (1), 163-200 (1973).
103. N. Ohashi, S. Mitarai, O. Fukunaga, and J. Tanaka, "Magnetization and electric properties of Pr-doped ZnO," *J Electroceram* **4** (Supp 1), 61-68 (1999).